A MICROSCOPIC HYPER-SPHERICAL MODEL OF TWO-NEUTRON HALO NUCLEI

By

Ivan Brida

A DISSERTATION

Submitted to
Michigan State University
in partial fulfillment of the requirements
for the degree of

DOCTOR OF PHILOSOPHY

Physics and Astronomy

2009

ProQuest LLC
789 East Eisenhower Parkway
P.O. Box 1346
Ann Arbor, MI 48106-1346

ABSTRACT

A MICROSCOPIC HYPER-SPHERICAL MODEL OF TWO-NEUTRON HALO NUCLEI

By

Ivan Brida

We have developed a microscopic cluster model of light two neutron halo nuclei that incorporates the few-body asymptotics in full extent. The wavefunction of the system consists of a core and two valence neutrons. The core is given in terms of correlated Gaussians. The three-body dynamics between the core and valence neutrons is taken into account by means of the hyper-spherical functions containing an exponentially decaying hyper-radial part. To avoid the spurious motion of the center of mass, Jacobi coordinates are used for the entire system.

In the present work, the model is applied to the lightest two-neutron halo nucleus, ^{6}He. The central Minnesota nucleon-nucleon interaction with and without a spin-orbit addition is used to bind the nucleus. The results are compared to those obtained in other models and to experimental data. Basic structural observables, such as binding relative to ^{4}He, radii and one-body densities are in agreement with other models. The microscopic description of the core allows us to test the efficiency of Pauli projection techniques employed in the few-body models. We demonstrate that proper antisymmetrization is crucial to bind ^{6}He against three-body break-up. Overlap functions between ^{6}He and ^{4}He have been extracted with the aim of reaction calculations involving ^{6}He. In particular, two-neutron transfer reaction p(^{6}He, ^{4}He)t at 25MeV/A is studied.

ACKNOWLEDGMENTS

I would first like to acknowledge my advisor Filomena Nunes. I admire her patience with me—a stubborn student of hers, the freedom she gave me to develop and work on my own ideas even when she did not find them useful, and her guidance and jokes throughout the years. Being her first graduate student, I hope her next students will be less stubborn and will give her less headaches. I would also like to thank my guidance committee members Edward Brown, Sekhar Chivukula, Remco Zegers, Vladimir Zelevinsky, and Gregers Hansen for their comments and suggestions.

I would like to thank Robert Wiringa and Steve Pieper for discussions on the variational Monte Carlo method. I thank Kalman Varga for discussions on the stochastic variational model and for providing me his computer codes.

Next, I would like to thank the Department of Physics and Astronomy at Michigan State university, the NSCL and especially the theory group for providing a great environment to work in. Special thanks goes to Shari Conroy without whom the theory group would fall apart in chaos. The financial support of the National Science Foundation and the Department of Energy is also acknowledged.

I am greatly indebted to the other members of my cohort: Matt Amthor, Jon Cook, Wess Hitt, Andy Rogers, and Terrance Strother. I will never forget all their inappropriate jokes on my behalf and the long nights we spent working on homeworks. Special thanks is addressed to my current and former office mates Jeremy Armstrong, Biruk Gebremariam, and Angelo Signoracci. There are a lot of thank yous for other graduate students and postdocs, including Ania Kwiatkowski, Giuseppe Lorusso, Rhiannon Meharchand, Michal Mocko, and Arnau Rios.

Last, but certainly not least, I express my gratitude to my family, my parents and my brothers for everything they have done for me and for helping me to make it to this point in my life.

Contents

List of Tables

List of Figures

Images in this dissertation are presented in color.

Chapter 1

Introduction

Atomic nuclei represent self-bound ensembles of strongly interacting fermions. Experimental and theoretical explorations of the chart of nuclei have revealed many intriguing features of nuclear matter. Among them, a structural hallmark—the nuclear halo—has been found in the realm of light nuclei near the limits of particle stability.

In general, the halo phenomenon is a threshold effect occurring in loosely bound systems, in which particles are held in short-range potential wells. In favorable circumstances, a barely trapped particle or particles (or a cluster of particles) may tunnel out into the classically forbidden region. This "leakage" populates very dilute and fragile structures near particle emission thresholds. The more loosely the halo particles are confined, the more clearly "the halo stratosphere" is developed.

Besides nuclear physics, halo systems are known or expected to exist in other branches of physics as well. One of the most extended halo systems known to exist is the atomic helium dimer $^4He_2$ which is about ten times larger than a typical diatomic molecule and is bound by only about 10^{-7} eV [1]. Halo states have been predicted or experimentally observed for a range of other systems, such as ^3He-^3He-^{39}K [2], positron-atom complexes [3], hyper-nuclei such as $^3_\Lambda H$ [4] among others. A comprehensive review of halo systems can be found for example in [5].

1.1 Halo in nuclei

The quantum-mechanical tunneling present in halo nuclei produces unexpected effects. The energy needed to remove halo nucleons is drastically less than particle separation energies for typical nuclei. Nuclear radii are enhanced; matter and charge radii may differ considerably. There is evidence that few-body effects may become crucial, leading to the formation of cluster structures beyond the reach of mean field theories.

In a first approximation, the spatial separation of particles in the halo from the rest of the system justifies a simplified description with only a few active constituents. Halo nuclei can be thought of in terms of a few (typically one or two) single halo nucleons orbiting a tightly bound core, thus implying a major role of single-particle properties.[1] In quantitative terms, it has been assessed [6, 7] that for a quantum halo to develop,

1. the probability to find halo particles in the forbidden region beyond the classical turning point should be more than 50%,
2. and the core-halo configuration should occur with more than a 50% probability in a given system.

It has been argued [8, 9] that for a nucleus to meet these criteria:

a. the energy needed to separate the halo part from the rest of the nucleus should be small, more precisely less than about 2 MeV $A^{-2/3}$, with A being the mass number of the nucleus,

b. the halo nucleons should occupy s- or p-angular momentum orbits around the core,

c. and the proton number of the nucleus should not exceed ten or so for a proton halo to develop.

For three-body halo states containing two loosely bound nucleons, the condition b. should be supplemented by a requirement of hyper-momentum[2] $K = 0$ or 1. The formation of

---

[1] Here, we do not consider less straightforward cluster divisions with tightly bound subgroups of nucleons, such as ^{9}Be consisting of two α clusters glued together by a neutron.

[2] To be introduced in Chapter 2.

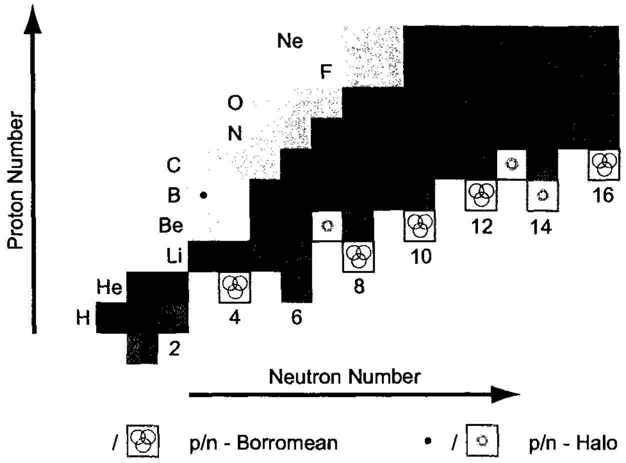

Figure 1.1: Lower part of the chart of nuclei. Stable nuclei are represented by black squares. In this figure, "p" stands for a proton, "n" for a neutron. The term "Borromean" is explained in Section 1.2.

a charged halo is hindered by the Coulomb barrier. These conditions naturally favor light nuclei in Figure 1.1 to populate halo states.

From the modern perspective, the best established nuclear halos live among light neutron-rich nuclei. Examples of one-neutron halo nuclei include the ground states of ^{11}Be (= ^{10}Be + n) [10] and ^{19}C (= ^{18}C + n) [11], excited states in ^{12}B (= ^{11}B + n) and ^{13}C (= ^{12}C + n) [12] and several possible candidates, such as ^{31}Ne (= ^{30}Ne + n) and ^{40}Al (= ^{39}Al + n) [5]. In one-neutron halos, the tail of the relative core-n wavefunction falls off exponentially with the distance between the core and the extra neutron. The decay length, determined by the neutron separation energy, is typically 4–5 times that of ordinary, tightly bound nuclei [5].

In nuclear physics, the most obvious three-body halo candidates are light drip-line nuclei with two neutrons encircling a core. Among them, ^{6}He (= ^{4}He + n + n) and ^{11}Li (= ^{9}Li + n + n) are stereotypical prototypes of nuclear halo systems [13], and they enjoy all the attention of the present work. ^{11}Li is considered the prima donna of all halo nuclei thanks to its very small two-neutron separation energy 378 keV [14]. Other two-neutron halo nuclei include ^{14}Be (= ^{12}Be + n + n) [15], possibly ^{22}C (= ^{20}C + n + n) [16], and other candidates [5].

For completeness, we should mention other nuclei in which some sort of halo may be developed. In the deuteron, for example, the proton (p) and the neutron are very likely to be found outside the range of the strong interaction. The binding energy of the deuteron (-2.2 MeV) is in absolute value small compared to a typical nucleon separation energy (7–8 MeV), arguably making the deuteron the forerunner of all nuclear halo states [17]. On the neutron-rich side of the chart of nuclei, ^{8}He contains four neutrons believed to form a neutron skin around the ^{4}He core [18]. On the proton-rich side, the population of halo nuclei is decimated by the Coulomb barrier. Hints of a proton halo have been seen in ^{8}B (= ^{7}Be + p) [19], ^{17}Ne (= ^{15}O + p + p) [20], and some other nuclear states. Reference [5] contains a more complete list of possible halo states in light nuclei. As an example of theoretical studies on the existence of halo effects in heavier nuclei, medium-mass even-even nuclei have been scrutinized in [21, 22]. The authors of these works concluded that on the large scale the halo phenomenon is very rare and can only exist at the very limit of neutron stability.

In the present work, however, we shall focus only on light two-neutron halo nuclei, in particular on ^{6}He and ^{11}Li.

1.2 Two-neutron halo nuclei: ^{6}He and ^{11}Li

Apart from possessing all of the peculiar halo features, the known two-neutron halo nuclei including ^{6}He and ^{11}Li are Borromean, meaning that the system core + n + n is bound, even though the binary subsystems core + n and n + n are unbound. The term Borromean is adopted after a heraldic symbol of three rings which are joined in such a way that if any one is broken, all three become free [13]. In the helium chain, for example, ^{4}He binds two extra neutrons, but not one, and the di-neutron is unbound as well. This odd-even staggering is merely a consequence of nucleon-nucleon correlations. One then deals meticulously with two correlated neutrons revolving around a core in the low density regime. Thus, these nuclei are ideal playgrounds to study neutron correlations in an almost proton-free environment. It is possible that these nuclei give rise to the so-called Efimov states [23, 24].

The Borromean nature of ^{6}He and ^{11}Li implies that, even at large distances, the core and the valence particles are correlated with no bound binary admixtures. Asymptotically, the wavefunction vanishes exponentially with a decay rate depending on the three-body binding energy, i.e. on the amount of energy needed to break the nucleus up into a core and two free neutrons. The inverse of the decay rate gives a typical "three-body distance" within the nucleus, which is about 7.5 fm in ^{11}Li. For better visual appreciation, this value corresponds to a di-neutron at distance about 6 fm from a ^{9}Li core or to the two neutrons being on opposite sides of the core at mutual distance of about 11 fm. These numbers are to be compared with the range of the nucleon-nucleon interaction of about 1–2 fm and also with the 2.32 fm radius of the ^{9}Li core [13]. The situation is less dramatic in ^{6}He due to its larger two-neutron separation energy[3] of about 970 keV [25]. One then anticipates that many properties of ^{6}He and ^{11}Li will depend chiefly on the asymptotic part of the wavefunction.

Due to the proximity of particle emission thresholds, ^{6}He and ^{11}Li support only a single bound state, the ground state. Moreover, these nuclei are short-lived; the half-life of ^{6}He is 806.7 ms [25] and that of ^{11}Li is even shorter at about 8.8 ms [26]. To be studied, these nuclei have to be produced artificially. Most information about the anatomy of nuclear halos has been obtained in reaction processes leading to continuum excitations and ultimately to the destruction of the investigated nuclei. It is useful to put the most rewarding experimental methods into their historical context. In the following short historical overview, we focus mainly on ^{11}Li, but some of the experiments have been carried out for other halo nuclei including ^{6}He.

1.3 Overview of ^{6}He and ^{11}Li: experiments

The history of two-neutron halo nuclei started with the discovery of ^{6}He back in the 1930s [27]. It took three more decades to produce ^{11}Li for the first time [28]. Current

---

[3] In what follows, the two-neutron separation energy is taken as an absolute value of the three-body binding energy, and the two terms will be used interchangeably.

interest in nuclear halos, however, was sparked by the advent of modern radioactive beam facilities. In 1985, the interaction cross section of helium and lithium isotopes colliding with ordinary nuclear targets was measured [29,30]. The surprisingly large values for ^{11}Li were soon interpreted as a consequence of extended neutron densities, a neutron halo, consisting of a di-neutron coupled to a ^{9}Li core [31]. This speculation was later supported by a measurement of the momentum distribution of ^{9}Li after the break-up of ^{11}Li [32]. Consistent with the di-neutron model, large spatial extent of the halo was, through the uncertainty principle, reflected by narrow relative momentum distributions. The di-neutron model also suggested large two-neutron removal cross sections via Coulomb dissociation. Soon after, the cross sections of electromagnetic dissociation of ^{11}Li on high-Z targets at high [33] and low beam energies [34] were found to reach anomalously large values. Later, charge-exchange cross sections of ^{8,9,11}Li were measured to be about the same [35], thus implying that the ^{9}Li core is little disturbed in ^{11}Li. One of the first attempts to indirectly deduce the neutron density profile of ^{11}Li can be found in [36]. The authors concluded that only density distributions with very long tails consistently reproduce the observed interaction cross-sections. Furthermore, the angular distributions of ^{9}Li and ^{11}Li nuclei scattered elastically from protons are similar, but the elastic scattering cross-section is smaller by about a factor of two for ^{11}Li [37]. In data analysis, both real and imaginary parts of the optical potentials had to be changed considerably for ^{11}Li compared to global fit parameters, in order to account for break-up due to the extended tail of the neutron density. β-decay represents an interesting alternative for extracting information about halo structure. Several theoretical works [38, 39] have investigated the β-decay of ^{11}Li into ^{9}Li and a deuteron (d). They concluded that the β-decay matrix elements are to a large extent determined by the halo part in ^{11}Li. Experimental efforts in this direction reported in [40,41] and more recently in [42] provide evidence that the β-decay takes place essentially in the halo of ^{11}Li, and that it proceeds mainly to the ^{9}Li + d continuum, opening up a new means to study the halo phenomenon in ^{11}Li.

The early reaction experiments were extended in later years, see for example reviews in [43–45]. They include transfer, stripping and break-up reaction studies providing differential, rather than integrated cross-sections. Reaction and decay experiments have been accompanied by precise measurements of static properties: measurements of two-neutron separation energy by methods of radio-frequency spectrometry [14] and Penning trap [46] for ^{11}Li, nuclear charge radius determined by laser spectroscopy for ^{6}He [47] and ^{11}Li [48], and electric quadrupole and magnetic moments of ^{11}Li from nuclear magnetic resonance experiments [49].

In spite of all the experimental efforts, the detailed structure of the two-neutron halo has not been deciphered yet. The consensus seems to be that, in ^{6}He, the two maverick neutrons coexist anywhere between two extreme configurations [13]: a di-neutron with valence neutrons closely spatially correlated, and a cigar configuration in which the two valence particles are on opposite sides of the core. In ^{11}Li, the situation is less clear due to a strong competition between s- and p-waves in the halo part of the wavefunction [13,50]. The question of clustering in ^{6}He and ^{11}Li is the subject of ongoing experimental quest [51–53].

Experimental data concerning two-neutron halos collected over the last decades has become so detailed that theoretical models must be more than merely qualitative to rise to the challenge. Even simple properties, such as the size of the nucleus, turn out to be model dependent and are not real experimental observables [54]. The study of halo nuclei as unstable species via reaction experiments involves tightly intertwined aspects of structure and reaction physics. Details of the reaction component are beyond the scope of this work. Nevertheless, reviews of reaction models used to probe the structure of light exotic nuclei can be found in [55,56].

1.4 Overview of ^{6}He and ^{11}Li: structure theory

Traditionally, theoretical considerations of structure and reactions of halo nuclei have been dominated by few-body models. Few-body structure models of two-neutron halo nuclei have built their success around the fact that, when viewed at a distance, the halo particles are decoupled from the core. Under such an approximation, the core's degrees

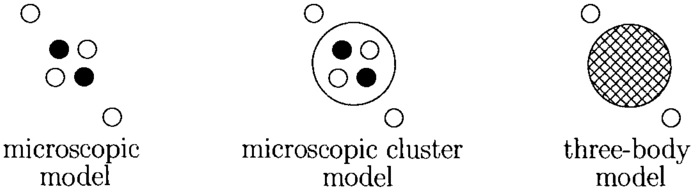

microscopic model

microscopic cluster model

three-body model

Figure 1.2: Schematic representation of structure models of ^{6}He. In microscopic cluster models, a microscopically described ^{4}He core is formed explicitly.

of freedom can be reduced, and the wavefunction factorizes into the core and the valence part. The many-body problem then reduces to a three-body one—core + n + n—held together by effective core-n and n-n interactions. For ^{6}He, the transition from a fully microscopic to a few-body picture is schematically depicted in Figure 1.2.

The early di-neutron models of ^{6}He and ^{11}Li, such as [31], turned out to be too schematic to quantitatively describe experimental data and were soon followed by more sophisticated three-body approaches. In the first generation, the three-body models of these nuclei treated the core as a completely inert object. Several methods of tackling the three-body problem were applied, mostly to ^{6}He and ^{11}Li. They include the Faddeev approach [13,57,58], the hyper-spherical harmonics method [13,59], the variational method on a harmonic oscillator basis [60], the two-body Green's function [61], and the cluster-orbital shell model [62, 63]. Some calculations within a pairing model were reported in [64]. In all their generosity, the three-body models of the next generation rewarded the core with some degrees of freedom, namely with rotational modes [65].

With increasing computational power in recent years and new techniques to solve many-body problems, ab-initio microscopic competitors have emerged in the field of structure models of light exotic nuclei. The microscopic nature of these models allows them to employ realistic nucleon-nucleon and three-nucleon interactions. The Green's function Monte Carlo model has been successfully applied to light nuclei up to ^{12}C [66,67]. The model reproduced the three-body binding energy and radius of ^{6}He. The no-core shell model [68] is another sophisticated approach, which as its name suggests, is a shell model with all particles active in harmonic oscillator shells; i.e. there is no inert core like in standard shell model calculations. The model has been applied to both ^{6}He [69] and ^{11}Li [70]. The fermionic molecular dynamics and the antisymmetrized molecular dynamics represent conceptually similar approaches to the problem of light nuclei [71]. They both use superpositions of Gaussian wave packets for single-particle wavefunctions. Their application to helium isotopes can be found in [72, 73]. As in Green's function Monte Carlo, the structure of ^{11}Li has not yet been successfully described by molecular dynamics models.

Somewhere between few-body and truly microscopic models are microscopic cluster models, in which some degrees of freedom are frozen to reduce the computational demands. This is achieved through the formation of microscopic clusters with a simplified internal structure within the nucleus being modeled. To a certain extent, cluster structures can also be recognized in some of the microscopic models mentioned above. The stochastic variational model [74] and its multi-cluster version [75] has been applied to helium [76] and lithium [77] isotopes. With simpler phenomenological forces of adjusted strength, the model has been able to reproduce basic (three-body-like) properties of ^{6}He and ^{11}Li. Other examples of microscopic cluster models applied to ^{6}He include [78–80]. All these models rely on Gaussians of one sort or another to describe the inter-cluster motion.

Our overview of structure models would not be complete without mean field theories. Widely dispersed halo particles barely feel the short-range nuclear forces exerted by nucleons in the core. As a consequence, valence and core particles experience different mean fields. For Borromean systems in particular, the term mean field is probably not appropriate, as the correlations between halo particles are crucial for the overall binding. Moreover, the last neutron in the core + n + n system can not be bound in the localized mean field of the core + n subsystem since such a bound subsystem does not exist in Borromean nuclei. The importance of unusually small neutron separation energies for mean field calculations was recognized early on [81]. In later shell model calculations, configuration mixing and adjustments to residual interactions have become unavoidable for a good description of exotic nuclei towards the drip-lines [82, 83]. In general, mean field approaches have found it rather challenging to obtain a reasonable description of halo effects in light nuclei.

1.5 Motivation for present work

The obvious advantage of few-body structure models of two-neutron halo nuclei is the exact treatment of halo dynamics. These models provide clear, intuitive insight into the relative motion between the core and valence particles, and as long as implemented properly, they are well suited to capture the long-distance halo characteristics and correlations. On the other hand, microscopic models tackle the many body problem in its full complexity. Thanks to our advancing knowledge of nuclear interactions and increasing computational power, brute force ab-initio models now yield very accurate structure results for many light nuclei. It is reasonable to believe that, sooner or later, ab-initio models will succeed in producing an accurate description of halo nuclei.

We are now in the position to ask why we need yet another structure model to cope with two-neutron halo nuclei. The answer is buried in drawbacks of the above-mentioned structure models and the lack of connection of some of them to reaction theories traditionally formulated in a few-body framework.

The crucial assumption of few-body models, a macroscopic core, turns out to be a double-edged sword: on one hand, it allows us to focus on the most important correlations between core and halo nucleons, on the other hand, it is undoubtedly a (crude) simplification of the many-body problem. To argue in favor of inert cores, some authors indeed suggest that core polarization in halo nuclei is suppressed compared to normal nuclei [84]; but on the other side, there are works that admit the possibility of less inert cores inside halo nuclei [48,76]. Despite the occasional strong claims by few-body practitioners [85], realistic halo nuclei are unfortunately not ideal halo systems; the simple halo picture is always obscured by small idiosyncrasies, and one has always to check that the core is really unperturbed to justify the simplified inert-core few-body approach [86]. Stemming from the simplified picture of the core, probably the two most severe drawbacks of few-body models are the lack of exact antisymmetrization and the usage of effective interactions [87]. Several Pauli blocking techniques have been developed to account for antisymmetrization in few-body models, however, when compared side by side, they may provide different results [88]. Effective interactions, especially those between the core and halo particles, are not necessarily known. Normally, the core-n potentials are adjusted to reproduce some set of experimental core-n findings and the three-body binding energy of the whole nucleus, or attempts are made to derive them from the underlying nuclear forces. Furthermore, there are indications that for reaction calculations three-body wavefunctions perhaps require additional renormalization to account for microscopic effects missing in the inert-core approximation [89]. Nevertheless, few-body models are presently used in most reaction calculations involving halo nuclei.

Some of the above-mentioned drawbacks of few-body models are eliminated in microscopic (cluster) models with halo particles made indistinguishable from those in the core. The microscopic treatment allows one to antisymmetrize wavefunctions properly and use phenomenological or realistic nucleon-nucleon (and three-nucleon) forces. So, what is wrong with microscopic (cluster) models? Well, one could object to several things. The first one is the missing connection to reaction theories, a link so important for the understanding of halo species. To feed reaction calculations formulated in a few-body picture, one would have to extract the necessary information about halo particles from the full microscopic wavefunction, a task that is by no means trivial computationally. Even though recently we have witnessed some progress in this direction for two-body-like (but not halo) projectiles [90, 91], most microscopic structure theories are still far from providing such few-body-like information relevant for three-body-like halo nuclei. This computational obstacle is accompanied by a more fundamental physics question of the adequacy of microscopic models in the asymptotic regions.

From the previous short review of structure theories it has become obvious that to make calculations feasible microscopic (cluster) models exploit computationally tractable bases. Chief among them are the Gaussians and harmonic oscillators. One must remember, however, that at large distances, where the halo nucleons are almost liberated from the core, the wavefunction falls off exponentially. In principle, it should be possible to capture the slower exponential decay by using a large Gaussian or oscillator basis, but as argued in [5], quality precedes quantity in the halo world; that is the actual shape of basis functions matters more than the size of the basis. In other words, the basis functions themselves ought to possess the correct long-distance functional form to produce correct halo asymptotics. For this reason, the authors of [5] concluded that Gaussians are in general not at all suited as a computational basis for halo nuclei. Moreover, most microscopic calculations are variational with the binding energy used to assess the rate of convergence. In general, the convergence of the total binding energy does not guarantee the convergence of other observables and definitely not the convergence of the wavefunction in asymptotic regions.

Based on the arguments presented, one can conclude that both few-body and microscopic structure models have their appealing aspects as well as their drawbacks. We wish to mix the best of the two approaches to create a microscopic structure model of two-neutron halo nuclei that would describe simultaneously short- and especially long-distance regions and allow us to link the structure and reactions of these nuclei. The concept of a microscopic cluster model with a carefully chosen functional form for the wavefunction seems to be ideal to meet our goals. Hereafter, the model of two-neutron halo nuclei developed in the present work shall be referred to as MiCH (microscopic core halos).

In MiCH, a two-neutron halo nucleus will be described by a properly antisymmetrized product of a microscopic core and the valence part consisting of two individual neutrons, or schematically $\Psi = \mathcal{A}^{core-val}(core \times valence)$. We shall use terms "core" and "valence" in spite of the presence of the core-valence antisymmetrizer $\mathcal{A}^{core-val}$ which, in principle, makes nucleons from the two parts of the wavefunction indistinguishable. A more precise meaning of "core" and "valence" will be provided as we go along. At large distances, the wavefunction naturally decouples into the three-body-like form $\Psi \longrightarrow core \times n \times n$, whereas at short distances it is equivalent to a fully antisymmetrized, many-body treatment. To bind the nucleus, effective nucleon-nucleon interactions shall be employed. The theory developed in this work is designed to cope with bound states of two-neutron halo nuclei. The link between structure and reactions will be established for simultaneous two-neutron transfer. In this reaction channel, the two valence neutrons are transferred in one step from a halo projectile to a target nucleus. The transition probability of this process is directly proportional to the overlap integral between the original two-neutron halo projectile and its own core.

1.6 Outline

In the present work, we elaborate on all aspects of MiCH. First, the two major building blocks of the wavefunctions—the valence part and the core—are discussed separately. Chapter 2 focuses on the valence part. A particular three-body model is described, elements of which are later incorporated into MiCH. To find the appropriate functional form for the valence part, the three-body dynamics between the core and the two extra neutrons is studied in interaction-free regions. Chapter 2 also contains results for ^{6}He and ^{11}Li studied within a three-body approach. Chapter 3 presents a microscopic model that meets requirements imposed on the core. MiCH is then finally assembled in Chapter 4 by putting the core and the valence part together. That chapter also includes the computational background needed for evaluation of matrix elements and optimization of variational parameters. Chapter 5 contains results for ^{6}He studied within MiCH. Basic structural features of ^{6}He are elaborated on, and the results obtained within MiCH are compared to those from other models and to experimental data. As part of the discussion, the two-neutron transfer reaction p(^{6}He,^{4}He)t is studied using microscopic structure input for ^{6}He modelled in MiCH. The work finishes with the conclusions and outlook in Chapter 6.

Chapter 2

Valence part

Contrary to standard nuclei, valence particles in two-neutron halo nuclei are weakly bound and the tail of the wavefunction offers large contributions to most physical observables. Any structure model aimed at the description of halo species should take into account the fact that the loosely bound neutrons swim in distant, low-energy regions and are subject to an interaction which is closer to the free rather than in-medium nucleon-nucleon interaction. Thus, a proper treatment of the asymptotic regions is vital if one is to pin down any observable sensitive to the spatial extent of the nucleus. Moreover, the added Borromean peculiarity of two-neutron halos implies pure three-body rather than any other asymptotics. Few-body models are especially well suited to cope successfully with the few-body dynamics and asymptotics of two-neutron halo nuclei. In Chapter 4, the wavefunction in MiCH will be cast as an antisymmetrized product of a microscopic core and a three-body-like valence part describing the relative motion of the two valence neutrons relative to the core.

In the current chapter, we focus on the valence part. To do so, we outline a well established three-body model [65,92,93]. To avoid repetition, the mentioned three-body model will be referred to as "the three-body model". First, we introduce coordinates and three-body basis sets used to attach the halo neutrons to the core in the three-body model, ingredients to be incorporated later into MiCH. Then, we outline details of the three-body model beyond what will be built into MiCH, such as interactions, the Pauli principle, and the actual way of solving the three-body problem. In later chapters, we will have no use of these extra aspects of the three-body problem, but it is useful to lay them out before us to perform three-body calculations for ^{6}He and ^{11}Li, results of which are included in this chapter. The results of three-body calculations for ^{11}Li were recently published by the author and collaborators [50]. For ^{6}He, calculations originally published in [94] are repeated to reach results that were not included in that article but that are needed for comparison with results obtained within MiCH for this nucleus.

2.1 Coordinates and bases

The key ingredient of the three-body model is the Schrödinger equation in the hyper-spherical formalism. The hyper-spherical method, which had been used in other areas of physics, was brought into nuclear physics in [95] with the aim to develop a general nuclear reaction theory. The value added to three-body models in [65,92] was the introduction of deformation and rotational degrees of freedom to an otherwise inert core. The Sturmian hyper-radial basis exploited in [65, 92] was later in [93] replaced by a more suitable Laguerre hyper-radial basis [96].

For clarity, we should define terms "core" and "valence" more precisely. In the current chapter, "valence" will refer to all features of the three-body core + n + n system except the properties of the core, i.e. it will encompass spins of the two neutrons as well as the full information about the relative motion between the three bodies. Later, in Chapter 4, the meaning of these terms will be elaborated.

To see how the three-body model is assembled, let us first analyze a three-body core + n + n bound problem in interaction-free asymptotic regions[1] where, as argued in [5], one ought to employ a basis with appropriate exponentially decaying form. At this point, we are solely interested in relative motion between the three bodies. To eliminate the spurious motion of the total center of mass, only relative Jacobi coordinates between core and neutrons are used as shown in Figure 2.1. In principle, the two sets of Jacobi

---

[1] Long range Coulomb effects are absent due to charge neutrality of valence particles.

coordinates—Y and T—are completely equivalent and the three-body problem can be cast in any of them. The main advantage of Jacobi coordinates over other sets of relative coordinates is that the operator of kinetic energy decouples into two independent single-particle-like pieces with no cross term:

$$T = -\frac{\hbar^2}{2m}\left[\frac{1}{\mu_1}\Delta_{\vec{x}_1} + \frac{1}{\mu_2}\Delta_{\vec{x}_2}\right] = -\frac{\hbar^2}{2m}\left[\Delta_{\vec{x}} + \Delta_{\vec{y}}\right], \tag{2.1}$$

where m is the mass of a nucleon. Then, the interaction-free three-body Schrödinger equation becomes:

$$T\psi\left(\vec{x},\vec{y}\right) = E_{3body}\psi\left(\vec{x},\vec{y}\right), \tag{2.2}$$

with $E_{3body} < 0$ being the three-body binding energy.

It is convenient to seek the solution of Eq. (2.2) in the form with angular and radial parts decoupled, schematically:

$$\psi\left(\vec{x},\vec{y}\right) = \mathcal{H}(x,y)Y_{l_x}(\Omega_x)Y_{l_y}(\Omega_y), \tag{2.3}$$

where Y_l are spherical harmonics (for now, their projection quantum numbers are omitted) and they take care of the angular part of Eq. (2.2). We stress that the orbital momenta l_x and l_y are associated with Jacobi coordinates, rather than any sort of single-particle coordinates. Next, hyper-spherical coordinates from Figure 2.1 are involved. The main advantage of hyper-spherical coordinates is that, as it will soon become obvious, they allow the transformation of the original Eq. (2.2) into a one-dimensional, hyper-radial equation. The radial function $\mathcal{H}(x,y)$ can be equally well written in terms of hyper-spherical coordinates ρ and θ, i.e. $\mathcal{H}(x,y) = \mathcal{H}(\rho,\theta)$. Plugging (2.3) into (2.2) yields:

$$-\frac{\hbar^2}{2m}\left[\frac{1}{\rho^5}\frac{\partial}{\partial\rho}\left(\rho^5\frac{\partial}{\partial\rho}\right) + \frac{1}{\rho^2}\Lambda^2\right]\mathcal{H}\left(\rho,\theta\right) = E_{3body}\,\mathcal{H}\left(\rho,\theta\right), \tag{2.4}$$

Let us consider a three-body system core + n$_1$ + n$_2$. In the laboratory frame, the three objects are at positions $\vec{r}_{core}$, $\vec{r}_{n_1}$ and $\vec{r}_{n_2}$. Then, there are two different—Y- and T-like—sets of Jacobi coordinates $\vec{x} = \{\vec{x}_i, i = 1, 2, 3\}$:

Y	T
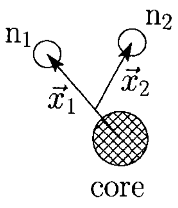	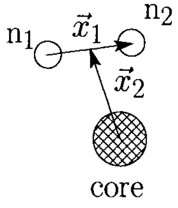

Relative Jacobi coordinates $\vec{x}_1$ and $\vec{x}_2$ connect centers of masses of subgroups of objects; the last Jacobi coordinate $\vec{x}_3$ (not shown in the graphics) is equal to the position of the center of mass of the three-body system in the laboratory frame:

Y	T
$\vec{x}_1 = \vec{r}_{n_1} - \vec{r}_{core}$	$\vec{x}_1 = \vec{r}_{n_2} - \vec{r}_{n_1}$
$\vec{x}_2 = \vec{r}_{n_2} - (\vec{r}_{n_1} + A_{core}\vec{r}_{core})/(A_{core} + 1)$	$\vec{x}_2 = (\vec{r}_{n_2} + \vec{r}_{n_1})/2 - \vec{r}_{core}$
$\vec{x}_3 = \vec{r}_{CMS} = (A_{core}\vec{r}_{core} + \vec{r}_{n_1} + \vec{r}_{n_2})/A$	

The volume element corresponding to the two relative Jacobi coordinates is:

$$\mathrm{d}V = \mathrm{d}\vec{x}_1 \mathrm{d}\vec{x}_2 = x_1^2 x_2^2 \,\mathrm{d}x_1 \mathrm{d}x_2 \mathrm{d}\Omega_1 \mathrm{d}\Omega_2.$$

Here, Ω_i comprises the standard polar and azimuthal spherical angles associated with $\vec{x}_i$. Next, rescaled relative Jacobi vectors are defined as:

$$\vec{x} = \sqrt{\mu_1}\,\vec{x}_1, \qquad \vec{y} = \sqrt{\mu_2}\,\vec{x}_2$$

with dimensionless reduced mass factors:

Y	T
$\mu_1 = A_{core}/(A_{core} + 1)$	$\mu_1 = 1/2$
$\mu_2 = (A_{core} + 1)/A$	$\mu_2 = 2A_{core}/A$

Note that spherical angles associated with $\vec{x}$ and $\vec{y}$ are the same as Ω_1 and Ω_2, i.e. $\Omega_x = \Omega_1$ and $\Omega_y = \Omega_2$. Finally, the hyper-spherical coordinates, the hyper-radius ρ and the hyper-angle θ, are introduced as:

$$x = \rho \sin\theta, \qquad y = \rho\cos\theta.$$

The volume element now becomes:

$$\mathrm{d}V = (\mu_1\mu_2)^{-3/2}\,\rho^5 \sin^2\theta \cos^2\theta \,\mathrm{d}\rho\,\mathrm{d}\theta\,\mathrm{d}\Omega_x\,\mathrm{d}\Omega_y.$$

Figure 2.1: Definition of Jacobi and hyper-spherical coordinates for a three-body system core + n$_1$ + n$_2$. A_{core} and A are the mass numbers of the core and of the whole system.

with the grand-angular operator Λ^2:

$$\Lambda^2 = \frac{1}{\sin^2 2\theta}\frac{\partial}{\partial\theta}\left(\sin^2 2\theta\frac{\partial}{\partial\theta}\right) - \frac{l_x(l_x+1)}{\sin^2\theta} - \frac{l_y(l_y+1)}{\cos^2\theta}. \tag{2.5}$$

This operator contains dimensionless magnitudes $l_x(l_x+1)$ and $l_y(l_y+1)$ of orbital momenta as traces of the orbital motion. The grand-angular operator has a complete spectrum of eigenfunctions enumerated by hyper-momentum K:

$$\Lambda^2\varphi_K^{l_x l_y}(\theta) = -K(K+4)\varphi_K^{l_x l_y}(\theta). \tag{2.6}$$

In [95], the eigenfunctions $\varphi_K^{l_x l_y}(\theta)$ were found in terms of hyper-geometric functions. For the purposes of the three-body model, these functions are transformed by means of the relationship 22.5.42 from [97] into a more convenient form:

$$\varphi_K^{l_x l_y}(\theta) = N_K^{l_x l_y}\sin^{l_x}\theta\cos^{l_y}\theta P_{n_{jac}}^{l_x+\frac{1}{2},l_y+\frac{1}{2}}(\cos 2\theta), \tag{2.7}$$

where $P_{n_{jac}}^{l_x+\frac{1}{2},l_y+\frac{1}{2}}(\cos 2\theta)$ is a Jacobi polynomial of the order n_{jac}. Then, the allowed values of the hyper-momentum K are:

$$K = l_x + l_y + 2n_{jac} \qquad n_{jac} = 0, 1, 2, \ldots \tag{2.8}$$

For a given pair of orbital quantum numbers $\{l_x,\ l_y\}$, hyper-angular functions $\varphi_K^{l_x l_y}$ can be made orthonormal with respect to the weight factor $\sin^2\theta\cos^2\theta$ from the hyper-spherical volume element in Figure 2.1:

$$\int_0^{\pi/2}\varphi_K^{l_x l_y}(\theta)\varphi_{K'}^{l_x l_y}(\theta)\sin^2\theta\cos^2\theta\,\mathrm{d}\theta = \delta_{K,K'}. \tag{2.9}$$

This requires:

$$N_K^{l_x l_y} = \sqrt{2^{l_x+l_y+2n_{jac}+3}\frac{(l_x+l_y+2n_{jac}+2)n_{jac}!(l_x+l_y+n_{jac}+1)!}{[2(n_{jac}+l_x)+1]!![2(n_{jac}+l_y)+1]!!\,\pi}} \tag{2.10}$$

with the aid of relationships 22.1.2 and 22.2.1 from [97].

Since the hyper-angular part of the wavefunction in Eq. (2.3) can be expressed in terms of functions Eq. (2.7), it is convenient to decompose the radial part $\mathcal{H}(\rho,\theta)$ of the wavefunction further into a product of hyper-radial and hyper-angular parts:

$$\mathcal{H}(\rho,\theta) = \mathcal{R}(\rho)\,\varphi_K^{l_x l_y}(\theta) = \rho^{-5/2}\,u(\rho)\,\varphi_K^{l_x l_y}(\theta), \tag{2.11}$$

where the factor $\rho^{-5/2}$ is chosen to cancel the factor ρ^5 in (2.4). By using this new form of the radial part of the wavefunction, Eq. (2.4) is brought to its final one-dimensional hyper-radial form:

$$\left[\frac{\mathrm{d}^2}{\mathrm{d}\rho^2} - \frac{\left(K+\frac{3}{2}\right)\left(K+\frac{5}{2}\right)}{\rho^2} - \kappa^2\right] u(\rho) = 0, \tag{2.12}$$

which is the only equation that needs to be solved. The three-body binding energy is now hidden in a decay parameter to-be κ:

$$\kappa^2 = \frac{2m\left|E_{3body}\right|}{\hbar^2}. \tag{2.13}$$

In Eq. (2.12), the term proportional to ρ^{-2} can be interpreted as an effective centrifugal barrier. This barrier combines not only the effects of single-particle-like centrifugal barriers associated with each Jacobi coordinate, but also an added effective barrier reflecting the difficulty of finding the two neutrons close to the core simultaneously. In contrast to the two-body case, the barrier does not vanish even for the lowest possible hyper-momentum $K = 0$ and thus for the most trivial orbital motion $l_x = l_y = 0$.

The hyper-radial equation Eq. (2.12) provides the remaining clues to build the skeleton of the three-body model. At small hyper-radii, the hyper-radial function $u(\rho)$ vanishes:

$$u(\rho) \xrightarrow{\rho\to 0} \rho^{K+\frac{5}{2}}, \tag{2.14}$$

whereas at large hyper-radii, the hyper-radial part of the wavefunction falls off as:

$$u(\rho) \xrightarrow{\rho\to\infty} \exp(-\kappa\rho), \qquad \mathcal{R}(\rho) \xrightarrow{\rho\to\infty} \rho^{-5/2}\exp(-\kappa\rho). \tag{2.15}$$

Indeed, the three-body binding energy buried in κ through Eq. (2.13) determines the decay rate of the wavefunction. The smaller the binding energy the more pronounced the halo effects. In the three-body approximation, two-neutron halo nuclei posses only the long-distance asymptotics in Eq. (2.15) due to the non-existence of any bound binary subsystem, and because the hyper-radius is invariant under the change of Jacobi sets, the asymptotics are the same in both Y and T Jacobi sets. Having in mind the importance of asymptotical behavior of the wavefunction, the three-body model employs a Laguerre hyper-radial basis introduced in [96]:

$$\mathcal{R}_{n_{lag}}(\rho,\rho_0) = \frac{1}{\rho_0^3}\sqrt{\frac{n_{lag}!}{(n_{lag}+5)!}}\, L^5_{n_{lag}}\left(\frac{\rho}{\rho_0}\right)\exp\left(-\frac{1}{2}\frac{\rho}{\rho_0}\right), \tag{2.16}$$

where $L^5_{n_{lag}}(\rho/\rho_0)$ are associated Laguerre polynomials of the order $n_{lag} = 0,1,2,\ldots$. A few comments regarding this basis are appropriate at this point. First and foremost, this basis is just a suitable mathematical basis, elements of which can not be interpreted as hyper-radial eigenfunctions of the physical three-body system. The basis explicitly contains the desired exponential part. The basis functions $\mathcal{R}_{n_{lag}}$ are orthonormal with respect to the weight ρ^5 which occurs in the hyper-spherical volume element in Figure 2.1:

$$\int_0^\infty \mathcal{R}_{n_{lag}}(\rho,\rho_0)\,\mathcal{R}_{n'_{lag}}(\rho,\rho_0)\,\rho^5\,\mathrm{d}\rho = \delta_{n_{lag},n'_{lag}} \tag{2.17}$$

with the help of the relationship 22.2.12 from [97]. Moreover, the basis is complete for any value of ρ_0. This fact is of great importance because any ρ_0 can be used in calculations and yet the proper asymptotic exponential behavior determined by the a priori unknown three-body binding energy, or κ, can be reconstructed. Last, the hyper-radial basis is privileged in that its index n_{lag} is not restricted by quantum numbers attached to the spherical and hyper-angular parts of the wavefunction.

Based on these schematic arguments, a single basis term for the valence part of the wavefunction is written as:

$$\psi_{n_{lag}\gamma_{val}J^{\pi}_{val}} = \mathcal{R}_{n_{lag}}(\rho,\rho_0)\,\mathscr{Y}_{\gamma_{val}J^{\pi}_{val}}\left(\theta,\Omega_x,\Omega_y,\chi_{n_1},\chi_{n_2}\right) \tag{2.18}$$

where $\mathscr{Y}$ is a generalized hyper-harmonic function in an LS-coupled product form:

$$\begin{aligned}\mathscr{Y}_{\gamma_{val}J^{\pi}_{val}}(\theta,\Omega_x,\Omega_y,\chi_{n_1},\chi_{n_2}) &= \varphi_K^{l_x\,l_y}(\theta)\times \\ &\left[\left[Y_{l_x}(\Omega_x)\otimes Y_{l_y}(\Omega_y)\right]_L\otimes\left[\chi_{n_1}\otimes\chi_{n_2}\right]_S\right]_{J^{\pi}_{val}}\end{aligned} \tag{2.19}$$

J^{π}_{val} denotes the total angular momentum and the parity of the valence part. The parity is determined by orbital momenta l_x and l_y as $\pi = (-1)^{l_x+l_y}$. χ_{n_1} and χ_{n_2} are spins of the two valence neutrons. Index γ_{val} comprises quantum numbers related to all but the hyper-radial part, as well as the Jacobi channel identifier Y or T, i.e. $\gamma_{val} = \{K, l_x, l_y, L, S, \mathrm{Y}/\mathrm{T}\}$. This form of valence terms is sufficient for the three-body model; later, in Chapter 4, each valence term will be enriched by isospins of valence particles.

In this section, we have introduced only those elements of the three-body model that will be in Chapter 4 incorporated into MiCH. The next section details the remaining ingredients of the three-body model.

2.2 Other ingredients of the three-body model

In the three-body model, the core is a macroscopic object with states $\Phi_{J^{\pi}_{core}}(\xi)$ that are eigenstates of the core's intrinsic Hamiltonian:

$$h^{core}(\xi)\Phi_{J^{\pi}_{core}}(\xi) = \epsilon_{J^{\pi}_{core}}\Phi_{J^{\pi}_{core}}(\xi). \tag{2.20}$$

To improve upon the inert-core assumption, the adopted three-body model assumes that the core behaves as a macroscopic deformed rotor and includes the lowest energy states of a rotational band built on the ground state of the core. The eigenstates of the core are the rotational matrices with Euler angles as coordinates ξ. Quadrupole deformation serves as the collective degree of freedom.

A question may arise whether the assumption of a deformed rotor-like core is justified in light nuclei. Even though it is true that light nuclei in general do not show genuine rotor-like features, some of them are known to be deformed. In such cases, the quadrupole deformation can be adjusted to reproduce the strength of the E2 transition between the ground state and the first excited state in the core, as in the case of ^{10}Be core in ^{11}Be [10]. When the core does not exhibit rotor-like features or the E2 transition strength is not known, the quadrupole deformation is a free variational parameter taken from a reasonable physical interval, as in the case of a ^{9}Li core in ^{11}Li [50]. Besides three-body calculations for ^{11}Li in Section 2.3, we will not rely on the assumption of a rotor-like core in this work.

Having the basis in Eq. (2.18) for the valence part and the states of the core given by $\Phi_{J^{\pi}_{core}}$, the three-body decomposition of the total wavefunction is finally written as:

$$\Psi_{J^{\pi} M_J} = \sum_{J^{\pi}_{core}\, n_{lag}\, \gamma_{val}\, J^{\pi}_{val}} c_{J^{\pi}_{core}\, n_{lag}\, \gamma_{val}\, J^{\pi}_{val}} \left[\Phi_{J^{\pi}_{core}} \otimes \psi_{n_{lag}\, \gamma_{val}\, J^{\pi}_{val}} \right]_{J^{\pi} M_J} \tag{2.21}$$

with numbers c being linear expansion coefficients. It is understood that parities π in the last expression implicitly carry the same subscripts as corresponding J. The number of terms in the expansion is controlled through the number of included states of the core, maximum hyper-momentum K, maximum order n_{lag} of hyper-radial basis functions, and the parity requirements $\pi = \pi_{core}\, \pi_{val}$ and $\pi_{val} = (-1)^{l_x + l_y}$. Additional constraints on the basis may be imposed by limiting the maximum orders l_x, l_y of partial waves. To take advantage of the completeness of the hyper-radial basis in Eq. (2.16), the nonlinear parameter ρ_0 is the same in all terms in Eq. (2.21). Although, in principle, both Y and T Jacobi sets of coordinates work equally well and could even be mixed in the wavefunction,

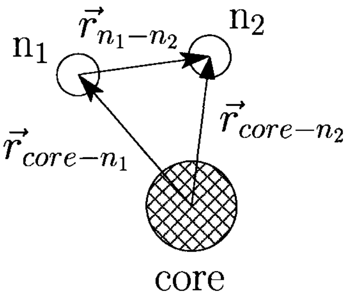

Figure 2.2: Pair-wise coordinates used to define two-body potentials in the three-body model. These coordinates are essentially the same as vectors $\vec{x}_1$ in Figure 2.1, but they are renamed here for the purpose of potential definitions.

the three-body model starts with the wavefunction written solely in the T Jacobi basis for reasons explained later in this section.

In Section 2.1, a simplified three-body problem in the interaction-free region was considered. We now extend our considerations to the full physical space where the three-body Hamiltonian contains the kinetic energy T, the intrinsic Hamiltonian of the core h^{core}, two-body interactions V^{core-n} and V^{n-n} for all pairs of interacting bodies, and a possible three-body interaction V^{3body}:

$$H = T + h^{core}(\xi) + V^{core-n}(\vec{r}_{core-n_1}, \xi) + V^{core-n}(\vec{r}_{core-n_2}, \xi) + V^{n-n}(\vec{r}_{n_1-n_2}) + V^{3body} \tag{2.22}$$

Figure 2.2 depicts the corresponding pair-wise coordinates. The operator of kinetic energy expressed in Jacobi coordinates appears in Eq. (2.1).

In three-body models in general, the exact form of two-body interactions, especially those between the core and the valence particles, is rather uncertain. In some works, inter-cluster potentials were derived from underlying nucleon-nucleon interactions [98]. Such potentials are non-local, however. In most three-body applications to two-neutron halo nuclei, the core-n interactions are not founded microscopically; rather they are given an empirical form with parameters adjusted to reproduce some set of experimental findings for the core + n system and possibly the three-body binding energy. The three-body model in this chapter adopts the later approach. The exact form of potentials will be shown later in this chapter when three-body results for ^{6}He and ^{11}Li will be discussed. For some core-n systems, such as ^{4}He-n, the interaction can be fitted to reproduce scattering phase shifts. For other systems, such as ^{9}Li-n, the scattering phase shifts are not available. One then adjusts potential parameters to reproduce experimentally known low-lying energy levels in the core + n system asserting that the levels can be constructed from a single neutron orbiting the core. Unfortunately, low lying energy spectra of the core + n system may not be well known, as it happens to be in the case of ^{10}Li [99]. For the interaction between the valence neutrons some sort of realistic nucleon-nucleon potential is used. When the two-body interactions alone are not sufficient to bind the three-body system by the experimentally observed amount against the three-body breakup, an additional three-body interaction may be introduced. Overall, it becomes obvious that the uncertainty due to interactions remains one of the major drawbacks of three-body models.

In few-body models, it is impossible to account properly for the fermionic nature of nucleons. The wavefunction can not be fully antisymmetrized due to the macroscopic treatment of the core. The wavefunction can, however, be explicitly made antisymmetric under the permutation of valence neutrons, a requirement easily achieved in the T Jacobi basis by imposing:

$$l_x + S + T = \text{odd} \tag{2.23}$$

where l_x is the orbital momentum of the relative motion between the two neutrons, and S and T are total spin and isospin of the valence part. For two neutrons, $T = 1$. This simple antisymmetry condition considerably reduces the number of available channels in the T Jacobi basis when compared to the Y set of coordinates. It is for this very reason that the three-body model starts with the wavefunction in Eq. (2.21) written in the T Jacobi basis. To account approximately for the Pauli blocking between the core and each valence neutron, the model space is restricted further. The three-body Hamiltonian in Eq. (2.22) does not provide information about the internal structure of the core. The model then assumes that the fictitious core's neutrons sit in the same core-n potential well defined for valence neutrons which, as we have argued in Chapter 1, may not be adequate for halo systems. Nevertheless, the lowest states produced by the core-n interaction are said to be occupied by neutrons in the core and as such should be eliminated from the model space available for valence neutrons. Several different techniques exist to suppress the forbidden core-n states [88]. In the three-body model described in this chapter, such forbidden states are projected out before diagonalization [65].

The linear coefficients c in Eq. (2.21) can be obtained through the energy matrix diagonalization. Upon arbitrary reordering of terms in Eq. (2.21), the three-body wavefunction can be schematically written as:

$$\Psi = \sum_i c_i \Psi_i. \tag{2.24}$$

When no core-n states are projected out of the valence model space, the expansion coefficients c_i are obtained by solving a set of simultaneous linear equations:

$$\boldsymbol{H}_{ij}\, c_j = E\, \boldsymbol{I}_{ij}\, c_j \tag{2.25}$$

with energy and overlap matrix elements defined as:

$$\boldsymbol{H}_{ij} = \langle \Psi_i | H | \Psi_j \rangle, \qquad \boldsymbol{I}_{ij} = \langle \Psi_i | \Psi_j \rangle. \tag{2.26}$$

The operator H is the Hamiltonian from Eq. (2.22). In Eq. (2.25), E is the binding energy of the nucleus. In the three-body model, $E = E_{3body}$. When the forbidden core-n states are projected out before diagonalization, matrix elements $\boldsymbol{H}$ and $\boldsymbol{I}$ take a more complicated form, which can be found in [65].

In actual calculations, it may be useful to move between the Y and T Jacobi sets. For example, the wavefunction in Eq. (2.21) is written in the T basis, but the matrix elements of the core-n interaction are most simply calculated in the Y basis. A change of Jacobi systems only affects the spherical and hyper-angular parts of hyper-harmonics in Eq. (2.18). Under a transformation of Jacobi sets, hyper-harmonic functions undergo a unitary transformation:

$$\mathscr{Y}_{\gamma_{val} J^{\pi}_{val}}\left(\theta, \Omega_x, \Omega_y, \chi_{n_1}, \chi_{n_2}\right) = \sum_{l'_x\, l'_y} \langle l'_x l'_y | l_x l_y \rangle_{KL}\, \mathscr{Y}_{\gamma'_{val} J^{\pi}_{val}}\left(\theta', \Omega'_x, \Omega'_y, \chi_{n_1}, \chi_{n_2}\right), \tag{2.27}$$

where the primed and unprimed quantities refer to different Jacobi sets. In γ_{val} and γ'_{val}, quantum numbers K, L and S are the same. The coefficients $\langle l'_x l'_y | l_x l_y \rangle_{KL}$, called the Raynal-Revai coefficients [100], have analytic forms. Because of the orthonormality of hyper-harmonic functions in all quantum numbers, squares of Raynal-Revai coefficients can be interpreted as probabilities to find a basis state with quantum numbers K, l'_x, l'_y, L, S in one Jacobi set in a state with numbers K, l_x, l_y, L, S in the other Jacobi set. For example, for $K = 0$, there exists only a single combination $l_x = l_y = 0$ allowed by Eq. (2.8). Therefore, in Eq. (2.18), basis states with $K = 0$ in different Jacobi sets are essentially identical. Also, low partial waves l_x, l_y in one Jacobi set may contain all higher partial waves l'_x, l'_y allowed by Eq. (2.8) in the other Jacobi set. The Raynal-Revai coefficients will be useful in Chapter 5 where ^{6}He will be scrutinized.

To conclude the discussion of the three-body model, we establish basic relationships between geometrical measures within a three-body system. We assume, for a while, that the core in Eq. (2.21) is described by a microscopic wavefunction $\Phi_{J^{\pi}_{core}}$. Then, one would be dealing with a system of A nucleons consisting of Z protons and N neutrons. The first A_{core} nucleons including all protons would be contained in the core. For such an A-body system, an operator of the average squared distance of nucleons from the position of the total center of mass $\vec{r}_{CMS} = (1/A)\sum_{i=1}^{A} \vec{r}_i$ could be defined as:

$$r_m^2 \equiv \frac{1}{A} \sum_{i=1}^{A} \left(\vec{r}_i - \vec{r}_{CMS}\right)^2, \tag{2.28}$$

where $\vec{r}_i$ would be the position of the i-th nucleon in the laboratory frame. After taking the square root of the mean value of this operator applied to the wavefunction in Eq. (2.21), one would obtain the commonly computed root-mean-square (rms) matter radius $\langle r_m^2 \rangle^{1/2}$ of the nucleus, which can be expressed as:

$$\langle r_m^2 \rangle^{1/2} = \sqrt{\frac{1}{A}\left[A_{core}\langle r_m^2(core)\rangle + \langle \rho^2 \rangle\right]}, \tag{2.29}$$

where $\langle\rangle$ denotes an expectation value and $\langle r_m^2(core)\rangle$ is a square of the rms matter radius of the core relative to the core's center of mass. Similarly, one could define an operator with the summation over protons only:

$$r_p^2 \equiv \frac{1}{Z}\sum_{i=1}^{Z}(\vec{r}_i - \vec{r}_{CMS})^2. \tag{2.30}$$

The corresponding rms proton radius $\langle r_p^2 \rangle^{1/2}$ of the nucleus could be computed as:

$$\langle r_p^2 \rangle^{1/2} = \sqrt{\langle r_p^2(core)\rangle + \langle r_{core-CMS}^2 \rangle}, \tag{2.31}$$

where $\langle r_p^2(core)\rangle$ is a square of the rms proton radius of the core and $r_{core-CMS}$ is the distance between the core's center of mass and the center of mass of the whole nucleus. Finally, an operator for the neutrons could be defined as:

$$r_n^2 \equiv \frac{1}{N}\sum_{i=1}^{N}(\vec{r}_i - \vec{r}_{CMS})^2 \tag{2.32}$$

with the summation restricted to neutrons only. The expectation values of r_m^2, r_p^2, and r_n^2 would be related simply as:

$$\langle r_m^2 \rangle = \frac{1}{A}\left[Z\langle r_p^2 \rangle + N\langle r_n^2 \rangle\right] \tag{2.33}$$

In reality, however, the core in Eq. (2.21) is a macroscopic object. Therefore, the core's rms matter and proton radii can not be directly computed in the three-body model. Rather, they must be inserted into Eq. (2.29) and Eq. (2.31) by hand. Within the three-body picture, all protons in a two-neutron halo nucleus are confined inside the core. It is merely due to the core's motion relative to the center of mass of the nucleus that the rms proton radius of the nucleus in Eq. (2.31) is larger than that of the core.

2.3 ^{11}Li in the three-body model

As part of the present work, ^{11}Li was studied within the three-body model introduced in this chapter. The ^{9}Li core is allowed to be deformed and/or excited. The material presented in this section is based on the article [50]. In the paper, the value 295 ± 26 keV [101] was used for the two-neutron separation energy in ^{11}Li. However, as also commented in the paper, a new experimental value 376 ± 5 keV [102] was reported for the two-neutron separation energy after the completion of our calculations, Later, this new value was finally corrected to be 378 ± 5 keV [14]. In this section, no attempt has been made to change the discussion and results to account for the change in the two-neutron separation energy.

2.3.1 Introduction

In the early days, three-body models of two neutrons and an inert ^{9}Li core were developed to describe properties of ^{11}Li [13, 58, 61, 103]. At that time nothing was known about the core + n subsystem ^{10}Li, and theorists could play the game of adjusting freely the effective ^{9}Li-n interaction in order to produce a sensible ^{11}Li ground state. In these models, two neutrons were coupled to the ground state of ^{9}Li and the final composition of the valence part of the wavefunction varied significantly depending on the core-n interaction used. In [58] a three-body force was introduced in addition to the two-body core-n and n-n interactions. In [61, 104], a density-dependent n-n delta force was used and emphasis was given to the importance of pairing. Three-body inert-core models have been expanded to generate three-body continuum states [105] and the complexity of these three-body scattering states was analyzed within the context of proton inelastic scattering.

Early microscopic calculations were unable to reproduce a realistic binding energy for ^{11}Li without artificially renormalizing the interactions [81, 106]. As pairing effects had been identified to be crucial [61], by introducing a phenomenological force in the pairing channel, a self-consistent description of the Li isotopic chain became possible within the relativistic Hartree-Bogolyubov framework [107]. Effective interactions valid near the driplines have meanwhile been developed in the shell model [108]. Nevertheless, configuration mixing, required to produce a realistic ground state for ^{11}Li, is still introduced by hand. In the mean time, some ab-initio methods have reached nuclei with mass eleven [67, 70]. Although the general spectra for light nuclei look promising, ab-initio models still have difficulties dealing with halo nuclei, ^{11}Li in particular.

There are still some open questions regarding ^{11}Li, even when considering the ground state only. Should the excitation and quadrupole deformation of ^{9}Li play a role in the structure of ^{11}Li? Using the three-body framework, it was our aim to shed some light on these issues under the constraints provided by the new ^{10}Li data. Besides the $3/2^-$ ground state, the $1/2^-$ first excited state of ^{9}Li should also be present in the model space due to its low excitation energy of 2.69 MeV [99]. We indeed carried out calculations in such an extended model space, but results were not sensitive to the inclusion of the first excited state of the core. This is probably due to the lower spin of this state when compared to the ground state; there are no new orbitals brought into the configuration space when the first excited state of the core is included. We then concluded that core excitation is not significant in ^{11}Li. This conclusion is in contrary to ^{12}Be (= ^{10}Be + n + n), a nucleus differing from ^{11}Li by a single proton, which has been studied within the same model [92]. There, the ground state and the first excited states of the ^{10}Be core have spins 0^+ and 2^+, respectively. Consequently, the model space of ^{12}Be is enlarged by inclusion of the first excited state of the core, and as expected, core excitation was found to be important in ^{12}Be. For reasons given in this paragraph and to avoid unnecessarily tedious discussions, we only present results for ^{11}Li built on the ground state of ^{9}Li.

2.3.2 ^{10}Li

In the three-body picture, one can not understand the Borromean nucleus ^{11}Li without a good description of its particle-unbound core + n subsystem ^{10}Li. The information on ^{10}Li is summarized in [99]. Therein, it is possible to see the large number of experiments that have been performed to measure the spectrum of ^{10}Li, but also the contradictory energy, parity, and spin assignments made.

Within the few-body picture, ^{10}Li is considered as a core + n system with a neutron above the ^{9}Li core. The extra neutron is allowed to live in orbits around the core labelled by nl_j, where n is the radial quantum number, l is the orbital momentum relative to the center-of-mass of the core, and $j = l \otimes s$ is the neutron's angular momentum with $s = 1/2$ being the neutron's internal spin. These orbits are assumed to be produced by a core-n potential to be defined later. Based on the experimental evidence and using the core + n decomposition, one can conclude the following regarding the low energy structure of ^{10}Li [99]:

1. The ground state of ^{10}Li contains a valence neutron in a $2s_{1/2}$ state at about +50 keV or below.

2. there is a $1p_{1/2}$ resonant state at several hundred keV, to be also referred to as the p-resonance. This resonance is often assumed to be around +500 keV [58].

3. There is no clear evidence for a d-state ($l = 2$) below +3 MeV. This state will be referred to as the d-resonance.

Along with other constraints, these observations are used to fix parameters of the core-n interaction.

2.3.3 Interactions

In this section, the potentials appearing in Eq. (2.22) used to bind ^{11}Li are discussed. In three-body models, the interaction between the two neutrons, V^{n-n}, is usually taken from a parameterization of the low energy nucleon-nucleon scattering phase shifts, which are well understood. For V^{n-n}, we use the soft-core Gogny interaction (also known as the GPT interaction) [109]. It includes central, tensor, spin-orbit, and spin-spin terms. The quadratic LL term is neglected since its effects are not strongly felt.

Most ambiguities reside in pinning down the effective interaction V^{core-n} between the ^{9}Li core and each neutron. In the following discussion, $\vec{r}_{core-n}$ stands for any of the two pair-wise coordinates between the core and the neutrons depicted in Figure 2.2. The form of the core-n interaction is based on the idea of the core being a rotor generating a deformed field. This field is taken as a deformed Woods-Saxon potential accompanied by a spin-orbit part proportional to a derivative of another non-deformed Woods-Saxon potential:

$$\begin{aligned} V^{core-n}\left(\vec{r}_{core-n},\xi\right) &= V_{ws}^{l}\left[1+\exp\left(\frac{r_{core-n}-R(\theta,\phi)}{a_{ws}}\right)\right]^{-1} - \left(\frac{\hbar}{m_{\pi}c}\right)^{2} \\ &\quad \left(2\vec{l}\cdot\vec{s}\right)\frac{V_{so}}{4r_{core-n}}\frac{\mathrm{d}}{\mathrm{d}r_{core-n}}\left[1+\exp\left(\frac{r_{core-n}-R_{so}}{a_{so}}\right)\right]^{-1}, \end{aligned} \tag{2.34}$$

where $\vec{l}$ is the operator of the orbital momentum between the core and a neutron, $\vec{s}$ is the operator of a neutron's spin, and m_{π} is the mass of a pion. For practical calculations, $(\hbar/(m_{\pi}c))^2 = 2.0$ fm^2. Both angular momentum operators are in units of $\hbar$.

The central Woods-Saxon part in Eq. (2.34) depends on the core's quadrupole deformation β_2 through the radius $R(\theta,\phi) = R_{ws}(\beta_2)[1+\beta_2 Y_{20}(\theta,\phi)]$, where θ and ϕ are spherical angles in the rest frame of the core. When $\beta_2 = 0$, a standard value $R_{ws} = 1.25A_{core}^{1/3} = 2.60$ fm is used [110], where A_{core} is the mass number of the core. When $\beta_2 \neq 0$, the radius parameter $R_{ws}(\beta_2)$ is adjusted to meet the volume conservation imposed on the central part of the interaction [10], and the dependence of R_{ws} on deformation is shown in Figure 2.3. In this and other figures, results are shown only up to $\beta_2 = 0.7$, a value that is unrealistically large. The spin-orbit term is left undeformed. Radius R_{so} was made equal to R_{ws} at any deformation. The diffusenesses are fixed to the standard value $a_{ws} = a_{so} = 0.65$ fm [110]. To increase the flexibility of the interaction, the depth V_{ws}^{l} of the central part depends on the relative orbital momentum l. Different

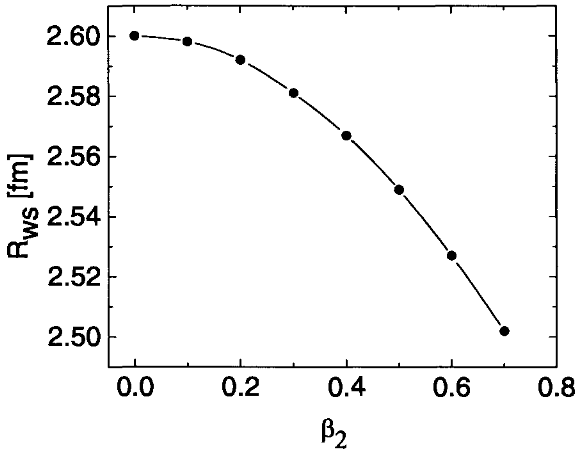

Figure 2.3: Radius of the ^{9}Li-n interaction as a function of deformation.

V^s_{ws} and V^p_{ws} are considered for $l = 0$ and 1, respectively, and the same V^d_{ws} is taken for all partial waves with $l \geq 2$. The depth V_{so} of the spin-orbit term is l-independent.

The rotor-like picture for ^{9}Li is probably an oversimplification, and thus we will not impose that the quadrupole deformation be determined by the strength of E2 transition between the ground state and the first excited state of the core, which in any case is not known. Therefore, in the three-body model of ^{11}Li the deformation parameter β_2 is a free parameter chosen from a physically reasonable interval. In principle, the deformation parameter can take negative values if the core is oblate. We found that the quadrupole force for oblate shapes of ^{9}Li produces more repulsion when compared to the prolate case and therefore less binding energy. For this reason, only the prolate deformation ($\beta_2 > 0$) of the ^{9}Li core is considered in what follows. It should be noted that the preference of a prolate deformation contradicts a recently measured negative quadrupole moment of ^{9}Li [111].

In case of an undeformed ^{9}Li, all J^π states in ^{10}Li originating from a given nl_j neutron orbital are degenerate. The degeneracy is, however, removed as soon as the spherical symmetry is broken by non-zero deformation. When there is deformation, l, j are no longer good quantum numbers, and a nuclear state $J^\pi(^{10}\text{Li})$ contains a superposition of different nl_j components coupled to the ground state of ^{9}Li with $J^\pi(^9\text{Li}) = 3/2^-$. Nevertheless, for simplicity, we will refer to any multi-component state $J^\pi(^{10}\text{Li})$, by the

nl_j component into which the state collapses in the limit of no deformation.

The depth of the core-n interaction can now be adjusted to reproduce low-lying levels in ^{10}Li. Because the experimental data on ^{10}Li from Section 2.3.2 is inconclusive about positions of the p- and d-resonances, these states can be moved around a bit to obtain reasonable results for ^{11}Li. In particular, to reproduce the experimental binding of ^{11}Li, we place the p-resonance in ^{10}Li at +400 keV. By comparison of ^{10}Li with ^{11}Be, a nucleus with the same number of neutrons, one would expect the d-resonance in ^{10}Li to be close to +2 MeV [112]. In this work, the d-resonance is placed at +3.4 MeV. If the d-resonance were at much higher energy, the three-body binding energy of ^{11}Li would not be reproduced; if it were at much lower energy, it would become bound more than the p-resonance at large deformations in contradiction to experimental data on ^{10}Li. The final restriction on the core-n interaction is that the interaction must produce the $1p_{3/2}$ orbital at -4.1 MeV to match the neutron separation energy of ^{9}Li. Under all these assumptions, the depths V_{ws}^l and V_{so} of the core-n interaction are adjusted so that the interaction produces a series of levels, lowest of which are shown in Figure 2.4 for the case of zero deformation. In the deformed cases, fitting the core-n potential means adjusting its depths so that the centroids of $1p_{3/2}$, $2s_{1/2}$, $1p_{1/2}$ and $1d_{5/2}$ orbitals are kept at -4.1 MeV, +50 keV, +400 keV and +3.4 MeV, respectively. The variation of potential depths with deformation is finally shown in Figure 2.5. The corresponding two-body bound states and the lowest resonances in ^{10}Li are shown in Figure 2.6 and Figure 2.7, respectively. We note that, with this choice of the core-n and n-n potentials, no three-body force is needed to reproduce the three-body binding energy of ^{11}Li.

Finally, in order to approximately satisfy the exclusion principle, the bound $1s_{1/2}$ and $1p_{3/2}$ neutron orbitals are projected out of the model space before diagonalization [65].

2.3.4 Results

Calculations were performed using the computer code EFADD [113]. The full model space in Eq. (2.21) contained all valence terms with $n_{lag} \leq 18$ and $K \leq 22$. The hyper-radial

E_{2body}	nl_j	$J^{\pi}(^{10}\text{Li})$	
+3.4 MeV	$1d_{5/2}$	$1^-, 2^-, 3^-, 4^-$	allowed levels
+400 keV	$1p_{1/2}$	$1^+, 2^+$	
+50 keV	$2s_{1/2}$	$1^-, 2^-$	
-4.1 MeV	$1p_{3/2}$	$0^+, 1^+, 2^+, 3^+$	forbidden levels
	$1s_{1/2}$	$1^-, 2^-$	

Figure 2.4: The lowest energy levels in ^{10}Li produced by the core-n interaction. It is assumed that the valence neutron is coupled to the $J^{\pi} = 3/2^-$ ground state of ^{9}Li and that the ^{9}Li core is undeformed, i.e. $\beta_2 = 0$. The levels, energies of which are shown, were used to restrict parameters of the core-n interaction. The two lowest levels, $1s_{1/2}$ and $1p_{3/2}$, are forbidden for valence neutrons in ^{10}Li and need to be projected out of the valence model space. The other orbitals are free to be occupied by valence neutrons.

Laguerre functions reach out to the maximum hyper-radius 20 fm.

Figure 2.8 shows the convergence of the three-body binding energy of ^{11}Li with the size of the model space measured by the maximum hyper-momentum. The figure contains three sets of results corresponding to $\beta_2 = 0.0, 0.3$ and 0.6. On one hand, the convergence exhibits the well known exponential dependence when $K_{max} \gtrsim 12$ for all deformations studied. On the other hand, in all cases, the convergence rate is very slow, much slower than in the ^{12}Be case [92]. Moreover, the convergence rate decreases with increasing

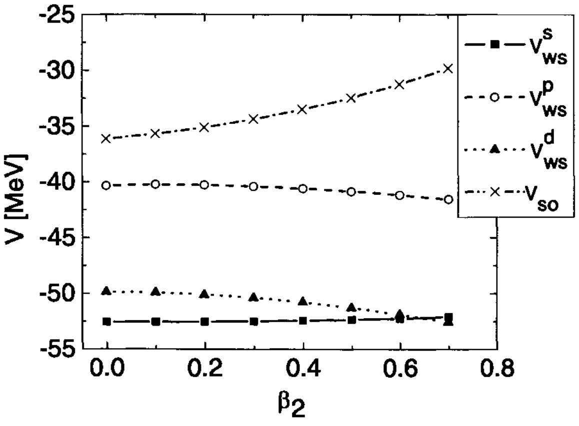

Figure 2.5: Depths of the fitted ^{9}Li-n interaction as a function of deformation.

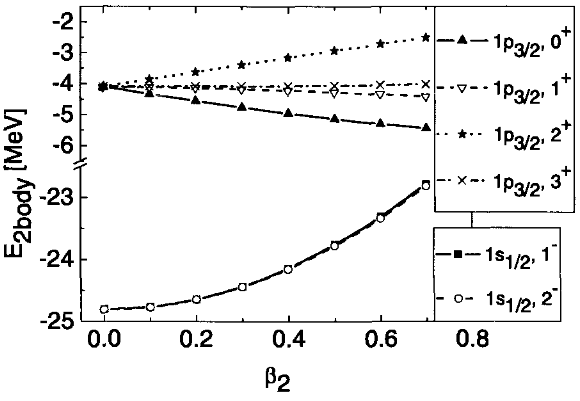

Figure 2.6: Two-body binding energy of bound states in ^{10}Li as a function of deformation. The legend refers to nl_j valence neutron orbitals (coupled to the $3/2^-$ ground state of ^{9}Li) and the total spin of ^{10}Li.

deformation. It is thus necessary to use extrapolated energy values for three-body binding energies.

The three-body binding energy of ^{11}Li as a function of deformation is presented in Figure 2.9. The figure contains both the values for the maximum hyper-momentum $K_{max} = 22$ and those obtained through the extrapolation in K_{max}. Contrary to the case of ^{12}Be where the energy gain was large, in ^{11}Li a very small additional binding is obtained from the quadrupole coupling, and as the deformation becomes large the system

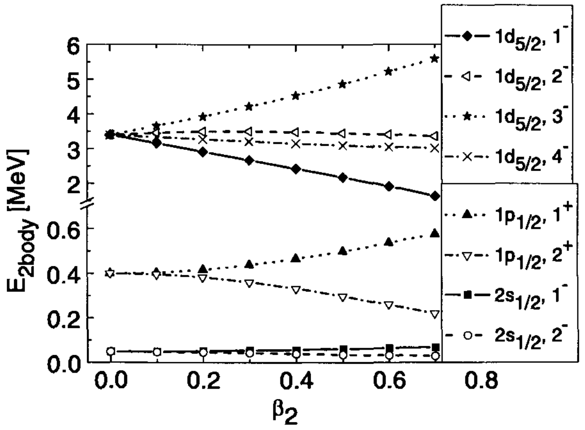

Figure 2.7: Two-body binding energy of continuum states in ^{10}Li as a function of deformation. The legend refers to nl_j valence neutron orbitals (coupled to the $3/2^-$ ground state of ^{9}Li) the and total spin of ^{10}Li. Both s-wave states refer to virtual states while the other states correspond to real resonances.

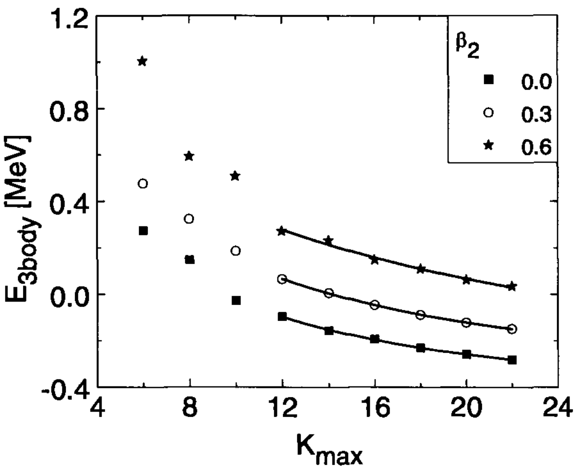

Figure 2.8: Dependence of the three-body binding energy of ^{11}Li on the size of the model space determined by the maximum hyper-momentum K_{max} included in calculations. For any K_{max}, all possible valence channels with $K \leq K_{max}$ are included in the wavefunction. The lines are exponential fits to the tails of data sets.

becomes less bound.

The rms matter radii of the corresponding wavefunctions are shown in Figure 2.10. To compute the matter radii of ^{11}Li, the rms matter radius 2.32 fm of the ^{9}Li core was used in Eq. (2.29) [13]. In Figure 2.10, the matter radii were obtained for the maximum hyper-momentum $K_{max} = 22$, but their variations between $K_{max} = 20$ and $K_{max} = 22$ were less than 1%. The experimental three-body binding energy and the rms matter radius impose a constraint on values of the deformation parameter, namely $\beta_2 \lesssim 0.3$. We note that the extrapolation was only done for three-body binding energies since it is the only observable that has a well established exponential dependence on K_{max}. Our prediction for the rms proton radius obtained for $\beta_2 = 0.3$ is $\langle r_p^2 \rangle^{1/2} = 2.37$ fm in agreement with the recent measurement of the charge radius of ^{11}Li [48].

Figure 2.11 shows the probabilities to find the three main structural components in the ground state of ^{11}Li, namely $(s_{1/2})^2$, $(p_{1/2})^2$ and $(d_{5/2})^2$ components. Here, jj coupling scheme $(l_{xjx})(l_{yjy})$ in the Y Jacobi basis is used (see Figure 2.1): l_x and l_y are orbital momenta along Jacobi vectors $\vec{x}$ and $\vec{y}$, and j's are orbital momenta l coupled to spins of neutrons sitting at the ends of corresponding Jacobi vectors. When the deformation of the core is small, the ground state of ^{11}Li is almost 60% $(p_{1/2})^2$; for large deformations

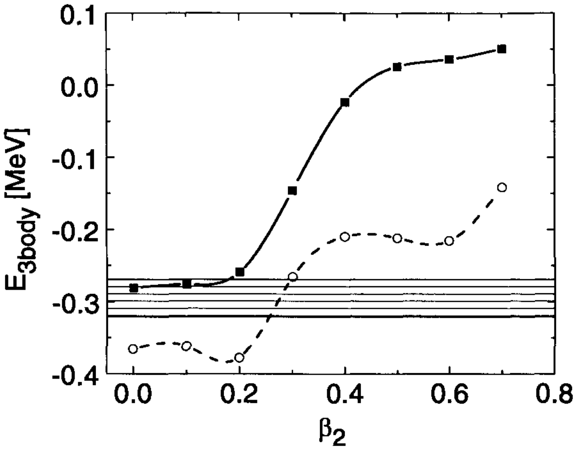

Figure 2.9: Three-body binding energy of ^{11}Li as a function of deformation. The squares correspond to values obtained for $K_{max} = 22$, the circles are values obtained through the extrapolation in K_{max} for $K_{max} \geq 12$. Lines are to guide the eye. Shaded region corresponds to experimental value 295 ± 26 keV [101].

it becomes more than 80% $(s_{1/2})^2$. The region around $\beta_2 = 0.3$ corresponds to the transition between these two configurations where both components are populated with equal probability. Regardless of the deformation, the weight of the $(d_{5/2})^2$ configuration is small, less than about 7%. This result is in contrast with the three-body calculations for ^{12}Be in [92] where the $(d_{5/2})^2$ configuration accounts for about 30% in the ground state of ^{12}Be.

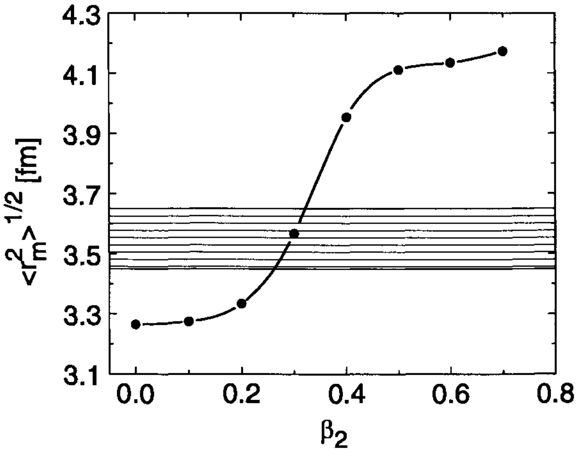

Figure 2.10: Rms matter radius of ^{11}Li as a function of deformation. The squares correspond to values obtained for $K_{max} = 22$, the line is to guide the eye. Shaded region corresponds to the value consistent with reaction data [54].

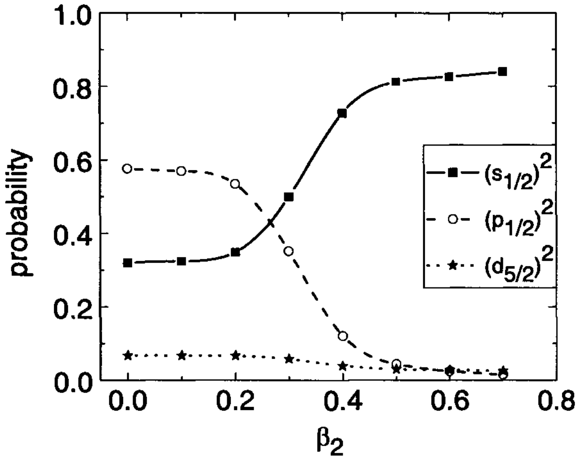

Figure 2.11: Probabilities of the three main structural components in the ground state of ^{11}Li as a function of deformation. The lines are to guide the eye.

One has to realize that there is no unique parameterization for the effective core-n interaction. We have convinced ourselves, though, that the features shown here for the structure of the ground state of ^{11}Li do not result from a specific parameterization. Rather, the main features emerge from the constraints imposed on continuum states in ^{10}Li. Other interaction parameterizations, using different interaction radii or spin-orbit parameters, produce exactly the same characteristics of ^{11}Li.

It is important to understand the implications of the ^{10}Li structure on ^{11}Li. Despite the large number of experiments, a close study of [99] raises questions about the precision with which states in ^{10}Li are known. We have explored the possibility of different assumptions for the neutron states to which the core-n interaction is fitted, namely $2s_{1/2}$ at +50 keV; $1p_{1/2}$ at +400 keV and $1d_{5/2}$ at +3.4 MeV. Of these, the least uncertain is the $2s_{1/2}$ state. We have checked that the main features of the present work are not changed by moving the $1p_{1/2}$ neutron orbital to +500 keV. More important is the uncertainty in the location of the $1d_{5/2}$ state. There is no clear experimental evidence for a d-resonance at +3.4 MeV or at any lower energy. If the d-resonance is broad or it is superposed by other states, it could be hard to observe experimentally. What happens if the d-resonance is pushed down? We refitted the core-n interaction for deformation $\beta_2 = 0.3$, fixing the centroid of the d-resonance at +2.5 MeV. An immediate consequence is a gain in three-body binding in ^{11}Li of about 150 keV. However this additional attraction would not be sufficient to change the structure of the ground state of ^{11}Li, which would remain essentially $(s_{1/2})^2$ and $(p_{1/2})^2$, with $(d_{5/2})^2$ accounting only for about 10%.

2.3.5 Conclusions

We performed three-body calculations for the ground state of ^{11}Li including deformation and excitation of ^{9}Li. We find that reorientation effects due to core deformation can account for the known configuration admixture of s-waves and p-waves in ^{11}Li. With a three-body model, in which the core is treated as a deformed rotor, it is possible to reproduce the three-body binding energy, the rms matter radius, the rms proton radius, and the structure of ^{11}Li consistent with experiment. On the other side, core excitation is found to be unimportant. In the three-body model, the strength of d-waves in ^{11}Li is predicted to be very small ($\approx 7\%$), which is in disagreement with shell-model calculations [50]. So far, experiments have not been able to make a clear statement about the position of the d-resonance in ^{10}Li. In the three-body calculations, we have assumed that such a resonance would be above +3 MeV; however, the shell model produces this state at a much lower energy around 2 MeV [50]. Resolving experimentally the position of d-states in ^{10}Li will settle once and for all the structure of the ground state of ^{11}Li. Such an experiment should be done with a reaction starting from ^{9}Li rather than knock-out from ^{11}Li since there is not much d-waves in ^{11}Li. One possibility would be to repeat the ^{9}Li(d,p)^{10}Li experiment [114] at a higher beam energy.

2.4 ^{6}He in the three-body model

In this section, we repeat some calculations for ^{6}He published in [94]. The goal is to gain access to three-body results for ^{6}He and have them available for a comparative study with the outcome of MiCH for this nucleus in Chapter 5. The main purpose of the original three-body paper [94] was to investigate three-body continuum structure and response functions in ^{6}He, but as part of the work the wavefunction for the ground state of ^{6}He was constructed as well. In that work, hyper-spherical expansion and Pauli blocking along the lines described in this chapter were employed. The ground state of ^{6}He in the cited work is regarded as possibly the best within the formalism presented in this chapter [115].

2.4.1 Introduction

The nucleus ^{6}He, the lightest of the two-neutron halo nuclei, has been used throughout the years as a reference nucleus in the realm of Borromean nuclei. This nucleus has been tackled in a variety of models, ranging from three-body [13, 94, 116] through microscopic cluster [76, 78, 79] to fully microscopic models [69, 117]. Because of the fairly simple structure of ^{6}He, many theoretical models are in agreement on the bulk properties of the ground state, such as binding energies, radii and the occurrence of halo structure. However, as will be demonstrated in Chapter 5, one needs to look deeper to find discrepancies between different models. Here, we focus on the three-body description of this nucleus.

In the three-body picture, ^{6}He in its ground state is considerably simpler to tackle than ^{11}Li. In fact, ^{6}He is probably the two-neutron halo nucleus on which any three-body model would stand the most firmly for several reasons. First, a free ^{4}He is exceptionally well bound among light nuclei, its $J^\pi = 0^+$ ground state has zero quadrupole moment, and the first excited state (also 0^+) is above 20 MeV [118]. Moreover, from the microscopic point of view, ^{4}He is a fairly simple object: in a first approximation, ^{4}He contains four nucleons in the lowest possible spherical $1s_{1/2}$ mean-field orbit. Here, the nl_j notation from Section 2.3.2 is used. Within the three-body approximation, it is then reasonable to assume that ^{4}He remains hardly polarized in ^{6}He, even though this assumption may contradict conclusions of some microscopic models in which distortion of the core in ^{6}He has been found important [76]. Thus, in three-body calculations of ^{6}He, we consider the ^{4}He core only in its non-deformed ground state. Second, the core-n potential can be conveniently fitted to experimentally known scattering phase shifts. But there is no such thing as a free lunch: even with the core-n interaction fitted to scattering data, ^{6}He suffers from underbinding, as will be shown in Section 2.4.2. Third, ground states of both

^{4}He and ^{6}He are $J^\pi = 0^+$ objects which considerably decreases the number of valence channels open for the two extra neutrons. Finally, the $1s_{1/2}$ neutron orbital (consequently the lowest $J^\pi = 1/2^+$ state of ^{4}He+n subsystem) produced by the core-n potential is the only one that needs to be projected out of the valence model space.

2.4.2 Interactions

The two-body interactions from Eq. (2.22) are adjusted as follows. The ^{4}He-n interaction V^{core-n} combines a central Woods-Saxon and a spin-orbit Woods-Saxon-derivative parts as in Eq. (2.34). The nuclear field is spherically symmetric because the core is undeformed. Parameters of the core-n interaction are taken from [94]: $R_{ws} = 2.0$ fm, $R_{so} = 1.5$ fm, $a_{ws} = 0.7$ fm, $a_{so} = 0.35$ fm, $V_{ws}^s = V_{ws}^p = -43.0$ MeV, $V_{ws}^d = -21.5$ MeV, $V_{so} = -40.0$ MeV. The core-n interaction is zero for partial waves with $l > 2$. This interaction reproduces α-n scattering phase shifts satisfactorily. As for the interaction between valence neutrons V^{n-n}, a realistic Gogny (GPT) force is used [109].

With these two-body interactions, the three-body model of ^{6}He suffers from the problem of underbinding [13,116]. It is commonly argued that physics underlying the problem of insufficient three-body binding may have to be explored beyond three-body models. Possible reasons for underbinding include polarization of the core and the influence of closed channels, most important of which is ^{3}H+^{3}H; use of local energy-independent potentials neglecting exchange interactions that would be introduced through antisymmetrization effects; and two-body interactions may not be the same in the presence of the third cluster as those in a free space. To cure the underbinding problem in [94], an effective three-body force was introduced:

$$V^{3body} = \frac{-1.50}{1 + (\rho/5.0)^3}\ [\text{MeV}] \tag{2.35}$$

to simulate the effects of the closed ^{3}H+^{3}H channel.

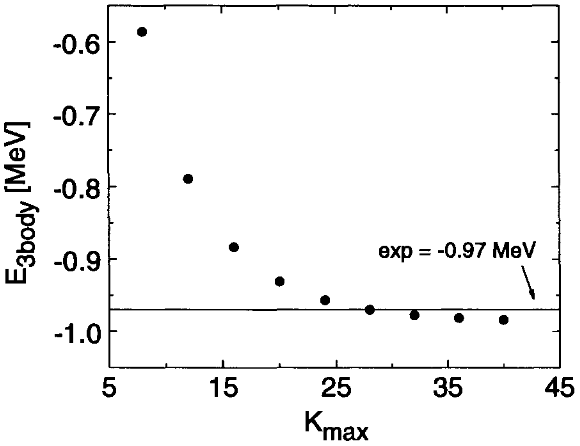

Figure 2.12: Dependence of the three-body binding energy of ^{6}He on the size of the model space determined by the maximum hyper-momentum K_{max} included in calculations. For each point, all possible valence channels with $K \leq K_{max}$ are included in the wavefunction.

2.4.3 Results

In this section, some results for ^{6}He studied in the three-body model are presented; the rest of the discussion will be delayed until Chapter 5. Because the three-body calculations of ^{6}He are computationally cheap compared to the case of ^{11}Li in Section 2.3, we can consider a much larger model space than for ^{11}Li. The wavefunction for ^{6}He is written in the T Jacobi basis, and all hyper-radial Laguerre basis functions with $n_{lag} \leq 25$ are included.

The convergence of the three-body binding energy of ^{6}He with the size of the model space determined by the maximum hyper-momentum K_{max} is shown in Figure 2.12. For $K_{max} = 40$, the three-body binding energy is -0.98 MeV, a value that would also be obtained from an exponential fit to the high-K_{max} tail of data points in Figure 2.12. Therefore, results for $K_{max} = 40$ are considered converged.

For the converged state, the weights of the five dominant valence configurations in the T Jacobi basis are shown in Table 2.1. As we explained in Section 2.1, hyper-radial basis states do not have a well defined physical meaning. Therefore, the weights in the table were summed over n_{lag} for a given combination $\{K, l_x, l_y, L, S\}$. The five configurations account for nearly the entire wavefunction. However, this group of components is by itself

Table 2.1: Probabilities of the five dominant components in the T Jacobi basis in the ground state of ^{6}He. Here, l_x and l_y are orbital momenta associated with Jacobi coordinates $\vec{x}$ and $\vec{y}$ from Figure 2.1, L and S are the total orbital momentum and spin of the valence part of the wavefunction, as in Eq. (2.18).

T Jacobi basis						
alias	K	l_x	l_y	L	S	probability [%]
$K = 2$ s-waves	2	0	0	0	0	80.89
$K = 2$ p-waves	2	1	1	1	1	11.03
$K = 0$ s-waves	0	0	0	0	0	4.17
$K = 6$ d-waves	6	2	2	0	0	1.64
$K = 6$ f-waves	6	3	3	1	1	0.78
					$\sum =$	98.51

not large enough to deliver converged results, as can for example be seen from Figure 2.12 where the three-body binding energy for $K_{max} = 8$ is about 400 keV above its converged value. The ground state of ^{6}He is controlled by $K = 2$ valence components. The spin-singlet ($S = 0$) valence configurations account for about 86.7% of the wavefunction; the admixed spin-triplet ($S = 1$) components exist only due to a spin-orbit coupling.

Similarly, the probabilities of dominant configurations in the Y Jacobi basis are shown in Table 2.2. In the Y Jacobi basis, the ground state of ^{6}He is dominated by valence terms with $l_x = 1$, i.e. by terms in which the valence neutrons orbit the core in relative p-waves in agreement with the shell-model picture where the lowest p-shell is the first shell available for valence neutrons outside the ^{4}He core.

Figure 2.13 shows the hyper-radial dependence of valence configurations from Table 2.1. Again, for a given valence configuration, hyper-radial dependences were summed over n_{lag} and multiplied by a factor $\rho^{-5/2}$ to bring them to the form $u(\rho)$ introduced in Eq. (2.11). This form of hyper-radial functions is preferred because of its simpler asymptotic properties from Eq. (2.14) and Eq. (2.15). As expected, all hyper-radial functions vanish at small hyper-radii. Probabilities of valence configurations in Table 2.1 were obtained by integrating squared hyper-radial functions from Figure 2.13 over the hyper-radius.

Further discussion on ^{6}He is postponed until Chapter 5 where the three-body results

Table 2.2: Probabilities of the three dominant components in the Y Jacobi basis in the ground state of ^{6}He. Here, jj coupling is used. Schematically $j_i = l_i \otimes s_i$, $i = x, y$, where l_i are orbital momenta associated with Jacobi vectors $\vec{x}$ and $\vec{y}$ in the Y Jacobi basis in Figure 2.1 and s_i are spins of neutrons sitting at the ends of corresponding Jacobi vectors.

Y Jacobi basis				
l_x	j_x	l_y	j_y	probability [%]
1	3/2	1	3/2	85.01
0	1/2	0	1/2	7.83
1	1/2	1	1/2	5.79
			$\sum =$	98.63

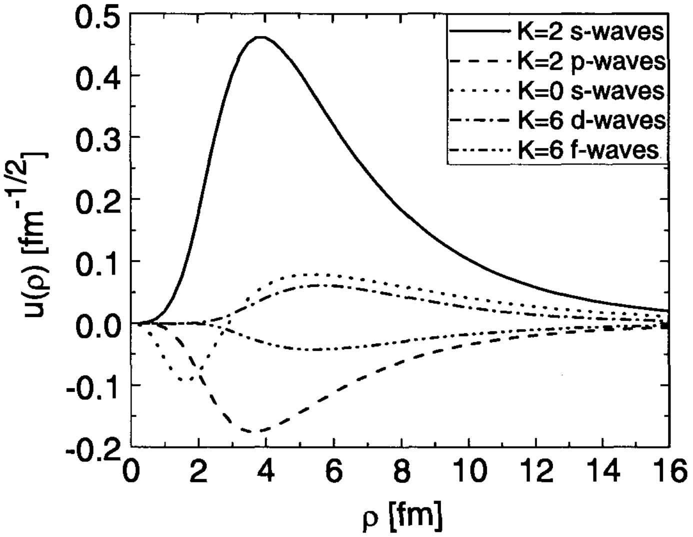

Figure 2.13: Hyper-radial dependence of the five dominant channels from Table 2.1 in the three-body wavefunction of ^{6}He.

will be compared with those obtained in MiCH.

Chapter 3

Core

In the previous chapter, the formalism for the valence part attached to a macroscopic core was outlined. The three-body-like construction of the valence part should guarantee the proper Borromean asymptotics of the wavefunction. To develop MiCH further, we now wish to find a suitable microscopic model for the core to replace the core's macroscopic representation in Eq. (2.21).

Let us start the search for the core's model by defining our needs. First, for the purposes of the present work, we need a microscopic model of ^{4}He. Our ultimate future goal, however, is to tackle heavier two-neutron halo nuclei, especially ^{11}Li. Therefore, to have MiCH developed in a unified fashion, the model for the core should be capable to describe heavier cores, such as ^{9}Li. However, in the light of upcoming chapters, there is a risk of running into computational difficulties for systems heavier than ^{6}He. It is known that the size of calculations in microscopic models grows rapidly with mass number. In fact, some models such as Green's function Monte Carlo are currently limited to masses $A \leq 12$ [67] due to computational demand. For future applications, the model for the core needs to be flexible enough to provide either a fully microscopic or microscopic cluster picture of the core. In the later version, the core would be built from microscopic clusters with some internal degrees of freedom frozen. Second, the core's model should provide reasonably accurate structure information so that we can focus on effects due to the valence particles. This constraint requires a certain level of sophistication in the description of the core. Third, the model must handle central as well as non-central nucleon-nucleon forces. This requirement is important because the studied two-neutron halo nuclei lie outside of the lowest s-shell in the region where non-central forces are known to play an important role. Fourth, unlike for the valence part, there is no need to impose special asymptotic requirements on the core's wavefunction, because all potential cores are tightly bound systems. Last, the wavefunction of the core should be expressed completely in Jacobi coordinates. Along with the valence part given in terms of Jacobi coordinates, fulfilment of this constraint removes by construction the spurious center-of-mass motion.

At first sight, the literature is very rich in microscopic structure models of light nuclei, some of which were mentioned in Chapter 1. In [119], several sophisticated models were applied to ^{4}He bound by the realistic AV8' nucleon-nucleon force [120] and their results were found to be essentially the same. Models tested in [119] (see references therein) include: the Faddeev-Yakubovsky method, the coupled-rearrangement-channel Gaussian-basis variational model, the stochastic variational model, the hyper-spherical variational model, the Green's function Monte Carlo, the no-core shell model, and the effective interaction hyper-spherical harmonic method. Many microscopic structure models mentioned in Chapter 1 and [119] meet some of the criteria imposed above on microscopic treatment of the core, but the pool of models meeting all of them is very limited. The most restrictive requirement turns out to be usage of Jacobi coordinates. From all the mentioned structure models, the stochastic variational model meets all our criteria. The rest of this chapter is dedicated to this model.

3.1 Stochastic variational model

As its name suggests, the stochastic variational model (SVM) represents a variational approach to many-body problems. SVM relies on the expansion of wavefunctions in terms of functionally simple basis states and a stochastic optimization of variational parameters. The original idea of stochastic optimization appeared in [121]. Later, the method was improved further [74, 122]. The basis functions used in the original and later version are different, though. Hereafter, we shall by SVM refer to the later version of the model. SVM has been also applied to a variety of problems in other branches of physics [123]. There are two versions of the model, differing by the treatment of the angular part of the wavefunction: vector-coupled and global. Following [124], the vector-coupled version of SVM is used in the present work.

In this section, a microscopic version of SVM applied to the core nucleus in ^{6}He, ^{4}He, is described first. This version of the model has been used to calculate properties of nuclear systems with mass numbers less than eight bound by effective central nucleon-nucleon interactions [74]. Later, the method was extended to include non-central nucleon-nucleon interactions. Properties computed for ^{3}H and ^{4}He bound by non-central forces agreed with those from other microscopic structure models [119, 125]. There also exists a microscopic cluster version of SVM, which has been applied to somewhat heavier nuclear systems, and which potentially could be used to describe ^{9}Li core in ^{11}Li studied within MiCH. The microscopic cluster version of the model is outlined at the end of this section.

The accuracy of any variational method crucially depends on the choice of trial wavefunctions. SVM prefers correlated Gaussians [126, 127] as trial variational basis functions. Before their adoption in SVM, these functions proved to be remarkably flexible in various few-body calculations, mainly in atomic and molecular physics, see for example [128, 129]. Also, the basis of correlated Gaussians allows analytical computation of many matrix elements and is easily adaptable to the permutational symmetry of fermionic systems.

In principle, any one-body square-integrable function of vector $\vec{r}$ and with angular momentum l and its projection m can be approximated to any accuracy by a linear combination of Gaussians of continuous size parameter a:

$$\exp\left(-\frac{1}{2}ar^2\right)\mathcal{Y}_{lm}(\vec{r}), \qquad \mathcal{Y}_{lm}(\vec{r}) = r^l\, Y_{lm}(\Omega_r), \tag{3.1}$$

where $\mathcal{Y}_{lm}$ and Y_{lm} are solid and spherical harmonics, respectively, and Ω_r comprises the polar and azimuthal angles associated with $\vec{r}$. The radial factor in solid harmonics improves the short-range behavior of basis states. This simple observation for a single particle can be easily generalized to an A-body problem in either an uncorrelated or a correlated fashion [130]. In an uncorrelated approach, the many-body basis states would consist of Slater determinants of single-particle Gaussian packets; in a correlated approach, inter-particle correlations are explicitly built into basis states.

SVM follows the correlated approach and employs basis states expressed fully in Jacobi coordinates. Jacobi coordinates for a four-particle system are defined in Figure 3.1. Being relative coordinates, Jacobi coordinates not only engage inter-particle correlations, but also make the removal of the spurious motion of the center of mass trivial. Then, a non-antisymmetrized basis term for ^{4}He in either K- or H-like Jacobi basis is written as:

$$\begin{aligned}\phi_{\gamma_{core} J^{\pi}_{core} T_{core} M_{T_{core}}}(\vec{x}, \boldsymbol{A}) = {} & \exp\left(-\frac{1}{2}x\boldsymbol{A}x\right) \times \\ & \left[\theta_{l_1 l_2 l_3 L_{12} L}(\vec{x}) \otimes \chi_{S_{12} S_{123} S}\right]_{J^{\pi}_{core}} \times \\ & \tau_{T_{12} T_{123} T_{core} M_{T_{core}}},\end{aligned} \tag{3.2}$$

where J^{π}_{core} denotes the total angular momentum and the parity of the state, T_{core} and $M_{T_{core}}$ are the total isospin and its projection. The projection of J_{core} is suppressed for clarity. Index γ_{core} comprises all other quantum numbers as well as the Jacobi channel identifier K or H, i.e. $\gamma_{core} = \{l_1, l_2, l_3, L_{12}, L, S_{12}, S_{123}, S, T_{12}, T_{123}, \mathrm{K/H}\}$. The function $\theta_{l_1 l_2 l_3 L_{12} L}(\vec{x})$ is chosen as a vector-coupled product of solid harmonics of relative Jacobi coordinates:

$$\theta_{l_1 l_2 l_3 L_{12} L}(\vec{x}) = \left[\left[\mathcal{Y}_{l_1}(\vec{x}_1) \otimes \mathcal{Y}_{l_2}(\vec{x}_2)\right]_{L_{12}} \otimes \mathcal{Y}_{l_3}(\vec{x}_3)\right]_L . \tag{3.3}$$

The spin $\chi_{S_{12} S_{123} S}$ and isospin $\tau_{T_{12} T_{123} T_{core} M_{T_{core}}}$ parts consist of successively coupled single-particle spins and isospins:

$$\chi_{S_{12}S_{123}S} = \left[\left[\left[\chi_{p_1} \otimes \chi_{p_2}\right]_{S_{12}} \otimes \chi_{p_3}\right]_{S_{123}} \otimes \chi_{p_4}\right]_S, \tag{3.4}$$

$$\tau_{T_{12}T_{123}T_{core}M_{T_{core}}} = \left[\left[\left[\tau_{p_1} \otimes \tau_{p_2}\right]_{T_{12}} \otimes \tau_{p_3}\right]_{T_{123}} \otimes \tau_{p_4}\right]_{T_{core}M_{T_{core}}}. \tag{3.5}$$

The projection number $M_{T_{core}}$ is fixed by the number of protons and neutrons in the nucleus. Constrained by vector coupling, different sets of orbital momenta $\{l_1, l_2, l_3, L_{12}, L\}$, spins $\{S_{12}, S_{123}, S\}$, and isospins $\{T_{12}, T_{123}, T_{core}\}$ may exist and they shall be referred to as different orbital, spin, and isospin channels, respectively.

The Gaussian part in Eq. (3.2) deserves closer attention. The symbol $\boldsymbol{A}$ stands for a 3×3 dimensional positive-definite, symmetric matrix of non-linear parameters, specific to each basis element. The quadratic form $x\boldsymbol{A}x$ involves scalar products of Jacobi vectors:

$$x\boldsymbol{A}x \equiv \sum_{i,j=1}^{A_{core}-1} \boldsymbol{A}_{ij}\vec{x}_i \cdot \vec{x}_j \tag{3.6}$$

with $A_{core} = 4$ being the mass number of the core nucleus. Due to the symmetricity requirement, the number of independent elements in matrix $\boldsymbol{A}$ is $A_{core}(A_{core} - 1)/2 = 6$. Also notice that, due to dimensions of matrix $\boldsymbol{A}$, the summation in Eq. (3.6) goes only up to $A_{core} - 1 = 3$ which prevents the A_{core}-th Jacobi coordinate $\vec{x}_4$, the position of the center of mass of the nucleus, to enter calculations. The Gaussian argument can also be written in a slightly different form:

$$x\boldsymbol{A}x = \sum_{i<j=1}^{A_{core}} \alpha_{ij}\left(\vec{r}_{p_i} - \vec{r}_{p_j}\right)^2 \tag{3.7}$$

with a simple relationship between elements of matrix $\boldsymbol{A}$ and coefficients α:

$$\alpha_{ij} = -\sum_{k=1}^{A_{core}-1}\sum_{l=1}^{A_{core}-1} \boldsymbol{U}_{ki}\boldsymbol{A}_{kl}\boldsymbol{U}_{lj}, \qquad i<j, \tag{3.8}$$

where $\boldsymbol{U}$ is a transformation matrix introduced in Figure 3.1. All coefficients α are non-

Let us consider a system of four identical particles $p_i, i = 1, 2, 3, 4$ at positions $\vec{r}_{p_i}$ in laboratory frame. Then, there are two different—K- and H-like—sets of Jacobi coordinates $\vec{x} = \{\vec{x}_j, j = 1, 2, 3, 4\}$:

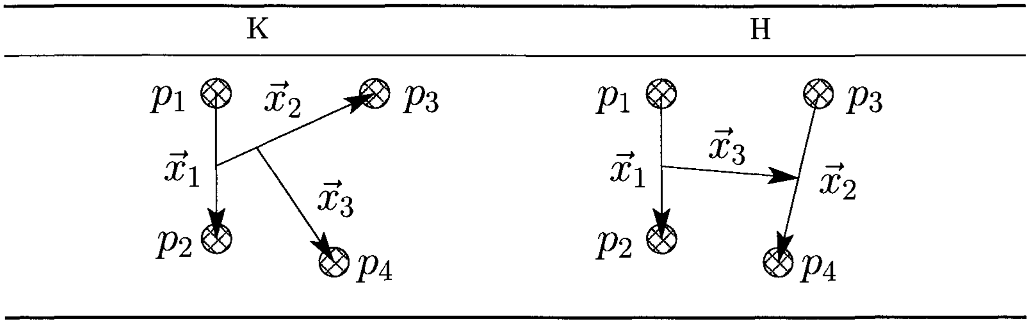

The first three Jacobi coordinates are relative coordinates: they originate and terminate at centers of masses of subgroups of particles they connect. The last Jacobi coordinate $\vec{x}_4$ (not shown in the graphics) is the same in the two Jacobi sets and is equal to the position of the center of mass of the four-particle system in the laboratory frame. Jacobi and single-particle coordinates are related simply as:

$$\vec{x}_i = \sum_{j=1}^{4} \boldsymbol{U}_{ij} \vec{r}_{p_j}$$

with the transformation matrix $\boldsymbol{U}$ being:

K	H
$\begin{pmatrix} -1 & 1 & 0 & 0 \\ -1/2 & -1/2 & 1 & 0 \\ -1/3 & -1/3 & -1/3 & 1 \\ 1/4 & 1/4 & 1/4 & 1/4 \end{pmatrix}$	$\begin{pmatrix} -1 & 1 & 0 & 0 \\ 0 & 0 & -1 & 1 \\ -1/2 & -1/2 & 1/2 & 1/2 \\ 1/4 & 1/4 & 1/4 & 1/4 \end{pmatrix}$

Figure 3.1: Definition of Jacobi coordinates for a system of four identical particles.

negative, and their number equals to the number of independent elements in matrix $\boldsymbol{A}$. The advantage of coefficients α is that, unlike elements of $\boldsymbol{A}$, they scale directly interparticle distances in the Gaussian and thus provide better intuitive feeling for the size of the nucleus. This advantage is useful during the process of parameter optimization.

The Gaussian in Eq. (3.2) as a whole is a spherically symmetric object. However, as long as the matrix $\boldsymbol{A}$ is non-diagonal, the Gaussian carries angular information due to cross terms $\vec{x}_i \cdot \vec{x}_j$. The power series expansion of $\exp(-\boldsymbol{A}_{ij} \vec{x}_i \cdot \vec{x}_j)$ contains high powers of $\vec{x}_i \cdot \vec{x}_j$, which can describe higher partial waves associated with the coordinates $\vec{x}_i$ and

$\vec{x}_j$. In such a case, quantum numbers l_1, l_2, l_3 in $\theta_{l_1 l_2 l_3 L_{12} L_{123} L}(\vec{x})$ loose their meaning of orbital momentum quantum numbers for a given basis state, and can be considered discrete variational parameters, instead.

The full wavefunction is then written as an antisymmetrized linear combination of basis sets from Eq. (3.2):

$$\Phi_{J^\pi_{core} T_{core} M_{T_{core}}} = \mathcal{A}^{core} \sum c^{\boldsymbol{A}}_{\gamma_{core} J^\pi_{core} T_{core} M_{T_{core}}} \phi_{\gamma_{core} J^\pi_{core} T_{core} M_{T_{core}}}. \tag{3.9}$$

Here, $\mathcal{A}^{core}$ is the antisymmetrization operator which runs over all permutations of particles inside the nucleus, i.e. $\mathcal{A}^{core} = \sum_1^{A_{core}!}(-1)^p P$ with P being the permutation operator and p being the permutation parity. The sum in Eq. (3.9) is left without any summation index because the wavefunction is constructed stochastically as will be explained below. Due to the stochastic optimization, there may be several basis terms present in the wavefunction with exactly the same combination of γ_{core} and differing only by $\boldsymbol{A}$. Therefore, the linear coefficient c in Eq. (3.9) must also carry the $\boldsymbol{A}$-matrix index.

The nuclear Hamiltonian for the core nucleus includes kinetic energies of all nucleons T_i and nucleon-nucleon potentials V_{ij}:

$$H = \sum_{i=1}^{A_{core}} T_i + \sum_{1=i<j}^{A_{core}} V_{ij}. \tag{3.10}$$

Note that the kinetic energy of the total center of mass does not need to be subtracted, because such component is removed by construction of basis terms in Eq. (3.2). Linear expansion coefficients c in Eq. (3.9) can be obtained through the energy matrix diagonalization in Eq. (2.25). To do that, the wavefunction in Eq. (3.9) is written schematically as $\Phi = \sum_i c_i \Phi_i$, and energy and overlap matrix elements are computed as in Eq. (2.26) with the Hamiltonian from Eq. (3.10).

It is instructive to visualize the effects of the antisymmetrizer $\mathcal{A}^{core}$ on the wavefunction in Eq. (3.9). To do that, a new set of vectors, a set of spots $\vec{r}_i, i = 1, 2, 3, 4$, is defined.

For the non-antisymmetrized system of particles, spots coincide with single-particle vectors, that is $\vec{r}_i = \vec{r}_{p_i}$. When the antisymmetrizer is invoked, spots are not affected, but particles are: in particle permutations, particles are moved around between spots. As a consequence, each particle index in the definition of Jacobi coordinates in Figure 3.1 and also in Eq. (3.2) needs to be replaced by an index of the spot hosting that particle in a given permutation. This way, not only single-particle spins and isospins travel between spots, but also Jacobi coordinates are changed. As an example, the permutation swapping particles 2 and 3 causes the following reorientation of Jacobi vectors:

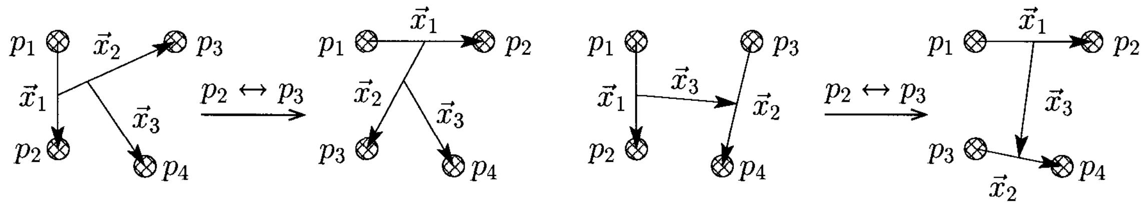

Through the distinction of particles and spots, the wavefunction automatically adjusts itself to the action of the antisymmetrizer. Once the antisymmetrizer has been completely executed, spot indexes are the only ones prevailing, while all particle indexes have vanished. Needless to say, particles are dummy objects. Yet in literature, the term "particles" is used to refer to both our particles and what we call spots. For the clarity of the upcoming discussion, however, we find the concept of spots useful.

In SVM, all variational parameters are optimized stochastically. The main arguments for random optimization go as follows:

- The simplest choice of non-linear parameters would be to use only a diagonal matrix $\boldsymbol{A}$, elements of which could be chosen deterministically, for example in a geometric progression [131]. The problem with such an approach is that the parameter grid for each diagonal element of $\boldsymbol{A}$ would need to be dense enough which would result in wavefunctions with many terms. Even then, using deterministic methods of parameter selection, it would be hard to avoid local minima in multi-dimensional parameter spaces. Moreover, not all of the parameter grid points would be equally important. The reason is that for a given set of Jacobi coordinates and orbital, spin, and isospin channels, a linear combination of correlated Gaussians forms a dense, non-orthogonal set. As a consequence, different sets of coefficients $\boldsymbol{A}$ (or α) represent the wavefunction equally well and none of them are really indispensable. This property of basis functions suggest the idea of a completely random selection of non-linear parameters.

- Furthermore, the nuclear interactions are strongly state dependent and for a realistic description of a nucleus, many different orbital, spin, and isospin channels need to be considered. The number of possible channels grows rapidly with the number of nucleons; but again, some channels will receive larger weights in the wavefunction than others.

- Also, in principle, all basis terms could be expressed in the same Jacobi set which would, as in three-body models, require inclusion of high partial waves to reach converged results. The convergence in orbital momentum is very slow in general, as we have seen for three-body results in Chapter 2, for example. Moreover, in practical many-body calculations, matrix element computation involving high partial waves is tedious and time consuming. On the other side, mixing different Jacobi sets in the wavefunction delivers faster convergence and only the low terms of the partial wave expansion are needed. This is because different Jacobi sets bring in different interparticle correlations and, as demonstrated by Eq. (2.27) for a three-body problem, low partial waves in one Jacobi set may contain higher partial waves in other Jacobi sets.

- As a result, even for fairly simple systems, such as ^{4}He bound by realistic nucleon-nucleon forces, the combined number of orbital, spin, and isospin channels, Jacobi sets, and non-linear parameters becomes prohibitively large. Therefore, the calculation of all of the matrix elements and diagonalization including all potentially important basis states of type Eq. (3.2) may be out of the question. In SVM, in addition to the random selection of the Gaussian non-linear parameters, a random selection of the orbital, spin, and isospin channels, as well as Jacobi sets is introduced. Random sampling also eliminates the danger of local minima traps in the multi-dimensional parameter space. The linear expansion parameters c in Eq. (3.9) are determined via energy matrix diagonalization, as explained before in this section.

Following these arguments, the wavefunction in Eq. (3.9) is constructed term by term in a trial-and-error method. Let us assume that the wavefunction already contains $N - 1$ basis states. Then the "construction" part of the optimization procedure reads:

1. Generate M random candidates to find the N^{th} basis function. Each new candidate is assembled in two steps:
   (a) Pick a Jacobi set and an orbital, spin, and isospin channel randomly from among all possible channels.
   (b) Randomly generate non-linear coefficients $\boldsymbol{A}$ (or α) from a "physically" relevant interval.
2. Through energy matrix diagonalization, calculate the energy with the N basis states formed out of the already adopted $N - 1$ states complemented with each of the M new candidates.
3. Among the random candidates, find the one providing the lowest energy in the previous step, add it to the wavefunction and increase the basis dimension to N. Discard all other random candidates.

The construction process is continued as long as some minimum amount of binding energy is gained with the acceptance of each new basis state. After that, the energy can be improved further without increasing the basis size by fine-tuning the non-linear coefficients. The "refinement" is done by applying steps 1(b)–3 to the already admitted basis states, i.e. by changing the non-linear parameters of one of the basis states already present in the wavefunction. The non-linear parameters of a single basis state are changed in the same way as before by randomly selecting the best combination. The refinement is done cyclically for each term in the wavefunction. Again, this fine-tuning is continued as long as binding energy is being gained. After that, more basis terms are added to the wavefunction through the construction algorithm. Several construction-refinement cycles may be needed before full convergence of the binding energy is reached.

We conclude this section by outlining a microscopic cluster version of SVM which was developed to account better for clustering in light nuclei and make the many-body calculations more tractable [132]. Over the years, the cluster version was applied to neutron-rich isotopes of elements with masses between six and eleven [75,77,133]. In this version, the nuclei are comprised of individual nucleons and microscopic clusters of ^{3}H, ^{3}He, and ^{4}He. The intrinsic wavefunctions of composite clusters are constructed from simple $1s$ harmonic-oscillator Slater determinants of a common width parameter. The inter-cluster wavefunction is modelled by correlated Gaussians and optimized by SVM. In such calculations, effective central nucleon-nucleon forces with occasional addition of spin-orbit and Coulomb interactions were used to bind the nuclei under study.

3.2 ^{4}He in the stochastic variational model

Having the framework of SVM outlined, we now wish to construct the wavefunction of ^{4}He within this model. In Chapter 5, such ^{4}He will serve as a core in ^{6}He. For ^{4}He bound by effective and realistic nucleon-nucleon forces, SVM results are in perfect agreement with other microscopic models. For effective nucleon-nucleon interactions, converged results can be obtained with less than a hundred correlated Gaussians [74]; for realistic forces with strong repulsion at short distances, several hundred basis states are needed to reach convergence [125].

3.2.1 Interactions

In microscopic calculations, the choice of the effective nucleon-nucleon interaction is of crucial importance. If one wants a model to have anything to do with the real physical problem, one must make sure that the inter-nucleon force is appropriate for all subsystems appearing in the model. As we have learned in Section 2.4, spin-singlet configurations of valence neutrons dominate the three-body wavefunction of ^{6}He, and as expected, these configurations have also been found to play a major role in this nucleus studied in microscopic models, e.g [134]. The spin-singlet state of two neutrons is unbound. Many effective nucleon-nucleon interactions do not take special care of this state, and in fact they often do not distinguish such state from a deuteron, which is a bound spin-triplet neutron-proton state. A popular potential of such kind is the Volkov force [135].

As the basis in the present work, the Minnesota nucleon-nucleon interaction [136] is used. This force reproduces the most important low energy nucleon-nucleon scattering data and therefore it does not bind the di-neutron. The force renormalizes effects of the tensor force into its central component and binds the deuteron by the right amount assuming a proton and a neutron in a relative s-wave. It also gives realistic results for the bulk properties of nuclei in the lowest s-shell. Furthermore, when supplemented by a spin-orbit force [137], the force reproduces low-energy α-nucleon scattering data. For two nucleons at positions (or spots) $\vec{r}_i$ and $\vec{r}_j$, the form of this interaction in Eq. (3.10) with the spin-orbit force included is:

$$\begin{aligned} V_{ij}(\vec{r}_{ij}) &= \left[V_1 + V_2\frac{1}{2}(1+P^{\sigma}_{ij}) + V_3\frac{1}{2}(1-P^{\sigma}_{ij})\right]\left[\frac{u}{2} + \frac{2-u}{2}P^{x}_{ij}\right] + \\ & \quad V_4\frac{1}{2\hbar}\vec{l}\cdot\left(\vec{\sigma}_i + \vec{\sigma}_j\right). \end{aligned} \tag{3.11}$$

Here, $\vec{r}_{ij} = \vec{r}_j - \vec{r}_i$. The exchange mixture parameter u has a default value 1.0 and can be tuned slightly to adjust the strength of the interaction. P^{σ}_{ij} is the spin-exchange operator exchanging spins at spots i and j. P^{x}_{ij} is the coordinate-exchange operator exchanging positions of spots i and j in the wavefunction. $\vec{\sigma}$ are the Pauli vectors of the nucleonic spin. $\vec{l}$ is the orbital momentum of the relative motion of two nucleons at spots i and j:

$$\vec{l} = -i\hbar(\vec{r}_j - \vec{r}_i) \times (\vec{\nabla}_j - \vec{\nabla}_i). \tag{3.12}$$

Finally, the potential has the following Gaussian form factors:

$$V_n = V_{0n} \exp\left(-\kappa_n r_{ij}^2\right), \qquad n = 1, \ldots, 4 \tag{3.13}$$

with numerical parameters:

n	V_{0n} [MeV]	κ_n [fm^{-2}]
1	200.00	1.487
2	−178.00	0.639
3	−91.85	0.465
4	−591.10	3.000

For the central components ($n = 1, 2, 3$), the potential parameters are from [136]. In that reference, it is advised to employ a short-range spin-orbit force to supplement the central interaction. Therefore, in the present work, the parameters of the spin-orbit force ($n = 4$) are those of the set IV in Table 1 from [137]. In [137], several sets of spin-orbit parameters are given, and among them the set adopted in this work is of the shortest range.

In Chapter 5, two cases of ^{6}He bound by different nucleon-nucleon interactions will be considered. In one of them, to be called MN (Minnesota), only the central component of the Minnesota force with the mixture parameter $u = 1.15$ will be used. In the other case, referred to as MN-SO (Minnesota with spin-orbit), the entire force from Eq. (3.11) with the mixture parameter $u = 1.015$ will be used. In both cases, the mixture parameters were adjusted to bind ^{6}He by approximately the right amount against the break-up into ^{4}He and two neutrons. More emphasis will be put to MN-SO results, and for that case the radial behavior of the central part of the Minnesota interaction for different spin-isospin nucleon doublets is shown in Figure 3.2. The exchange parameter does not affect the two dominant interaction channels: $S = 0$, $T = 1$ and $S = 1$, $T = 0$.

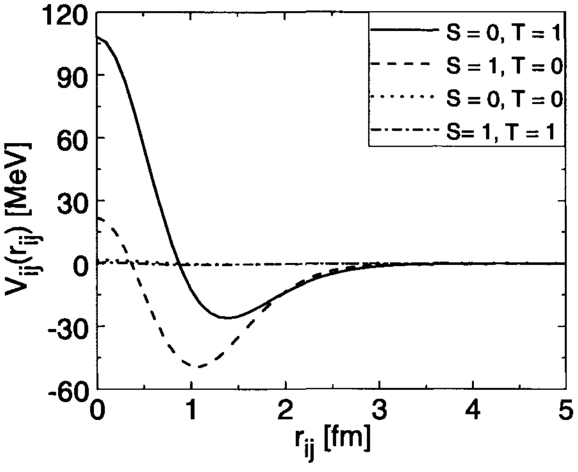

Figure 3.2: Radial dependence of the central part of the Minnesota potential from Eq. (3.11) with $u = 1.015$ in different spin-isospin channels of two nucleons coupled to total spin S and isospin T. Here, $r_{ij} = |\vec{r}_{ij}|$.

3.2.2 Results

For the two cases MN and MN-SO defined in the previous section wavefunctions of the ground state of ^{4}He were obtained within SVM. Both K- and H-like Jacobi sets from Figure 3.1 were mixed in the wavefunction. Due to the absence of non-central forces in the MN case, the wavefunction of ^{4}He contains only orbital channels with $L = 0$ and spin channels with $S = 0$. On the contrary, the spin-orbit force in MN-SO invites orbital and spin channels with $L \neq 0$ and $S \neq 0$ to the wavefunction. In both cases, all orbital channels with $l \leq 2$ were present in the model space.

Convergence of the binding energy of ^{4}He with the number of Gaussian basis states included in the wavefunction is shown in Figure 3.3. The convergence for MN-SO is slightly slower than for MN. Because the case MN-SO is more realistic due to the inclusion of the spin-orbit interaction, more effort was made to obtain a well converged wavefunction in that case. In converged states containing 20 and 75 basis states, ^{4}He is bound by -30.85 MeV and -30.93 MeV in MN and MN-SO, respectively. Therefore, ^{4}He turns out to be overbound relative to its experimental binding energy -28.30 MeV [118] which is not surprising given the effective nucleon-nucleon interactions employed.

In this chapter, the treatment of microscopic cores in two-neutron halo nuclei has

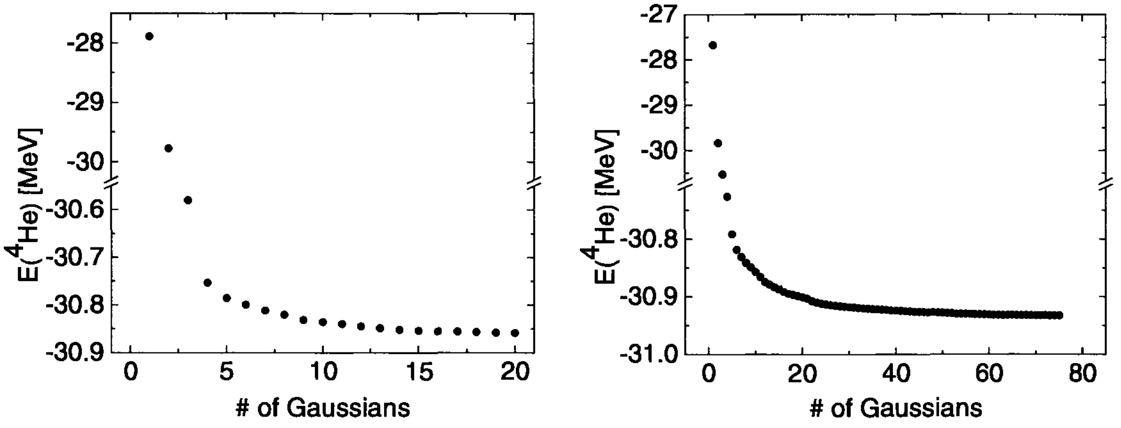

(a) MN (b) MN-SO

Figure 3.3: Convergence of the binding energy of the MN and MN-SO ^{4}He with the number of Gaussian basis states included in the wavefunction.

been presented. Having the MN and MN-SO wavefunctions for ^{4}He obtained within the SVM model, we now leave the discussion of microscopically described cores to be used in MiCH. Later in Chapter 5, ^{6}He built on MN and MN-SO ^{4}He cores will be studied in detail.

Chapter 4

MiCH: final assembly

Until now, we have separately introduced two building blocks of MiCH. To capture both the short- and long-distance correlations in two-neutron halo nuclei properly, we wish to combine the three-body-like approach from Chapter 2 to the valence part of the wavefunction with a microscopic core expressed within the SVM framework outlined in Chapter 3. We are now at the point where the two pieces, the core and the valence part, can finally be put together.

In this chapter, we first present the final form of the wavefunctions within MiCH. Driven by a desire for physical insight into extended Borromean halo systems, we are trying to build wavefunctions from functionally very different components for the core and the valence part. In doing so, we sacrifice computational ease, which has serious computational implications that need to be elaborated. Variational Monte Carlo is introduced as a suitable computational framework. Several methods aimed on improving numerical integrations are outlined. The chapter concludes with a discussion of variational optimization of wavefunctions in MICH.

4.1 Core and valence together

In essence, MiCH is a microscopic cluster model of two-neutron halo nuclei in which the clusters are a composite core and two valence neutrons. The form of the wavefunction in MiCH is based on the three-body-like decomposition in Eq. (2.21) with the following modifications:

1. The core is now a microscopic object described by a wavefunction $\Phi_{J^{\pi}_{core}\, T_{core}\, M_{T_{core}}}$ from Eq. (3.9).

2. Similarly to nucleons inside the core, the valence neutrons need to be treated carefully as particles in the manner described in Section 3.1. This is necessary because the valence nucleons are indistinguishable from those inside the core. If the core contains A_{core} nucleons, then the two extra neutrons are labelled as particles $p_{A_{core}+1}$ and $p_{A_{core}+2}$, and they are assigned isospins $\tau_{p_{A_{core}+1}}$ and $\tau_{p_{A_{core}+2}}$. Other than that, the valence particles are attached to the core as in the three-body model in Chapter 2. Accounting for isospins of valence particles, a definition of hyperharmonics in Eq. (2.19) is extended to:

$$\begin{aligned}\mathcal{Y}_{\gamma_{val}\, J^{\pi}_{val}\, 1-1} = {} & \varphi^{l_x\, l_y}_{K}(\theta) \times \\ & \left[\left[Y_{l_x}(\Omega_x) \otimes Y_{l_y}(\Omega_y) \right]_L \otimes \left[\chi_{p_{A_{core}+1}} \otimes \chi_{p_{A_{core}+2}} \right]_S \right]_{J^{\pi}_{val}} \times \\ & \left[\tau_{p_{A_{core}+1}} \otimes \tau_{p_{A_{core}+2}} \right]_{1-1}, \end{aligned} \tag{4.1}$$

which gives the valence term from Eq. (2.18) the following form:

$$\psi_{n_{lag}\, \gamma_{val}\, J^{\pi}_{val}\, 1-1} = \mathcal{R}_{n_{lag}}(\rho, \rho_0)\, \mathcal{Y}_{\gamma_{val}\, J^{\pi}_{val}\, 1-1}. \tag{4.2}$$

By convention, neutrons are particles with isospin projection -1/2. Therefore, the total isospin and isospin projection of the valence part of the wavefunction are 1 and -1, respectively.

3. The final modification of Eq. (2.21) is needed to antisymmetrize the wavefunction properly. The core itself comes already antisymmetrized. As it was argued in Chapter 3, it is advantageous to mix different Jacobi channels to accelerate the optimization of variational parameters. For the valence part, there exist Y and T

Jacobi configurations from Figure 2.1. All valence terms of the type of Eq. (4.2) are antisymmetrized in the T Jacobi basis by construction, but those in the Y basis are not. To ensure the proper antisymmetry between valence particles in a unified fashion, an additional antisymmetrization operator $\mathcal{A}^{val} = \sum_1^2 (-1)^p P$ is needed to act on all valence terms. In addition, the antisymmetry between valence nucleons and those inside the core is ensured by the action of yet another antisymmetrizer $\mathcal{A}^{core-val} = \sum_1^{A(A-1)/2} (-1)^p P$, where $A = A_{core} + 2$ is the mass number of the halo nucleus. In $\mathcal{A}^{val}$, operators P act only on valence particles, whereas in $\mathcal{A}^{core-val}$, operators P permute valence particles with those inside the core.

With these modifications to Eq. (2.21), the wavefunction for a two-neutron halo nucleus modelled in MiCH takes the form:

$$\begin{aligned}\Psi_{J^\pi M_J T M_T} = \sum \; & c^{\rho_0}_{J^\pi_{core}\, n_{lag}\, \gamma_{val}\, J^\pi_{val}} \mathcal{A}^{core-val} \\ & \left[\Phi_{J^\pi_{core}\, T_{core}\, M_{T_{core}}} \otimes \mathcal{A}^{val} \psi_{n_{lag}\, \gamma_{val}\, J^\pi_{val}\, 1 -1} \right]_{J^\pi M_J T M_T}\end{aligned} \tag{4.3}$$

For reasons explained later in this chapter, the sum is left without a summation index and compared to Eq. (2.21), the linear expansion coefficient c carries an additional index ρ_0 to account for the possibility of different values of ρ_0 in different valence terms. Also, it is implicitly assumed that parities π carry the same subscripts as their corresponding J.

More schematically, the wavefunction can be written as:

$$\Psi = \mathcal{A}^{core-val} \left[core \otimes val \right]. \tag{4.4}$$

This form is used to clarify further the meaning of terms "core" and "valence" first defined in Section 2.1. These terms keep their definite intuitive meanings only until $\mathcal{A}^{core-val}$ is executed; after that, the nucleons belonging originally to the core and to the valence part become indistinguishable. Therefore, the terms "core" and "valence" will refer to the situation before the antisymmetrizer $\mathcal{A}^{core-val}$ has acted.

Similarly to Chapter 3, the nuclear Hamiltonian includes the kinetic energies T_i of all nucleons and two-body nucleon-nucleon potentials V_{ij}:

$$H = \sum_{i=1}^{A} T_i + \sum_{1=i<j}^{A} V_{ij}. \tag{4.5}$$

The kinetic energy of the total center of mass does not need to be subtracted, because the wavefunction in Eq. (4.3) is expressed completely in the center-of-mass system.

In spite of fixed isospin projections of the core and the valence part, the total wavefunction in Eq. (4.3) has good isospin $T = |M_T|$ as long as the core is considered in its ground state only. In all potentially interesting two-neutron halo nuclei, cores have either the same number of protons and neutrons, and thus have isospin 0 (as in the case of ^{4}He), or are on the neutron-rich side of the chart of nuclei, thus having isospin $T_{core} = |M_{T_{core}}| = |(Z_{core} - N_{core})/2|$ where N_{core} and Z_{core} are the proton and neutron numbers of the core. Because only neutrons are added on top of an already neutron-rich core, the total isospin and its projection are simply equal to the sums of isospins of the core and the valence part. In the present work, the core is considered in its ground state only.

In Chapter 5, ^{6}He will be studied within MiCH. As we have argued in Section 2.4.1, this two-neutron halo nucleus is particularly simple to model, because both ^{4}He and ^{6}He have $J^\pi = 0^+$ ground states, leaving only valence channels with $J^+_{val} = 0$ open. Then, the angular momentum couplings in Eq. (4.3) can be simplified and the wavefunction takes a simple product form:

$$\begin{aligned} \Psi_{0^+01-1}\left({}^6\mathrm{He}\right) = \sum\; & c^{\rho 0}_{0^+ n_{lag}\gamma_{val}0^+}\mathcal{A}^{core-val} \\ & \left[\Phi_{0^+00}\left({}^4\mathrm{He}\right)\mathcal{A}^{val}\psi_{n_{lag}\gamma_{val}0^+1-1}(\rho_0)\right]. \end{aligned} \tag{4.6}$$

The form of the wavefunction in Eq. (4.3) can be encountered in other microscopic cluster models, too. Among such models applied to ^{6}He are SVM [76, 133] and the hyper-spherical model from [79]. There are several differences between MiCH and the other models. The most obvious is the treatment of the valence part. In MiCH, a functionally correct, exponentially decaying valence basis is adopted from three-body models, while the other microscopic cluster models employ Gaussians of some sort in the valence part of the wavefunction to reduce the computational demand. As we argued in Chapter 1, however, a Gaussian basis may not be the optimal choice to capture the asymptotic trends in Borromean nuclei. Another difference is the amount of details built into the core. In other microscopic cluster models applied to ^{6}He, the ^{4}He core is normally approximated by a single Slater determinant of single-particle harmonic oscillator wavefunctions. It was pointed out in [76, 134], however, that such a simplified treatment of the core may lead to underbinding of ^{6}He relative to the three-body break-up threshold. It was argued that other configurations such as 3N + N (here, N stands for a nucleon) should be present in the ^{4}He to account for a possible distortion of the core in ^{6}He. In MiCH, on the other hand, a converged ^{4}He from Section 3.2 is used as the core in ^{6}He, which should diminish the underbinding problem. Last, but not least, in Chapter 5 we will extract information about the ^{4}He + n + n decomposition of ^{6}He modelled within MiCH in the form suitable for feeding calculations of transfer reactions through which halo nuclei are commonly studied. This step has not been reported from other microscopic structure models.

In MiCH, the wavefunction in Eq. (4.3) is assembled in two steps. First, the core is constructed as a free nucleus. Once optimized, the core's variational parameters are excluded from optimizations in the second step of the wavefunction assembly. In other words, the distortion of the core due to valence neutrons is not considered explicitly, and like in many other microscopic models, a possible distortion of the core is accounted for only through the core-valence antisymmetrization. In the second stage of the wavefunction construction, the focus is on the valence part containing discrete $(n_{lag}, \gamma_{val}, J^{\pi}_{val})$, continuous non-linear (ρ_0), and continuous linear variational parameters (c). These valence parameters are to be varied until the expectation value of the Hamiltonian:

$$E = \frac{\langle\Psi|H|\Psi\rangle}{\langle\Psi|\Psi\rangle} \tag{4.7}$$

is minimized. Here, Ψ is the wavefunction from Eq. (4.3). To minimize the energy, we need a reliable and efficient method to compute integrals in Eq. (4.7).

Essentially the same integration/optimization problem from Eq. (4.7) was encountered in both the three-body model in Chapter 2 and SVM in Chapter 3. In the three-body model, the integrals involved in Eq. (4.7) are low-dimensional and can be easily evaluated. In the three-body model, it is then possible to have the same non-linear parameter ρ_0 in all valence terms and to simply enlarge the space of discrete variational parameters until energy convergence is reached. In SVM, the integrals are multidimensional, but because of the Gaussian basis, the integrals can be evaluated analytically in a closed form. Therefore, SVM can rely on a random trial-and-error selection of variational parameters.

In MiCH, the situation is different. The wavefunction in Eq. (4.3) combines a core with a functionally very different valence part. Upon the action of $\mathcal{A}^{core-val}$, the core and the valence part of the wavefunction are blended together and there does not seem to be an easy way to move between permuted Jacobi sets in order to find the set most appropriate for the computation of a given matrix element. To make calculations easier, one could consider expanding the valence hyper-spherical functions in Eq. (4.2) in terms of Gaussians and thus make the core and the valence part functionally identical. Then, all calculations could be carried out in the SVM fashion. However, such an expansion could compromise the long-distance behavior of the wavefunction, and so was abandoned. In MiCH, the only option seems to be a numerical evaluation of the matrix elements in Eq. (4.7). In the case of ^{6}He, the integrals involve $6 \times 3 = 18$ spatial and $2 \times 6 = 12$ spin-isospin dimensions.

Due to their numerical evaluation, matrix elements in Eq. (4.7) come with uncertainties. However, one must still be able to evaluate the integrals with sufficient accuracy to perform a meaningful variational calculation. The computational problem at hand is far from trivial, especially in the context of nuclear physics, where the interactions are highly state-dependent. Moreover, due to the dimensionality of the integration space, standard methods of on-grid integrations are out of the question. In conventional quadrature methods of numerical integration, the accuracy depends on the density of the integration mesh. For example, if one uses a d-dimensional cubic mesh to evaluate a d-dimensional integral using Simpson's rule, the error scales as $N^{-4/d}$, where N is the total number of mesh points [138]. Therefore, as the dimension d increases, the error falls off increasingly slowly with N. Therefore, a better way to evaluate multidimensional integrals is to scan the integration space to find the regions most relevant for a given physical problem. This opens the door to Monte Carlo integration techniques, in which the statistical error in the value of the integral falls off as $N^{-1/2}$ regardless of the integral's dimensionality. In particular, variational Monte Carlo has proven to be a very powerful tool to tackle mathematical problems of the type of Eq. (4.7).

4.2 Variational Monte Carlo

As stated in the previous section, we are dealing with a variational problem in which matrix elements must be evaluated by means of multi-dimensional numerical integrals. To simplify the notation in this section, we shall use $\Psi(\vec{r}, s, t, p)$ for the wavefunction in Eq. (4.3) depending on all spatial ($\vec{r} = \{\vec{r}_1, \dots, \vec{r}_A\}$), spin ($s = \{\chi_1, \dots, \chi_A\}$) and isospin ($t = \{\tau_1, \dots, \tau_A\}$) degrees of freedom as well as on a set of variational parameters (p). The expectation value of the Hamiltonian H with the wavefunction gives an estimate of the ground-state energy:

$$\langle H(p) \rangle = E(p) = \frac{\langle \Psi(\vec{r}, s, t, p) | H | \Psi(\vec{r}, s, t, p) \rangle}{\langle \Psi(\vec{r}, s, t, p) | \Psi(\vec{r}, s, t, p) \rangle}. \tag{4.8}$$

On the left-hand side, the braces denote expectation (mean) value of the operator, on the right-hand side, they mean integration over all $\vec{r}$, s and t. By minimizing $E(p)$ with respect to all variational parameters, one obtains the approximation to both the energy and the wavefunction of the true nuclear ground state. Integrals involved in Eq. (4.8) are to be computed by means of variational Monte Carlo (VMC).

Mathematical foundations of various Monte Carlo techniques can be found for example in [139]. VMC has been applied to problems in nuclear [66, 140] as well as other areas of physics [138]. For a general description of VMC, we shall lean mostly on [138–140] supplemented by other references. The term "variational Monte Carlo" comprises two aspects of the problem in Eq. (4.8). The "variational" part refers to the variational nature of the problem, whereas the "Monte Carlo" part is responsible for the actual evaluation of the integrals involved. The general concept of VMC, however, does not provide any guidance on moving within the space of variational parameters that would help us move towards the variational energy minimum.

In the following text, we first focus on numerical aspects of Eq. (4.8). The Metropolis algorithm along with other techniques used to evaluate integrals will be described. Then, VMC will be applied to a simplified case of ^{6}He to convince ourselves that the integrations are done properly in MiCH. The section on VMC will conclude with the discussion of parameter optimization techniques used in MiCH.

4.2.1 Monte Carlo essentials

The Monte Carlo approach to the evaluation of multi-dimensional integrals relies on statistical sampling and averaging of the integrand. In this section, the essentials of the Monte Carlo integration are presented.

Adhering to the physical problem at hand, let us consider many-body functions depending only on A spatial coordinates concisely denoted as $\vec{r} = \{\vec{r}_1, \dots, \vec{r}_A\}$; complications due to spins and isospins will be discussed later. The goal is to find the integral of some function $f(\vec{r})$:

$$I \equiv \int f(\vec{r})\, \mathrm{d}\vec{r}, \tag{4.9}$$

where the integral is taken over the relevant space of $\vec{r}$. An underlying idea of Monte Carlo integration lies in transforming the integrand into a product of two auxiliary functions $p(\vec{r})$ and $g(\vec{r})$. The former function, also called the importance or sampling function, is chosen first such that it obeys:

$$p(\vec{r}) \geq 0, \qquad \int p(\vec{r})\,\mathrm{d}\vec{r} = 1, \tag{4.10}$$

and hence may be ascribed a meaning of a probability density. Consequently, the vector $\vec{r}$ may be considered a random variable. The other function $g(\vec{r})$ is computed accordingly as $g = f/p$. Then, the original integral can be written as:

$$I = \int g(\vec{r})\,p(\vec{r})\,\mathrm{d}\vec{r} \tag{4.11}$$

and interpreted as nothing more than the mean or expectation value of the function $g(\vec{r})$. Due to its dependence on the random vector $\vec{r}$, the function $g(\vec{r})$ is a random variable distributed around its mean value I with variance:

$$\mathrm{var}(g) \equiv \int [g(\vec{r}) - I]^2\,p(\vec{r})\,\mathrm{d}\vec{r}. \tag{4.12}$$

In principle, the value of I may be obtained by drawing an infinite set of mutually independent random vectors from the distribution $p(\vec{r})$ and computing the sample average of local values $g(\vec{r})$:

$$I = \lim_{N\to\infty}\left[\frac{1}{N}\sum_{n=1}^{N} g\left(\vec{r}^{(n)}\right)\right]. \tag{4.13}$$

Here, $\vec{r}^{(n)}$ means the n-th set of vectors $\vec{r}$. A Monte Carlo estimate of I may be obtained by averaging over a finite sample:

$$I \approx I_N = \frac{1}{N}\sum_{n=1}^{N} g(\vec{r}^{(n)}). \tag{4.14}$$

The variance of function $g(\vec{r})$ from Eq. (4.12) can be estimated in an unbiassed way as:

$$\mathrm{var}(g) \approx \sigma_{N-1}^2(g) \equiv \frac{N}{N-1}\sigma_N^2(g), \tag{4.15}$$

where $\sigma_N^2(g)$ is a commonly computed biassed estimator of the variance of values $g(\vec{r}^{(n)})$ distributed around their mean value I_N:

$$\sigma_N^2(g) \equiv \frac{1}{N}\sum_{n=1}^{N}\left[g(\vec{r}^{(n)}) - I_N\right]^2. \tag{4.16}$$

The quantity $\sigma_{N-1}(g)$ is called the unbiassed standard deviation of the sample $g(\vec{r}^{(n)})$.

In the nomenclature of quantum Monte Carlo, the vector $\vec{r}$ is said to be a walker, wandering around the integration space. A random stop, $\vec{r}^{(n)}$, of the walker is called a configuration or a sampling point, and a chain of sampling points is referred to as a random walk. In the present work, we prefer to use the term integration point over sampling point. Referring back to Chapter 3, an integration point $\vec{r}^{(n)}$ consists of a set of spots $\vec{r}_1^{(n)}, \dots, \vec{r}_A^{(n)}$.

It is important to realize that different random walks may yield different values of I_N. In fact, for any N, the Monte Carlo estimator I_N by itself is a random variable distributed with its own probability density, the expectation value of which is equal to I, and the variance of which is:

$$\mathrm{var}(I_N) = \frac{\mathrm{var}(g)}{N}. \tag{4.17}$$

Using the Monte Carlo estimator from Eq. (4.15) for var(g), the variance of integral estimates I_N can be estimated as:

$$\mathrm{var}(I_N) \approx \frac{\sigma_{N-1}^2(g)}{N}. \tag{4.18}$$

We point out that, when the original integral Eq. (4.9) is estimated by Eq. (4.14) on short random walks, the distribution of values of I_N may not be Gaussian and so $\sqrt{\mathrm{var}(I_N)}$

can not be attributed the typical meaning of an error bar. As $N \to \infty$, however, the central limit theorem shows that the distribution of values I_N will converge toward a normal distribution regardless of the sampling distribution $p(\vec{r})$ or the distribution of local values $g(\vec{r}^{(n)})$. Only then is it meaningful to estimate a one-standard-deviation error of the Monte Carlo estimate of the mean (also called the standard error of the mean or simply the error):

$$S_e(I_N) = \frac{\sigma_{N-1}(g)}{\sqrt{N}}, \qquad \text{when } N \to \infty. \tag{4.19}$$

Therefore, the error bar on the integral estimate I_N will decrease as $1/\sqrt{N}$ regardless of the integral dimensionality in Eq. (4.9). We emphasize again that the Monte Carlo estimate of the integral I_N and the error S_e are trustworthy only when they are estimated on large samples of statistically independent integration points $\vec{r}^{(n)}$.

A judicious choice of the importance function significantly reduces the variance for a fixed sample size. The variance of the integral estimate $\mathrm{var}(I_N)$ in Eq. (4.17) would vanish for a constant function $g(\vec{r}) = const = I$. However, this choice is not available since the integral I is not known a priori. In practice, we want an importance function that matches the general behavior of the function $g(\vec{r})$. In many quantum-mechanical problems, the importance function is taken to be the square of the actual wavefunction.

Once the importance function is chosen, the integral in Eq. (4.9) can be estimated by means of Eq. (4.14). We rely upon the Metropolis algorithm [141] for generating a random walk with integration points distributed according to the sampling function $p(\vec{r})$. Considered a golden standard for integration space sampling, this algorithm has been employed in nearly all other variational Monte Carlo calculations. The description of the Metropolis algorithm with all non-trivial details can be found for example in [139]. For our purposes, we use the following simple version of the algorithm encountered in most practical applications:

1. Given a walker at point $\vec{r}$, generate a trial vector $\vec{r}_{trial}$ randomly from within a $3A$-dimensional cube of volume $(\Delta_r)^{3A}$ surrounding the point $\vec{r}$.

2. Calculate the probabilities $p(\vec{r})$ and $p(\vec{r}_{trial})$. The acceptance probability for a move from $\vec{r}$ to $\vec{r}_{trial}$ is given by the expression:

   $$P(\vec{r} \to \vec{r}_{trial}) = \min\left\{1, \frac{p(\vec{r}_{trial})}{p(\vec{r})}\right\}.$$

   In actual calculations, the ratio in brackets is compared with a random number between 0 and 1; if the ratio is greater, the proposed move is accepted.

3. If the move is accepted, set $\vec{r} = \vec{r}_{trial}$ and return to step 1. Otherwise, discard the point $\vec{r}_{trial}$ and generate the next trial move from the original position $\vec{r}$.

The very first sampling point is chosen completely randomly. By construction, the algorithm satisfies the condition of detailed balance. This condition ensures that if many walkers originating from different positions are launched simultaneously, at any time later the number of walkers flowing from one integration point to another is the same as the number of walkers flowing in the opposite direction. Therefore, any point in the integration space can be reached by the walker from any other point.

Despite its simplicity, the Metropolis algorithm is of a great power, as it can be used to sample essentially any importance function regardless of the number of dimensions. Another advantage is that to generate a walk the importance function does not need to be normalized because the acceptance probability $P(\vec{r} \to \vec{r}_{trial})$ depends only on a ratio of local values of the importance function. There are, however, a few complementary disadvantages of the algorithm. First, the sampling is correct only asymptotically. The initial integration points generated depend on the starting point and should be discarded. In all our calculations, at least 1,000 generated integration points are discarded before local values of the operators are first evaluated. Second, successive integration points are correlated, which violates the assumption of their statistical independence needed to make the Monte Carlo estimates reliable. This correlation is obvious because the new point $\vec{r}$ in step 3 is either equal to $\vec{r}$ from step 1, or is somewhere nearby. Consequently, successive local values of the function $g(\vec{r})$ are likely to be correlated. Due to such correlations, the effective number of independent samples is less than the actual number of points in the random walk, which slows down the convergence of the integral estimate in Eq. (4.14) and also makes the formulae in Eq. (4.15) and Eq. (4.19) underestimate true statistical deviations. Therefore, great care must be taken to ensure that the integral is estimated on a sufficiently large set of statistically independent configurations $\vec{r}^{(n)}$, as will be discussed in Section 4.2.2.

Having outlined the Monte Carlo integration, we now turn back to the evaluation of expectation values of physical observables depending on the many-body wavefunctions $\Psi = \Psi(\vec{r}, s, t)$:

$$\langle O \rangle = \frac{\langle \Psi | O | \Psi \rangle}{\langle \Psi | \Psi \rangle} = \frac{\displaystyle\int \langle \Psi | O | \Psi \rangle_{s,t} \, \mathrm{d}\vec{r}}{\displaystyle\int \langle \Psi | \Psi \rangle_{s,t} \, \mathrm{d}\vec{r}}, \tag{4.20}$$

where O is an operator and $\langle | \rangle_{s,t}$ denotes the inner product in the spin-isospin space. In quantum mechanics, the square of the normalized wavefunction is a good candidate for the sampling function:

$$p(\vec{r}) = \frac{\langle \Psi | \Psi \rangle_{s,t}}{\langle \Psi | \Psi \rangle}. \tag{4.21}$$

With this choice of the importance function and the following definition of a local value of the operator O:

$$O_{loc}(\vec{r}) \equiv \frac{\langle \Psi | \, O \, | \Psi \rangle_{s,t}}{\langle \Psi | \Psi \rangle_{s,t}}, \tag{4.22}$$

Eq. (4.20) takes a very simple form:

$$\langle O \rangle = \int O_{loc}(\vec{r}) \, p(\vec{r}) \, \mathrm{d}\vec{r} \tag{4.23}$$

suitable for the Monte Carlo evaluation. At each integration point, a local value in Eq. (4.22) is calculated and the expectation value $\langle O \rangle$ and its error are estimated by means of Eq. (4.14) and Eq. (4.19). Local values of total energy will be denoted as E_{loc}.

In practical calculations, the norm $\langle \Psi | \Psi \rangle$ of the wavefunction is often not known and in fact is not needed. It is because the norm appears in Eq. (4.20) that we can adapt the Monte Carlo machinery to the computation of $\langle O \rangle$ and never actually compute the norm of the wavefunction. Formally, the importance function in Eq. (4.21) is normalized to unity to make Eq. (4.23) work; however, as we explained before, the Metropolis algorithm does not care about whether the importance function is normalized or not. Therefore, to generate a random walk needed to evaluate Eq. (4.23), $p(\vec{r}) = \langle\Psi|\Psi\rangle_{s,t}$ can be used.

In a more general case, any importance function having sufficient overlap with the square of the actual wavefunction can be used to sample the physical space. One then talks about correlated sampling, in which the expectation value of an operator is computed as:

$$\langle O\rangle = \frac{\displaystyle\int \frac{\langle\Psi|O|\Psi\rangle_{s,t}}{p(\vec{r})} p(\vec{r})\,\mathrm{d}\vec{r}}{\displaystyle\int \frac{\langle\Psi|\Psi\rangle_{s,t}}{p(\vec{r})} p(\vec{r})\,\mathrm{d}\vec{r}} = \frac{\displaystyle\int O_{loc}(\vec{r})\, w(\vec{r})\, p(\vec{r})\,\mathrm{d}\vec{r}}{\displaystyle\int w(\vec{r})\, p(\vec{r})\,\mathrm{d}\vec{r}}, \tag{4.24}$$

where $w(\vec{r})$ is a local weight defined as:

$$w(\vec{r}) \equiv \frac{\langle\Psi|\Psi\rangle_{s,t}}{p(\vec{r})}. \tag{4.25}$$

Both integrals on the right-hand side of Eq. (4.24) are approximated by finite sums of the type in Eq. (4.14). As far as the expectation values of operators are concerned, the sampling function in correlation sampling does not need to be normalized because its overall normalization would enter both integrals in Eq. (4.24) and so would be cancelled out.

The material contained in this section is sufficient to evaluate multi-dimensional integrals encountered in the variational problem in Eq. (4.7). Further discussion on technical details and the implementation of VMC can be found in Appendix A. Before we proceed further towards techniques used to optimize variational parameters, we have to make sure that the integral estimates are reliable. As mentioned before, the Metropolis algorithm has several drawbacks that need to be thoroughly examined.

4.2.2 Can we trust ourselves?

In this section, we examine the inner workings of the numerical Monte Carlo integrations presented in the previous section. In particular, we look at correlations between local values inherent in the Metropolis algorithm. We discuss several methods to attenuate the degree of such undesired correlations.

As a test case, a simple ^{6}He is considered bound by the central part of the Minnesota interaction from Eq. (3.11) with the mixture parameter set to its standard value $u = 1.0$. This interaction is similar to MN from Section 3.2. To optimize the wavefunction of the ^{4}He core, both K- and H-like Jacobi channels and all orbital channels with $l \leq 2$ and $L = 0$ are present in the model space. Variationally optimized ^{4}He core contains 20 Gaussian basis terms and its binding energy is -30.77 MeV. To assemble the ^{6}He guinea pig, a single valence term in the T Jacobi basis with $K = 2$, $l_x = l_y = L = S = 0$ and $n_{lag} = 0$ is attached to the core as in Eq. (4.6). The non-linear parameter in the valence part is set to $\rho_0 = 1.0$ fm to reproduce approximately the experimentally known size of ^{6}He. The choice of the valence channel is given by its major role in the three-body wavefunction of ^{6}He in Section 2.4.3. Therefore, in spite of its simplicity, this ^{6}He is expected to provide a reliable testing ground. Unless noted otherwise, this ^{6}He is used in all calculations in the rest of the current section.

As mentioned in Section 4.2.1, successive integration points generated by the Metropolis algorithm may be correlated, often very strongly. Let us consider a random walk containing N integration points. At each point, a local value of some function $g(\vec{r})$ is evaluated. To assess quantitatively the degree of correlation between local values $g(\vec{r}^{(n)})$ k integration points apart, we use a biassed estimator of auto-correlation coefficient:

$$r(g,k) = \frac{1}{(N-k)\,\sigma_N^2(g)} \sum_{n=1}^{N-k} \left[g(\vec{r}^{(n)}) - I_N\right] \left[g(\vec{r}^{(n+k)}) - I_N\right] \tag{4.26}$$

with the notation preserved from Section 4.2.1. By definition, $r(g,0) = 1$, and for $N = 2$, $r(g,1) = -1$. The auto-correlation coefficient takes positive values for highly correlated local values $g(\vec{r}^{(n)})$ and vanishes for uncorrelated samples. The distance k will be called the correlation distance.

In this section, the focus is on correlations between local values of total (kinetic plus potential) energy, because in light of the variational principle in Eq. (4.8), the total energy is of primary interest. Hereafter, by energy we mean the total energy, and a local value of the total energy is shortened to a local energy, unless stated otherwise. In the Metropolis algorithm, the degree of correlation can be controlled by the linear size Δ_r of the 3A-dimensional cube from which trial moves are drawn. To illustrate the effect of Δ_r, three random walks were produced with values of $\Delta_r = 4.5$ fm, 1.4 fm and 0.15 fm, corresponding to Metropolis acceptance probabilities (or rates) of about 5%, 50% and 95%, respectively. Each walk contains 10,000 integration points and the sampling function was taken as the square of the wavefunction of ^{6}He. For each walk, auto-correlation coefficients were computed and are shown in Figure 4.1 along with fragments of Monte Carlo histories of local energies.

It is evident from Figure 4.1 that local energies are tightly correlated, especially for extrema of Metropolis acceptance rates. The explanation in terms of Δ_r is simple. Imagine a walker at some point $\vec{r}$ in space with a presumably large probability $p(\vec{r})$, Then a trial move drawn from a cube with large Δ_r may easily end up in a region with much lower probability, and so be rejected, which gives raise to flat sections in Monte Carlo histories. On the other hand, when Δ_r is small, a trial move does not disturb the probability $p(\vec{r})$ too much and will most likely be accepted, which results in fairly smooth Monte Carlo histories. These arguments are also reflected by the very slow decay of auto-correlation curves in Figure 4.1. On the other hand, the case with moderate Metropolis acceptance produces fairly weakly correlated local energies. Based on this observation, we shall hereafter adhere to the lore of quantum Monte Carlo holding that the Metropolis algorithm should accept about fifty percent of trial moves in order to produce good results.

Even when the Metropolis acceptance rate is close to 50%, local energies are still correlated, but the degree of correlation is quickly attenuated as the correlation distance increases. This observation suggests an improved sampling algorithm in which every

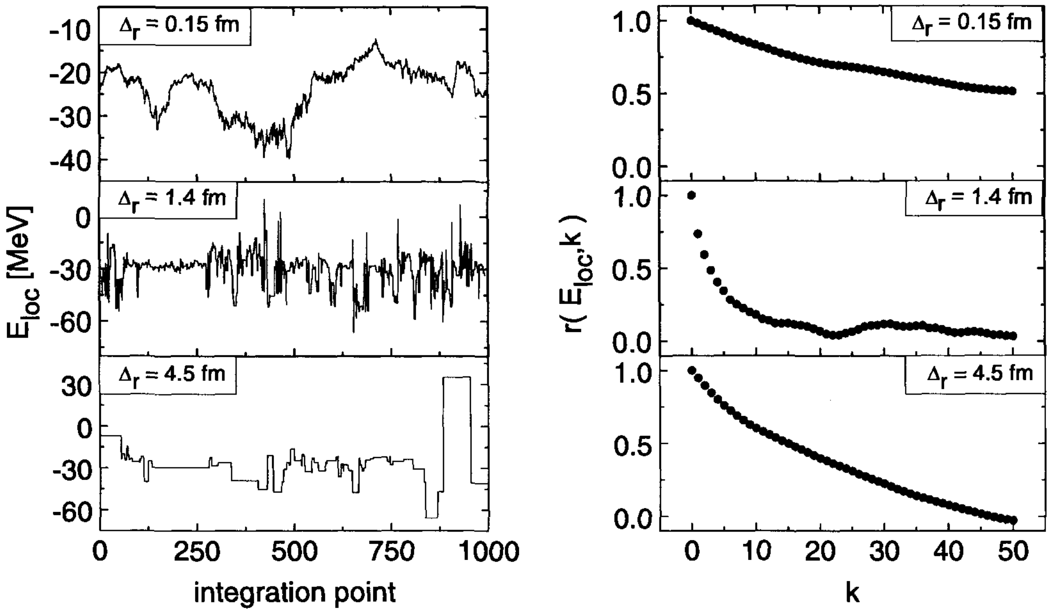

(a) Monte Carlo histories of the first 1,000 local energies.

(b) Auto-correlation coefficients between local energies computed from all 10,000 integration points in each random walk for different correlation distances k.

Figure 4.1: Effects of correlations in the Metropolis algorithm on local energies. The results are for three random walks with $\Delta_r = 4.5$ fm, 1.4 fm, and 0.15 fm corresponding to Metropolis acceptance rates of about 5%, 50% and 95%, respectively.

integration point is decorrelated a certain number of times before local values of operators are evaluated again, as is schematically illustrated in Figure 4.2. The auto-correlation curve in Figure 4.1(b) with $\Delta_r = 1.4$ fm suggests that about 5–10 decorrelation steps should suffice to substantially decorrelate local energies. In Figure 4.3 we show auto-correlation curves for local energies produced in three new independent walks with 1, 10, and 30 decorrelation steps. From this figure it is also clear that having about 10 decorrelation steps is indeed good enough to break correlations between local energies. Using more decorrelation steps hardly improves the results.

An alternative approach to decorrelated sampling is the data reblocking (or bunching) method [142]. The method works as follows. At reblocking level 0, a set of local values $\{g(\vec{r}^{(n)}), n = 1, \ldots, N\}$ is considered a set of $N^{(0)} \equiv N$ blocks, each block holding a single local value and thus having a block average value of $\bar{g}_n^{(0)} \equiv g(\vec{r}^{(n)})$. Then, for any higher reblocking level b, new blocks are formed by merging the two neighboring blocks

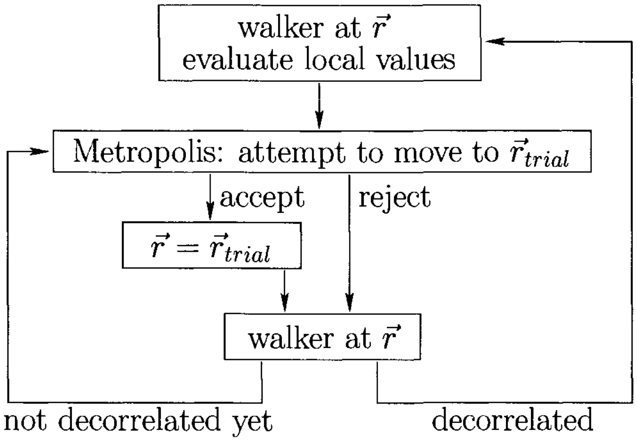

Figure 4.2: Flow chart for the decorrelated Metropolis algorithm.

from the previous level. Therefore, the new block averages are equal to:

$$\bar{g}_{n'}^{(b)} = \frac{1}{2}\left[\bar{g}_{2n'-1}^{(b-1)} + \bar{g}_{2n'}^{(b-1)}\right] \qquad b = 1, 2, \ldots \tag{4.27}$$

with $n' = 1, \ldots, N^{(b)}$, where $N^{(b)} = \mathrm{int}(N^{(b-1)}/2)$. Here, the operation int means truncation to the nearest integer. The reblocking continues as long as at least two new blocks can be formed. At each level, the sample mean value and its error $S_e^{(b)}$ are computed by applying Eq. (4.14) and Eq. (4.19) to the block averages $\bar{g}_{n'}^{(b)}$. One can even estimate the

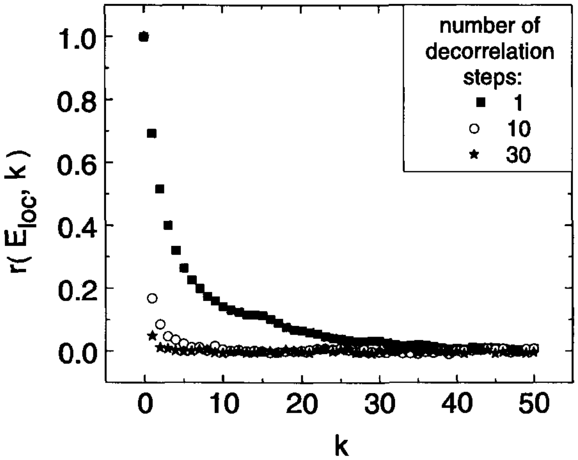

Figure 4.3: Auto-correlation coefficients between local energies as a function of the correlation distance k in three independent walks with 1, 10, and 30 decorrelation steps. Each walk contains 2^{16} integration points and the Metropolis acceptance rate is about 50%.

error on the standard error $S_e^{(b)}$ as $S_e^{(b)}/\sqrt{2(N^{(b)}-1)}$ [142].

The idea behind the reblocking algorithm is the following. As the reblocking level increases, each new block contains more and more original local values and so, on the basis of the central limit theorem, block averages approach independent Gaussian stochastic variables. When the sample size N is a power of two[1], the sample mean is invariant under the blocking transformation. Furthermore, for statistically independent block averages, the standard error $S_e^{(b)}$ is also blocking-invariant. For correlated data, blocking typically yields increasingly uncertain estimates of $S_e^{(b)}$ and the best error estimate is obtained for the smallest blocking level beyond which $S_e^{(b)}$ saturates. At very high reblocking levels, the error estimate may become unreliable because of the small number of remaining blocks.

To see the effect of reblocking, in Figure 4.4 the bunching algorithm is applied to the data from Figure 4.3. In general, energy block averages become less correlated as the level of reblocking increases. However, for the walk with a single decorrelation step the reduction of correlations is still fairly slow, the error estimate $S_e^{(b)}$ barely saturates, and the error estimated directly from the local energies (reblocking level 0) severely underestimates the true error. In agreement with previous observations, about ten decorrelation steps are needed for the error estimate of the mean energy to quickly form a distinct plateau, the appearance of which is a fully convincing signal that energy block averages have become statistically uncorrelated and saturated error estimates can be trusted. Note that for well decorrelated walks saturated error estimates are almost identical to those for no reblocking. In most of our calculations, blocks are formed from 100 local values which corresponds to reblocking levels 6–7.

For the walk with 30 decorrelation steps from Figure 4.3, the evolution of the mean energy and the energy error estimate is plotted in Figure 4.5. At the beginning of the walk, the running mean energy is poorly defined due to low statistics. Later into the walk, the energy curve flattens and the statistical error in the energy is reduced. Even

---

[1] Otherwise, at some reblocking levels, single excess blocks are dropped in order for Eq. (4.27) to work, which results in a data loss.

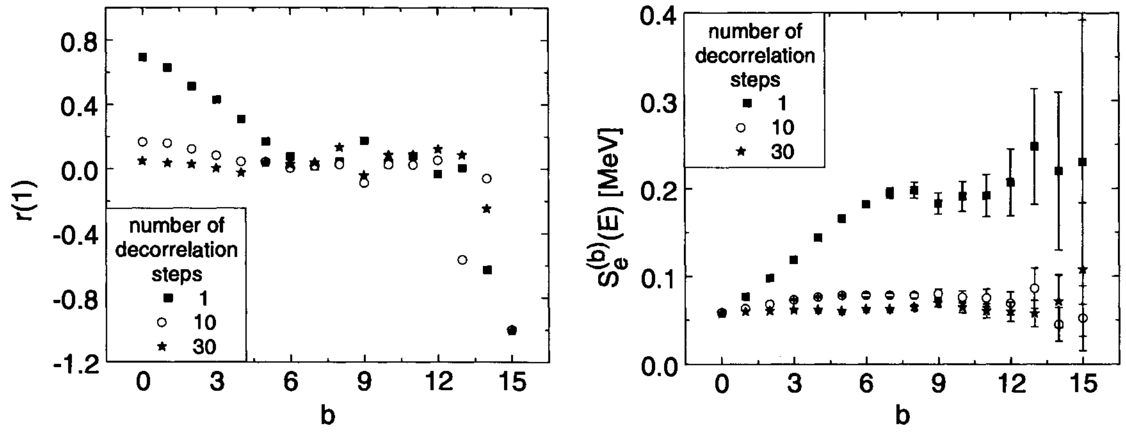

(a) Auto-correlation coefficients between successive energy blocks ($k = 1$).

(b) Estimates of the standard error of the mean energy.

Figure 4.4: Effects of bunching on data from Figure 4.3 at different reblocking levels b.

though not visible in the figure, the error falls off as $N^{-1/2}$ towards the end of the walk where a sufficient number of integration points has been averaged.

For an additional insight into the effects of correlations, Figure 4.6 shows block averages and unbiassed standard deviations of local values within blocks of kinetic, potential and total energies for data from Figure 4.3. First, we notice large cancellations between kinetic and potential energy resulting in a fairly narrow interval of block averages of total

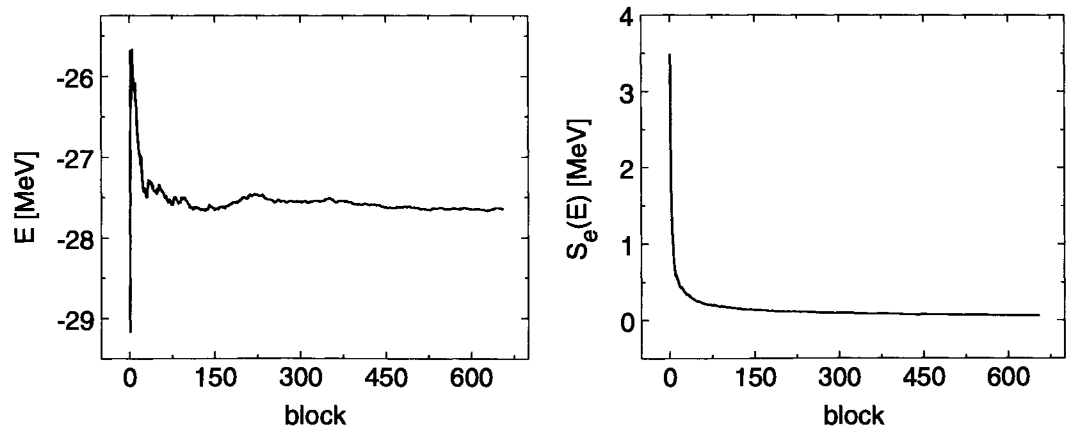

(a) Mean energy computed by applying Eq. (4.14) to block averages.

(b) Energy error estimate computed by applying Eq. (4.19) to block averages.

Figure 4.5: Mean energy and energy error estimate computed along the walk with 30 decorrelation steps from Figure 4.3. Local energies are divided into blocks of 100 values.

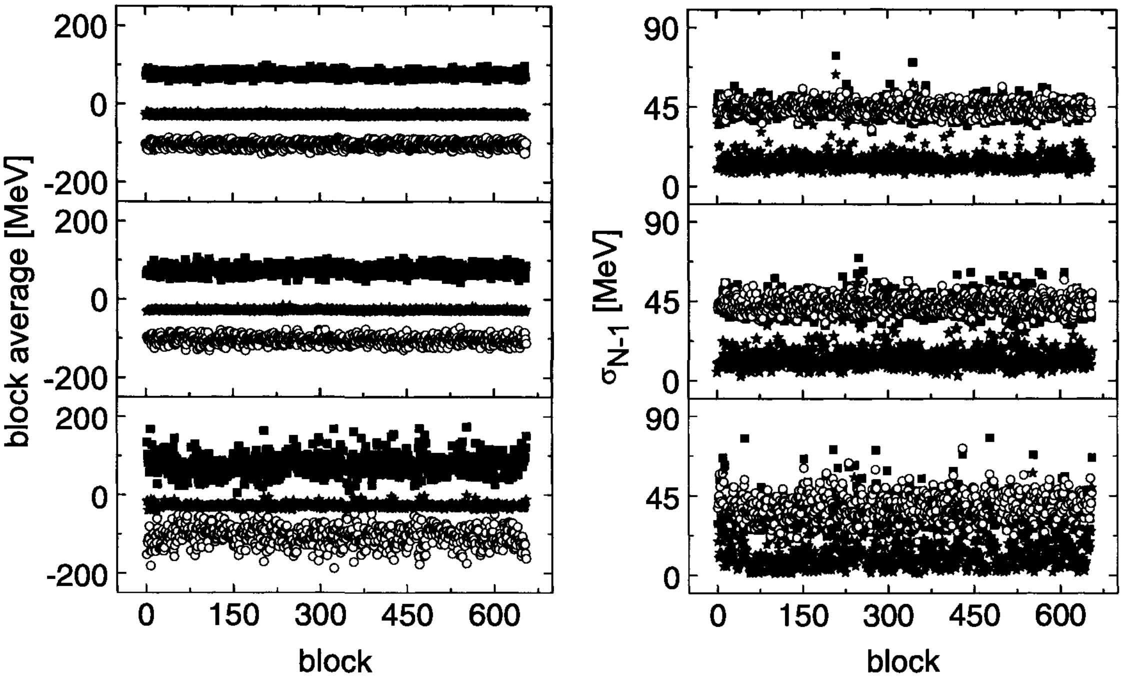

(a) Block averages.

(b) Standard deviations within blocks.

Figure 4.6: Block values of kinetic (solid black squares), potential (empty red circles), and total (solid blue stars) energy for data from Figure 4.3. Each block contains 100 local values. Panels from bottom to top correspond to walks with 1, 10, and 30 decorrelation steps.

energy. The undesired spread of block averages and deviations within blocks is reduced as the number of decorrelation steps increases, which can be explained as follows. Correlated local values tend to follow one another more closely (see cases with $\Delta_r = 4.5$ fm and 0.15 fm in Figure 4.1(a)) such that there will be entire blocks of them with a fairly small internal spread, but which lie on average quite far from the walk average. On the contrary, well decorrelated local values are more evenly distributed on both sides of the walk average, the consequences of which are a more efficient averaging within blocks resulting in a narrower distribution of block averages and larger deviations within blocks. Again, taking more than ten decorrelation steps hardly improves the results.

In summary it is obvious that the Metropolis algorithm used to generate random walks may easily provide biassed results. In this section, the focus was on the energy as the observable crucial for variational optimization, but the observations made are valid for other observables as well. Based on the arguments presented, in this work we adhere to the following rules:

- The Metropolis acceptance rate should be close to 50% of proposed trial moves.
- Each walk is decorrelated by a sufficient number of decorrelation steps. In most calculations, we use 30 or more decorrelation steps.
- The reblocking algorithm is used to reliably estimate the error in the energy.
- For increased accuracy, results computed on several independent random walks may be averaged.

Appendix B contains additional reliability tests.

4.2.3 Wavefunction optimization

Having introduced the Monte Carlo background needed for evaluation of integrals in Eq. (4.7), we now turn to the actual problem of wavefunction optimization. The goal is to optimize variational parameters in the valence part of the wavefunction in Eq. (4.3). In this section, these variational parameters are called simply parameters. VMC, as presented so far in Section 4.2, provides a general framework to compute expectation values of energy for a given set of parameters, but the method must be accompanied by additional tools to give any sort of guidance in the parameter space.

From a physics standpoint, the parameter optimization is achieved via minimization of energy in Eq. (4.7). From a practical standpoint, the variational problem is more complicated due to the statistical evaluation of matrix elements required. Local energies fluctuate around the estimated mean energy and, as we have seen in Figure 4.5, along the course of a random walk the running mean energy may drop below its converged value. For a given set of parameters, it is a matter of luck whether the energy estimate is below or above the true energy, which is not known anyway. Therefore, energy estimates may be misleading, especially when one compares energies for different sets of parameters. It has been argued [143, 144] that a numerically more stable parameter optimization can be achieved by minimizing the variance, Eq. (4.16), of local energies, or by minimizing a linear combination of the energy and the variance of the energy [144]. The major argument for variance minimization is that at the minimum the variance is known to be zero a priori. Moreover, each term in the sum Eq. (4.16) is bounded from below by zero. The major drawback of variance minimization is that, from the physical point of view, one typically seeks the lowest energy, which is not guaranteed to be delivered by variance minimization unless the true eigenstate is found. Furthermore, it has been observed [145] that energy optimized wavefunctions give on average better expectation values for other observables. Sometimes, the energy and variance minimizations are used to optimize different parts of the wavefunction [146]. In the present work, the expectation value of energy is minimized. As the energy is minimized, the variance of local energies is reduced as well.

Regardless of the actual optimization procedure, one needs to ensure that the energy is really being lowered. Correlated sampling introduced in Section 4.2.1 is a useful trick commonly employed to roughly disentangle the effect of a small change in the parameters on energy from ambiguities arising due to the statistical sampling. One begins with a wavefunction Ψ_{ref} containing reference values of parameters. For this wavefunction, a reference random walk $\{\vec{r}^{(n)}, n = 1, \ldots, N\}$ is generated and energy E_{ref} is estimated from Eq. (4.23). Suppose (some of) the parameters in Ψ_{ref} are slightly[2] disturbed resulting in a new wavefunction Ψ. Then, instead of generating a new walk for Ψ, we can use the reference walk to estimate the energy E corresponding to Ψ. Because both energies E and E_{ref} are computed on the same walk, statistical ambiguities potentially arising from different walks are suppressed. One normally looks at the difference between the two energies because they are highly correlated, and the error of the difference is much smaller than errors on the two energies themselves. Using Eq. (4.24) with $p(\vec{r}) = \langle \Psi_{ref} | \Psi_{ref} \rangle_{s,t}$[3]

---

[2] The term "slightly" needs to be defined with care. It includes not only a slight change of continuous parameters, but also a change of discrete parameters due to a change, addition and/or removal of valence channels. A quantitative measure of "slightness" will be provided later in terms of local weights.

[3] The importance function for correlated sampling does not need to be normalized, as discussed in Section 4.2.1.

for E, the energy difference is estimated as:

$$\Delta E = E - E_{ref} \approx \frac{\sum_{n=1}^{N} E_{loc}(\vec{r}^{(n)})w(\vec{r}^{(n)})}{\sum_{n=1}^{N} w(\vec{r}^{(n)})} - \frac{1}{N}\sum_{n=1}^{N}(E_{loc})_{ref}(\vec{r}^{(n)}) \tag{4.28}$$

with local values at any point $\vec{r}^{(n)}$ defined as in Eq. (4.22) and Eq. (4.25):

$$E_{loc} = \frac{\langle\Psi|H|\Psi\rangle_{s,t}}{\langle\Psi|\Psi\rangle_{s,t}}, \qquad (E_{loc})_{ref} = \frac{\langle\Psi_{ref}|H|\Psi_{ref}\rangle_{s,t}}{\langle\Psi_{ref}|\Psi_{ref}\rangle_{s,t}}, \qquad w = \frac{\langle\Psi|\Psi\rangle_{s,t}}{\langle\Psi_{ref}|\Psi_{ref}\rangle_{s,t}}. \tag{4.29}$$

Taking advantage of correlated sampling, the same reference walk can be used in several subsequent adjustments of parameters before a new reference walk should be generated for the best new wavefunction. A good reason to produce a new reference walk is when the energy has been lowered significantly, i.e. when the absolute value of the energy gain ΔE between the reference and the best new energy becomes larger than the error on the reference energy, ideally by at least a factor of two. Another reason to update the reference walk is if the wavefunction Ψ with adjusted parameters starts to differ significantly from Ψ_{ref}, which is signalled by local weights. Correlated sampling is reliable provided that local weights $w(\vec{r_n})$ in Eq. (4.29) do not significantly exceed their average value. If the parameters are changed too much, a single weight or a few large weights will dominate over the others in Eq. (4.28), thus biasing the energy difference estimate. To avoid this negative effect in MiCH, all local weights should be smaller than about 10-20 times their average.

The valence part of the wavefunction in Eq. (4.3) is a linear combination of basis functions, each of which depends on continuous and discrete parameters. When these parameters are changed, the linear expansion coefficients c in Eq. (4.3) can be determined via the energy matrix diagonalization in Eq. (2.25). Formally, the wavefunction is written as $\Psi = \sum_i c_i\Psi_i$ and matrix elements $\boldsymbol{H}_{ij}$ and $\boldsymbol{I}_{ij}$ in Eq. (2.26) are computed in correlated sampling on a reference walk generated by the previous best guess for the wavefunction. Again, as for expectation values of operators in Eq. (4.24), the overall normalization of the sampling function is not needed. Unlike the overlap matrix $\boldsymbol{I}$, the Hamiltonian matrix $\boldsymbol{H}$ estimated on a finite random walk may not be symmetric. Following the arguments in [146], we do not symmetrize the energy matrix. The overlap matrix may be ill-conditioned because of the possible linear dependence of valence terms. When that happens, the overlap matrix is regularized by a singular value decomposition from Sect. 2.6 in [147] and the non-symmetric generalized eigenvalue problem of type Eq. (2.25) is solved with the aid of numerical libraries [148].

In general, non-linear parameters ρ_0 do not need to be the same in all valence terms in Eq. (4.3), as is common in three-body models. In fact, as suggested by the success of SVM, it could be beneficial to mix valence terms with different values of ρ_0, especially because the core-valence antisymmetrizer in Eq. (4.3) removes the orthogonality properties of valence terms. We have tested several methods to optimize non-linear parameters in tandem with energy matrix diagonalization and correlated sampling. A stochastic selection in the fashion of SVM turns out to be inefficient because of the computational demand required to calculate the energy for a single set of parameters. There exist deterministic optimization methods analyzing the local dependence of the mean energy (Newton method) [149] and the wavefunction [150] on variational parameters. These deterministic methods have been tuned for and proved efficient in atomic and molecular physics, but upon testing them in MiCH, they do not seem to be adequately robust to meet our needs. In MiCH, the added complexity is most likely due to spin-isospin contaminations in the wavefunction and highly state-dependent, (non-)central, nuclear interactions. Also, at the beginning of the optimization route, the nucleus is three-body unbound. This can be seen, for example, from Figure 4.5, where ^{6}He containing a single valence term is bound by about -27.5 MeV, a value to be compared with the binding energy of the ^{4}He core, -30.77 MeV, given in Section 4.2.2. All the optimization methods mentioned tend to break the nucleus apart, unless the radius of the nucleus is constrained. Additionally, correlated sampling is reliable only for small changes in non-linear parameters.

The easiest way to control the size of the nucleus is to make the non-linear parameter ρ_0 the same in all valence terms, and that is the approach in this work. Even then, however, this parameter is a true variational parameter, which needs to be tuned to minimize the binding energy. From a distant view, our optimization method resembles that of three-body models: for an optimum value of the parameter ρ_0, the number of valence channels in the wavefunction is increased until convergence in energy is reached. However, on closer inspection, there are some major differences.

All the previous comments on parameter optimization are valid in general. We now turn to ^{6}He, the nucleus to be studied in Chapter 5. First, we consider the nucleus bound by a soft-core effective central nucleon-nucleon interaction, such as MN in Section 3.2.1. In this case, the ^{4}He core contains only basis terms with $L = S = 0$, as we have seen in Section 3.2.2. This makes valence neutrons in spin-singlet and spin-triplet states orthogonal. In the three-body analysis of ^{6}He in Section 2.4.3, spin-triplet states were present in the wavefunction only due to the spin-orbit interaction. It is then sufficient to consider spin-singlet valence terms only. The optimization begins with a single, $K = 0$ or 2, $n_{lag} = 0$ valence term attached to the core. Valence terms with higher hyper-momenta and degree of hyper-radial polynomials are added to the wavefunction until convergence in the binding energy is reached. The value of ρ_0 is adjusted to keep the rms proton radius of ^{6}He close to its experimental value. To avoid high partial waves in the valence part, both Y and T Jacobi configurations are mixed. After each addition of (few) new valence terms, linear coefficients c in Eq. (4.6) are determined via energy matrix diagonalization. Despite numerical evaluation of energy and overlap matrices, the lowest eigensolution of Eq. (2.25) is numerically stable even when the matrices are of appreciable size, of the order of 100×100 elements. Starting with a converged wavefunction, different values of ρ_0 are tested using correlated sampling and energy matrix diagonalization to finally locate the energy minimum.

To prevent numerical difficulties, valence terms with $n_{lag} \neq 0$ should be avoided until a preliminary convergence of $n_{lag} = 0$ terms with the hyper-momentum K has been reached. The reason is that higher-order hyper-radial terms may produce extraordinarily large local values of kinetic energy making the Monte Carlo energy averaging harder to converge. In the present work, the problem of large local kinetic energies is called the problem of bad points and is discussed in detail in Section B.1.

Parameter optimization is more involved in the presence of the non-central spin-orbit force between nucleons. As mentioned in Section 3.2.2, the spin-orbit force mixes $L = S = 0$ and $L = S = 1$ Gaussians in the wavefunction of ^{4}He. When attached to such a core, valence spin-singlet and spin-triplet terms are not necessarily orthogonal in the fully antisymmetrized wavefunction of ^{6}He; some of them may be almost orthogonal, though. Consequently, the overlap matrix $\boldsymbol{I}$ may contain many very small elements which are hard to distinguish from statistical noise. The energy matrix $\boldsymbol{H}$ is affected less severely. Under such circumstances, the energy matrix diagonalization may be numerically unstable yielding unreliable eigenvectors of linear coefficients c. Thankfully, the lowest energy eigenvalues are still numerically stable. These are effects at the edge of numerical stability and given the statistical sampling, their severity varies between random walks. To circumvent this problem, a major modification was introduced into the parameter optimization procedure described above for ^{6}He bound by central forces, namely a comparative optimization on two independent random walks. The details of this improved method are rather technical and as such are relegated to Appendix C.

Chapter 5

^{6}He in MiCH

We are now ready to put the model developed in this work to the test. In previous chapters, we have described all components going into the model including numerical techniques needed to evaluate matrix elements and the variational optimization method. In this chapter, the model is applied to the ground state of the simplest two-neutron halo nucleus, ^{6}He.

The chapter starts with a study of antisymmetrization effects in ^{6}He. As we will see, these effects are crucial for binding of ^{6}He. Then, basic observables computed for optimized ^{6}He wavefunctions will be presented and compared with experimental data and values obtained in other theoretical models. To appreciate the amount of details going into different models, the discussion will continue with a more detailed comparison of results obtained within MiCH and within the three-body model from Section 2.4. Finally, the chapter will be concluded by an application of MiCH to a two-neutron transfer reaction involving ^{6}He.

5.1 Antisymmetrization effects in ^{6}He

In this section, the effects of antisymmetrization operators in Eq. (4.6) are studied. Unlike in three-body models, wavefunctions in MiCH can be properly antisymmetrized to account for the fermionic nature of nucleons. Core-valence antisymmetrization should make states occupied inside ^{4}He unavailable for valence particles. The antisymmetrization of the valence part ensures the Pauli principle between valence neutrons, a requirement important especially in the Y Jacobi basis in which, unlike in the T basis, the valence basis terms from Eq. (4.2) do not meet the Pauli principle by construction.

In the current section, "a (valence) channel" means ^{6}He containing the MN-SO ^{4}He core from Section 3.2 and a single valence term characterized by a set of numbers $\{K, l_x, l_y, L, S, n_{lag}, \mathrm{Y/T}\}$. Ground states of both ^{4}He and ^{6}He have $J^\pi = 0^+$, and so the total angular momentum and parity of each valence channel must be $J^\pi_{val} = 0^+$. The system is bound by the MN-SO interaction from Section 3.2.1.

We focus on valence channels with the lowest hyper-momenta, namely with $K = 0$ and 2.[1]. Possible combinations of angular momentum quantum numbers for such channels are shown in Table 5.1. The table also shows whether a given channel in the T Jacobi basis is blocked by the Pauli principle between valence neutrons. Due to their trivial (constant) hyper-angular dependence, $K = 0$ channels contain the "lowest" core-valence s-waves ($l_x = 0$) in the Y Jacobi basis, and as such are expected to be the most core-valence Pauli-blocked.[2] On the other hand, $K = 2$ channels are expected to be crucial for the structure of ^{6}He, as has been demonstrated in Section 2.4.3. For $K = 2$ channels, squares of the Raynal-Revai coefficients for angular transformations between Y and T Jacobi sets from Eq. (2.27) are shown in Table 5.2.

Figure 5.1 shows binding energies of channels with $K = 0$ and 2, and $n_{lag} = 0$ and 1 for different values of the valence hyper-radial parameter ρ_0. For each channel, three energy curves are shown differing by whether the antisymmetrizers $\mathcal{A}^{val}$ and $\mathcal{A}^{core-val}$ in Eq. (4.6) are active or not. For each channel, both antisymmetrizers are first disabled, then $\mathcal{A}^{val}$ is switched on, followed by the activation of $\mathcal{A}^{core-val}$. We observe in Figure 5.1 that when the core-valence antisymmetrizer does not act, the valence antisymmetrizer has barely any effect on T Jacobi channels. It must be so because these channels satisfy

---

[1] $K = 1$ channels are not allowed because they would have to combine s- and p-waves due to Eq. (2.8) The parity of such channels would be negative which violates the requirement of positive parity of the valence part.

[2] Remember that in a first approximation ^{4}He can be thought of as four nucleons sitting in the lowest s-shell.

Table 5.1: Possible combinations of angular momentum quantum numbers for $K = 0$ and $K = 2$ channels.

K	l_x	l_y	L	S	Pauli blocked by Eq. (2.23) in T Jacobi basis	alias
0	0	0	0	0	no	$K = 0$ s-waves
2	0	0	0	0	no	$K = 2$ s-waves (spin-singlet)
2	1	1	0	0	yes	$K = 2$ p-waves spin-singlet
2	1	1	1	1	no	$K = 2$ p-waves spin-triplet

the Pauli principle between valence neutrons by construction.

For a given n_{lag}, $K = 0$ s-waves are essentially identical in Y and T Jacobi bases, as we discussed in Section 2.2. Without core-valence permutations, $K = 0$ s-waves with $n_{lag} = 0$ and 1 form deep energy minima in Figure 5.1(a). These minima, however, are removed upon the action of $\mathcal{A}^{core-val}$. Interestingly enough, the fully antisymmetrized $K = 0$, $n_{lag} = 1$ channel is bound more than the most trivial of all valence channels, the channel with $K = 0$, $n_{lag} = 0$, which is simply a manifestation of the Pauli principle. The $K = 0$, $n_{lag} = 0$ channel puts a neutron in the Y basis into the radially most trivial s-wave ($l_x = 0$) motion around the core, which makes this channel strongly forbidden by the core-valence Pauli blocking. On the other hand, due to its non-trivial hyper-radial dependence, the channel with $K = 0$, $n_{lag} = 1$ contains "less" trivial core-valence s-waves, which makes it "less" forbidden by the Pauli principle.

We start the analysis of $K = 2$ channels by $K = 2$ s-waves in the T Jacobi basis, i.e. by Figure 5.1(b). When the valence neutrons are not antisymmetrized with nucleons

Table 5.2: Squares of the Raynal-Revai coefficients $\langle l'_x l'_y | l_x l_y \rangle_{KL}$ from Eq. (2.27) for angular transformations of $K = 2$ valence channels between Jacobi sets. $\langle l'_x l'_y | l_x l_y \rangle_{KL}$ corresponds to a transformation from the unprimed to the primed Jacobi set, or schematically unprimed → primed.

	$[\langle 00 \vert 00 \rangle_{20}]^2$	$[\langle 11 \vert 00 \rangle_{20}]^2$	$[\langle 00 \vert 11 \rangle_{20}]^2$	$[\langle 11 \vert 11 \rangle_{20}]^2$	$[\langle 11 \vert 11 \rangle_{21}]^2$
Y → T	0.04	0.96	0.96	0.04	1.00
T → Y	0.04	0.96	0.96	0.04	1.00

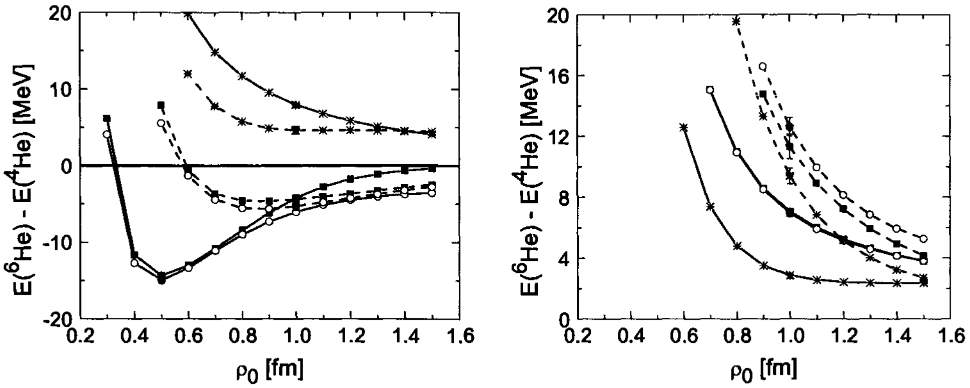

(a) $K = 0$ s-waves in T basis

(b) $K = 2$ s-waves in T basis

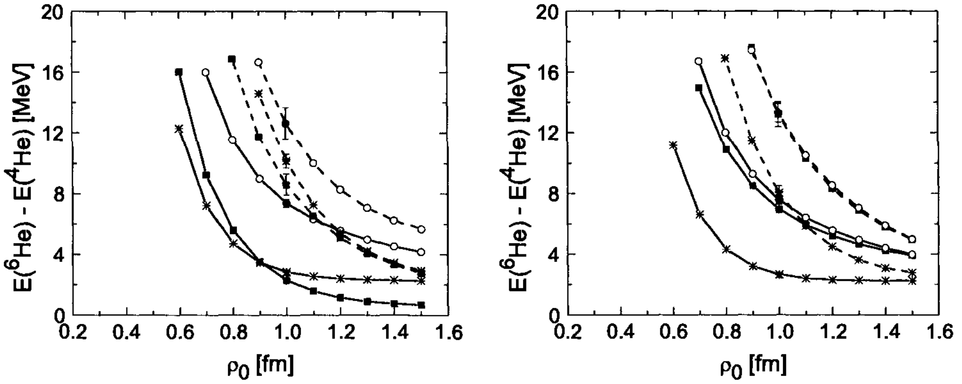

(c) $K = 2$ s-waves in Y basis

(d) $K = 2$ p-waves spin-singlet in Y basis

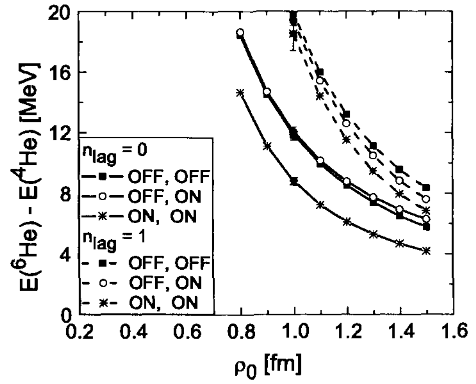

(e) $K = 2$ p-waves spin-triplet in T basis

Figure 5.1: Three-body binding energy of valence channels as a function of the non-linear parameter ρ_0 for different antisymmetrization settings. The legend is the same in all panels. For each channel, the OFF/ON switches indicate whether the corresponding antisymmetrizer in Eq. (4.6) is active or not: the first switch controls $\mathcal{A}^{val}$, the second switch is for $\mathcal{A}^{core-val}$. Energy curves are constructed in correlated sampling on walks for reference values of ρ_0; for each curve, reference energy is depicted by a star. Error bars appear on reference values only.

inside the core, ^{6}He behaves as a pure three-body system core + n + n. It is three-body unbound with binding energy monotonically heading towards the three-body threshold (i.e. towards the binding energy of ^{4}He) as the hyper-radial scaling length ρ_0 increases. Larger ρ_0 implies larger average hyper-radii and thus larger ^{6}He through the three-body relationship in Eq. (2.29). Therefore, the gain in binding energy with increased ρ_0 is misleading, because the nucleus gradually breaks apart into the core and two neutrons. This undesired trend is changed dramatically once $\mathcal{A}^{core-val}$ is switched on, because the core-valence exchange effects deliver extra binding to the system. Such a simple, fully antisymmetrized ^{6}He with $n_{lag} = 0$ remains three-body unbound, but the binding energy saturates for a fairly large interval of ρ_0 in Figure 5.1(b). This saturation forms a foundation on which a variationally optimized ^{6}He in Section 5.2 will eventually become bound against the three-body break-up. Using Table 5.2, $K = 2$ s-waves in the T Jacobi basis consist of 96% $K = 2$ p-waves spin-singlet state in the Y basis. Therefore, in the Y basis a neutron is mostly in a relative p-wave motion around the core, making the channel $K = 2$ s-waves in the T Jacobi basis mostly Pauli allowed.

The response of the other two $K = 2$ spin-singlet channels from Table 5.1, s-waves and p-waves spin-singlet in the Y basis, can also be easily understood. We first look at $K = 2$ s-waves in the Y basis, i.e. by Figure 5.1(c). In the absence of both $\mathcal{A}^{val}$ and $\mathcal{A}^{core-val}$ antisymmetrizers, this channel (for a given n_{lag}) is bound the most among all $K = 2$ channels, as can be seen from Figure 5.1. The reason for this is that in this channel one of the neutrons would be in an s-wave ($l_x = 0$) motion relative to the core, making the entire channel fairly bound. The binding is weaker than for $K = 0$ s-waves though. As soon as the valence particles are antisymmetrized, however, several MeV of the binding energy in Figure 5.1(c) are lost in this channel, which can be explained as follows. Using Table 5.2, we can write schematically:

$$\begin{aligned} K = 2 \text{ s} - \text{waves in Y} \;\longrightarrow\;& 4\%\ K = 2 \text{ s} - \text{waves in T} + \\ & 96\%\ K = 2 \text{ p} - \text{waves spin} - \text{singlet in T}. \end{aligned}$$

However, the p-wave admixture in the T basis is completely eliminated by the action of $\mathcal{A}^{val}$, because it is Pauli blocked in Table 5.1, and the original channel effectively turns to $K = 2$ s-waves in the T basis. Upon a rotation back to the Y basis and using Table 5.2 again, one obtains:

$$K = 2 \text{ s} - \text{waves in Y} \xrightarrow{\mathcal{A}^{val}} K = 2 \text{ s} - \text{waves in T} \longrightarrow$$

$$4\% \; K = 2 \text{ s} - \text{waves in Y} + 96\% \; K = 2 \text{ p} - \text{waves spin} - \text{singlet in Y}.$$

The result is a dramatic structural change: the original s-waves in the Y basis become mostly p-waves in the same basis putting a neutron into a p-wave ($l_x = 1$) relative to the core. The net result is the above-mentioned loss of binding. Similar analysis can be done for $K = 2$ p-waves spin-singlet in the Y basis (Figure 5.1(d)):

$$K = 2 \text{ p} - \text{waves spin} - \text{singlet in Y} \xrightarrow{\mathcal{A}^{val}} K = 2 \text{ s} - \text{waves in T} \longrightarrow$$

$$4\% \; K = 2 \text{ s} - \text{waves in Y} + 96\% \; K = 2 \text{ p} - \text{waves spin} - \text{singlet in Y},$$

and so the structural change due to the action of $\mathcal{A}^{val}$ is far less dramatic because the channel remains mostly p-waves in the Y basis. Once valence particles in $K = 2$ spin-singlet states in the Y basis are antisymmetrized, these channels become equivalent to $K = 2$ s-waves in the T basis. Therefore, the core-valence exchange effects in these channels can be understood on the merit of the discussion for $K = 2$ s-waves in the T basis.

The remaining $K = 2$ channels in Table 5.1 contain valence particles in a spin-triplet state. For a given n_{lag}, there is only one such state in the Y basis and one in the T basis. Therefore, they must be essentially identical upon rotations of Jacobi bases, as is also demonstrated by corresponding Raynal-Revai coefficients in Table 5.2. The energy gain in these channels due to antisymmetrization effects is not large enough to produce a saturated energy curve in Figure 5.1(e).

In summary, at the level of single valence channels, the antisymmetrization exchange effects have significant impact on ^{6}He. Not only do they enforce the fermionic nature of the nucleus, but they also deliver extra binding to the system. Similar analysis could be done for valence channels with higher hyper-momenta, but we have limited our discussion to valence channels that are crucial for the structure of ^{6}He. We convinced ourselves that general observations made in this section depend neither on the value of the mixture parameter u in the Minnesota interaction nor on inclusion of the spin-orbit force.

5.2 Converged ^{6}He

Having understood the behavior of single valence channels, we now proceed to the optimization of the wavefunction of ^{6}He. Results are presented for two cases: MN and MN-SO defined in Section 3.2.1. More emphasis is put on MN-SO because it employs a more realistic nucleon-nucleon interaction due to the spin-orbit force. In both cases, the mixture parameter u in the central part of the interaction was adjusted to bind ^{6}He by about the right amount against the break-up into ^{4}He and two neutrons. Essentially, the interaction mixture parameter is the only free parameter in MiCH. The Coulomb interaction is neglected since it would barely shift absolute binding energies of both ^{4}He and ^{6}He by about the same amount. The wavefunctions for the ^{4}He core are taken from Section 3.2.2.

The convergence of the binding energy of ^{6}He relative to the three-body threshold with the number of valence terms in the wavefunction is shown in Figure 5.2. The variational optimization technique used in MiCH was described in Section 4.2.3. Here, a few comments are given on chronology in Figure 5.2.

The case MN is discussed first. The construction of the wavefunction begins with a single $K = 0$, $n_{lag} = 0$ valence channel with which the nucleus is three-body unbound. The scaling length ρ_0 is set to 0.80 fm to keep the rms proton radius of ^{6}He close to its experimental value 1.91 fm. Next, all valence channels with $K \leq 10$ and $n_{lag} = 0$ in both Y and T Jacobi bases are gradually added to form a fairly well defined wavefunction

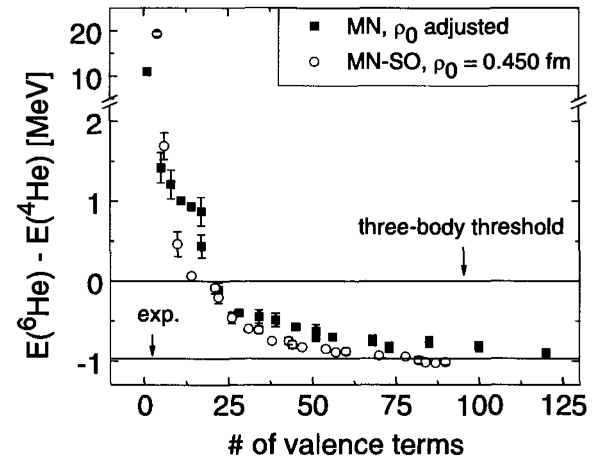

Figure 5.2: Convergence of the three-body binding energy of ^{6}He with the number of valence terms included in the wavefunction. In MN, the variational parameter ρ_0 is adjusted along the optimization route; in MN-SO, the results are for a fixed value $\rho_0 =$ 0.45 fm. See text for details. Error bars were not computed for all points, and even when present, they may be smaller than the actual symbol.

before valence terms with higher hyper-radial orders n_{lag} are considered. The parameter ρ_0 is slightly enlarged because the radius has become smaller due to stronger binding. The three-body binding energy of a still three-body unbound ^{6}He is about +0.5 MeV in Figure 5.2. Next, all valence terms with $K = 0$ and 2 and $n_{lag} = 1$ are added to the wavefunction and the three-body break-up threshold is finally crossed. By crossing the three-body threshold, the binding energy as a function of ρ_0 forms a variational minimum. From this moment on, ρ_0 is adjusted to approximately minimize the energy. It then takes another 118 valence terms to reach the converged value -0.90 MeV for the three-body binding energy. At the end, all spin-singlet valence terms with $K \leq 12$ and $n_{lag} \leq 5$ in both Y and T bases are included in the wavefunction.

Figure 5.3 shows the dependence of the three-body binding energy and the rms proton radius on the scaling length ρ_0 for converged ^{6}He. In the MN case, the variational energy minimum is located around $\rho_0 = 0.45$ fm. The steep reduction in binding below $\rho_0 = 0.40$ fm in Figure 5.3(a) reflects trends observed in Figure 5.1. By reducing ρ_0, the nucleus becomes smaller in Figure 5.3(b) because the valence neutrons are forced to stay closer to the core. As a consequence, the binding of ^{6}He is reduced due to the increase

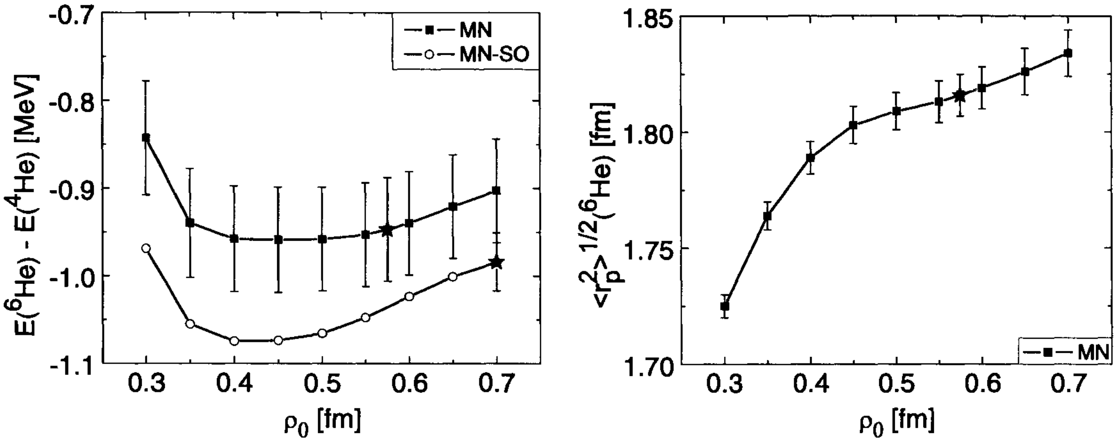

(a) Three-body binding energy. (b) Rms proton radius.

Figure 5.3: Dependence of the three-body binding energy and the rms proton radius of converged ^{6}He on the non-linear parameter ρ_0. All curves are constructed in correlated sampling on walks for reference values of ρ_0. Reference values of observables are depicted by stars.

of total kinetic energy of the system. On the other side, for very large values of ρ_0, the valence neutrons are forced to spend more time farther from the core, and the size of the nucleus increases and the binding becomes weaker.

The optimization procedure in the MN-SO case is more complicated, as described in Appendix C. In this case, the wavefunction is tailored to a specific value of ρ_0. The wavefunction is first optimized for $\rho_0 = 0.70$ fm, a value that prevents ^{6}He from getting too large at the beginning of the optimization when the nucleus is still three-body unbound. Using the method of a comparative optimization outlined in Appendix C, a fairly converged wavefunction is constructed. For this wavefunction, a reference walk is produced. On this walk in correlated sampling, the binding energy is estimated for an auxiliary ^{6}He containing a set of all 222 valence terms with $K \leq 14$ and $n_{lag} \leq 5$ for different values of ρ_0. The corresponding energy curve is shown in Figure 5.3(a). Because for this auxiliary ^{6}He only energy eigenvalues are reliably determined in the energy matrix diagonalization, neither error bars nor radii are shown. The energy minimum is formed around $\rho_0 = 0.45$ fm, a value for which the wavefunction is optimized again, and the convergence plot is shown in Figure 5.2. At the point where ^{6}He becomes three-body bound, a subset of about 15 valence terms with $K \leq 6$ and $n_{lag} \leq 2$ is included in the wavefunction. Altogether ninety carefully selected valence terms having $K \leq 14$ and $n_{lag} \leq 5$ are needed to reach energy convergence in the MN-SO case.

Several extra remarks regarding the variational optimization are appropriate at this point. First, the convergence plots in Figure 5.2 are not unique. If the history plots were constructed again, they would look differently depending on several factors, such as the order in which valence terms are added to the wavefunction; the exact values of ρ_0 used throughout the optimization; statistical effects due to random sampling etc. However, we convinced ourselves that the converged results from Figure 5.2 would be reproduced. Second, in Chapter 2, the valence basis in Eq. (2.18) is orthogonal and complete, and converged results obtained within the three-body model should be independent of ρ_0. In MiCH, the orthogonality of valence terms is destroyed by the core-valence antisymmetrizer. As expected, the non-linear parameter ρ_0 is then a variational parameter, as would also be suggested by a formation of energy minima in Figure 5.3(a). Last, in the following discussion, converged results for ^{6}He are for $\rho_0 = 0.45$ fm in both MN and MN-SO cases.

Once the wavefunctions have been optimized, we can calculate binding energies and rms point matter, point proton and point neutron radii for ^{6}He. Radii are computed as square roots of expectation values of operators in Eq. (2.28), Eq. (2.30) and Eq. (2.32). The results are shown in Table 5.3 along with experimental values and results obtained in a variety of other models: the macroscopic three-body model from Chapter 2 and Section 2.4 in particular, SVM [76] as a representative of microscopic cluster theories, and the Green's function Monte Carlo (GFMC) [117] representing microscopic models. Preliminary results from the MN model have been published in [153].

Let us first comment on experimental values of radii. What has become experimentally known with a great accuracy are nuclear charge radii $\langle r_c^2 \rangle^{1/2}$ of ^{4}He and ^{6}He. However, in our calculations, nucleons are treated as point particles, and rms point proton radii $\langle r_p^2 \rangle^{1/2}$ are calculated. Following [47], the charge and the point proton radii are related

Table 5.3: Binding energies E and three-body binding energies E_{3body} in [MeV] and rms point nucleon radii in [fm] of ^{4}He and ^{6}He from various models along with experimental values. MN and MN-SO are results of this work, the other models are the three-body model from Chapter 2, SVM [76] and GFMC [117]. Experimental proton radii were computed by means of Eq. (5.1) using charge radii from references cited in the table. Values labelled with * were computed; for radii, the relationship from Eq. (2.33) was used, GFMC three-body binding energy was obtained using binding energy -29.4(1) MeV of ^{6}He from [117]. The thickness of the neutron halo is defined as $\Delta r = \langle r_n^2 \rangle^{1/2} - \langle r_p^2 \rangle^{1/2}$.

		MN	MN-SO	3body	SVM	GFMC	exp.
^{4}He	E	-30.85	-30.93	N/A	-25.60	-28.37(3)	-28.30 [118]
	$\langle r_p^2 \rangle^{1/2}$	1.40	1.40	1.40	1.41	1.45(0)	1.46(1) [151]
^{6}He	E_{3body}	-0.90(5)	-1.02(3)	-0.98	-0.96	-1.03(10)*	-0.97 [25]
	$\langle r_m^2 \rangle^{1/2}$	2.41(1)	2.32(1)	2.49	2.42	2.55(1)*	2.48(3) [152] 2.33(4) [18]
	$\langle r_p^2 \rangle^{1/2}$	1.81(1)	1.75(1)	1.86	1.81	1.91(1)	1.91(2) [47]
	$\langle r_n^2 \rangle^{1/2}$	2.67(1)	2.56(1)	2.75	2.68	2.82(1)	2.72(4)* 2.51(6)*
	Δr	0.86(1)	0.81(1)	0.89	0.87	0.91(1)	0.81(4) 0.60(6)

as

$$\langle r_p^2 \rangle = \langle r_c^2 \rangle - \langle R_p^2 \rangle - \langle R_n^2 \rangle \frac{N}{Z}, \tag{5.1}$$

where $\langle R_p^2 \rangle^{1/2} = 0.895(18)$ fm [154] is the rms charge radius of the proton, $\langle R_n^2 \rangle = -0.120(5)$ fm^2 [155, 156] is the mean-square charge radius of the neutron, and N and Z are nuclear neutron and proton numbers. We used values 1.681(4) fm [151] and 2.054(14) fm [47] for charge radii of ^{4}He and ^{6}He, respectively. The corresponding proton radii are shown in Table 5.3. In literature, matter radius of ^{6}He has been extracted from relevant interaction cross-section data; however, the extracted values disagree, as listed in Table 5.3, according to the type of analysis performed.

In our calculations, a free ^{4}He in Table 5.3 turns out to be overbound and smaller relative to experimental data. The fact that we differ from experimentally known absolute binding energies was expected because of the effective nucleon-nucleon interactions employed. We are, however, mostly interested in three-body-like features of ^{6}He. The three-body binding energy is approximately reproduced after a slight tuning of the mixture parameter u in the Minnesota interaction. Our proton radii of ^{6}He are smaller than they should be which may be a consequence of a smaller ^{4}He core. On the other hand, matter radii are comparable with those deduced from experiments. Perhaps due to stronger three-body binding, MN-SO ^{6}He is slightly smaller than its MN counterpart. Nevertheless, proton and neutron radii change consistently so that the thickness of the neutron halo does not change dramatically between MN and MN-SO.

Next, MN and MN-SO results are compared with those of other models listed in Table 5.3. In the three-body calculations in Section 2.4, the binding energy and the size of ^{4}He core do not enter the actual three-body calculations, but the radius of the core is needed to compute the size of ^{6}He. In the three-body picture, radii of ^{6}He are simply related to the radius of the core via Eq. (2.29) and Eq. (2.31). For the best comparison between our and three-body results, we assume the same radius of ^{4}He in the three-body model as in MN-SO. Then, in a naive three-body picture, the larger size of ^{6}He in the three-body model (when compared to MN-SO) is solely due to the valence neutrons living on average slightly farther from the core. The three-body model is also useful to assess how strongly radii of ^{6}He depend on the size of the core. If the radius of the core is increased to its experimental value 1.46 fm, then radii of ^{6}He become $\langle r_m^2\rangle^{1/2} = 2.51$ fm, $\langle r_p^2\rangle^{1/2} = 1.90$ fm, $\langle r_n^2\rangle^{1/2} = 2.77$ fm and $\Delta r = 0.86$ fm. With these new values, the experimental proton radius of ^{6}He is perfectly reproduced, and the neutron halo shrinks a bit.

Within SVM, ^{6}He has been studied in the past repeatedly [76,132,133]. In Table 5.3, SVM results obtained in [76] are quoted where central and spin-orbit Minnesota and Coulomb interactions were employed. In the later reference, several different cluster compositions were considered to study break-up of the core in ^{6}He. In Table 5.3, results for ^{4}He correspond to model α_2 in [76], i.e. to an α-particle wavefunction of which is a superposition of three 1s harmonic oscillator Slater determinants with common oscillator parameters set to minimize the α's ground-state energy. Due to this very simple picture, SVM ^{4}He in table Table 5.3 is bound less than ^{4}He in MN and MN-SO cases. The SVM results for ^{6}He in Table 5.3 are those from model (b) in [76]. In that model, ^{6}He was modelled as a combination of ^{4}He + n + n and t + t with tritons again built from simple 1s harmonic oscillators. The importance of the triton channel was first observed in [134], where this channel was introduced to overcome the insufficient three-body binding of ^{6}He. SVM three-body binding energies and radii of ^{6}He are comparable with ours, especially with the MN model.

For the sake of completeness, we also show microscopic GFMC results in Table 5.3. These were obtained using realistic two-body AV18 and three-body IL2 interactions. We show GFMC results to point out that by using modern realistic potentials in microscopic calculations, absolute binding energies and proton radii of ^{4}He and ^{6}He can indeed be reproduced. However, as we argued in Chapter 1, questions may arise about how microscopic models treat asymptotic regions so important for Borromean halo nuclei.

We have also computed the point nucleon density distributions. For the more realistic MN-SO case, they are plotted in Figure 5.4 along with density distributions obtained in other models from Table 5.3. For comparison, the figure also contains the proton (equal to neutron) density for the MN-SO ^{4}He. These nucleon densities are calculated as simple δ-function expectation values:

$$\frac{1}{4\pi r^2}\frac{1}{\langle\Psi|\Psi\rangle}\left\langle\Psi\left|\sum_{i=1}^{A}\frac{1\pm\tau_{z,i}}{2}\delta\left(r-|\vec{r}_i-\vec{r}_{CMS}|\right)\right|\Psi\right\rangle \tag{5.2}$$

with ± for proton and neutron densities, respectively. Here, τ_z is the operator of isospin projection from Appendix A. For a nucleus with mass number A, the integral is carried over all spatial coordinates $\vec{r}_i$ as well as all nucleonic spins and isospins. To compute the densities corresponding to the three-body model, we constructed an auxiliary wavefunction of ^{6}He of type Eq. (4.6) by combining the MN-SO ^{4}He and the valence part taken from the three-body wavefunction of ^{6}He obtained in Section 2.4. In such auxiliary wavefunction, the core-valence antisymmetrizer in Eq. (4.6) was switched off because the Pauli principle was approximately taken into account when the three-body wavefunction was constructed in Section 2.4. In logarithmic scale, proton and neutron densities from

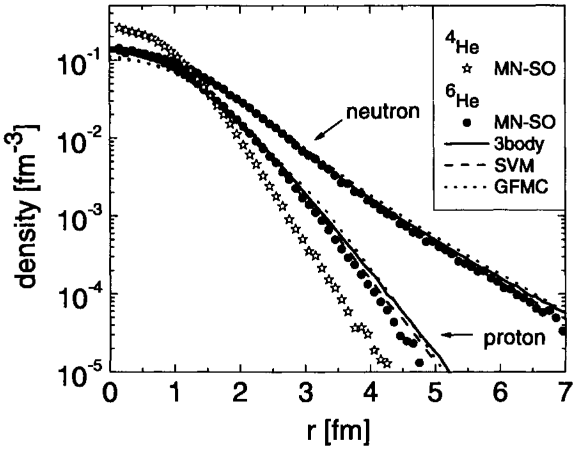

Figure 5.4: Point proton and point neutron density distributions in ^{6}He for models from Table 5.3 except MN. The GFMC densities are from [66]. Also, for comparison, the proton (=neutron) density of the MN-SO ^{4}He is shown. All proton (neutron) distributions are normalized to the number of protons (neutrons).

different models of ^{6}He are close to one another with small differences reflecting slightly different radii and wavefunction compositions. All models reproduce the most pronounced property, namely the neutron distribution extending far beyond that of protons. In other words, they reproduce the neutron halo of ^{6}He. Depleted at short distances, the proton density of ^{6}He stretches farther out than that for a free ^{4}He. A partial explanation of this effect comes from the three-body model: in ^{6}He, the α core does not sit at the center of mass of the entire system, and its motion relative to the center of mass spreads out the proton distribution. Due to the same effect, the neutron density in ^{6}He is also expected to be depleted at small distances relative to that of a free ^{4}He, as is also visible in Figure 5.4.

The effects of the Pauli blocking from Section 5.1 were tested further in the MN model. First we consider a case with the core-valence antisymmetrizer switched off. When the $K = 0$ valence channels are present in the wavefunction, the nucleus is three-body overbound by several tens of MeV, as one would expect based on Figure 5.1(a), where $K = 0$ s-waves are deeply three-body bound. When, however, $K = 0$ s-waves are all removed from the wavefunction, the nucleus becomes three-body unbound regardless of inclusion of valence terms with higher hyper-momenta. When the core-valence antisymmetrizer is switched back on, the converged ^{6}He is three-body bound by about -0.9 MeV from Table 5.3. When all the lowest $K = 0$ hyper-spherical channels are now removed from the converged wavefunction, the three-body binding decreases to about -0.75 MeV. It becomes evident that, to produce a meaningful ^{6}He, it is not sufficient to simply neglect the most Pauli-blocked $K = 0$ valence channels. Rather, all contributing valence channels should be included in the model space and subjected carefully to the antisymmetrization. This message is important especially for few-body models in which the core-valence forbidden states are removed approximately by different Pauli blocking techniques.

We can see that all models mentioned in Table 5.3, although different in their nature, are in a fair agreement on most commonly computed properties of ^{6}He. The agreement between densities in the three-body and MN-SO models is especially remarkable given how those densities were obtained. In MN-SO, the valence part of the microscopic wavefunction was built from the very beginning on top of a microscopic ^{4}He core; in the three-body model, the internal structure of the core was roughly accounted for through Pauli blocking, and only the final optimized three-body wavefunction was attached to a microscopic MN-SO core in order to obtain nucleon densities. In linear scale, densities from MN-SO and the three-body model are shown again in Figure 5.5. It looks like highly integrated properties, such as radii and densities, may not appreciate the amount of details built into different models of ^{6}He. We may then pose a question: is it really worthwhile to pursue a time-consuming microscopic approach to ^{6}He if a computationally cheap three-body route works so well? Provided the three-body picture of ^{6}He is well suited for a problem at hand, can we not simply use three-body wavefunctions for all our needs? One way to shed more light at this issue is to compare three-body wavefunctions directly with their analogs extracted from MiCH, with overlap functions.

5.3 Overlap functions

For a more detailed comparison with results obtained in the three-body model, the three-body-like core + n + n information needs to be extracted from MiCH. To access this

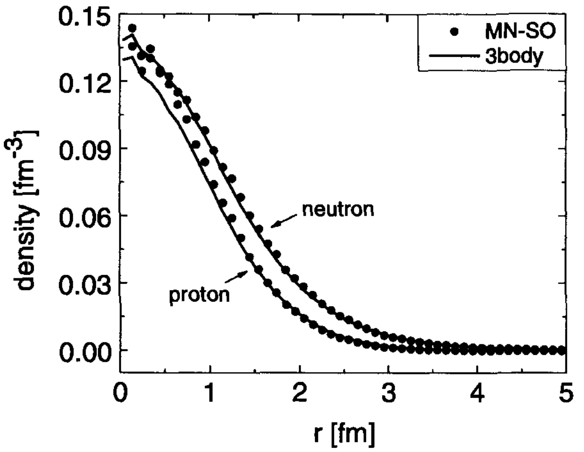

Figure 5.5: Point proton and point neutron density distributions in ^{6}He for MN-SO and three-body models from Table 5.3.

information, an overlap integral between a microscopically described two-neutron halo nucleus (Ψ) and its core (Φ) is computed:

$$\mathcal{I}_{M_{J_{val}}1-1} = \sqrt{\binom{A}{2}} \left\langle \Phi_{J^{\pi}_{core} M_{J_{core}} T_{core}\, M_{T_{core}}} \middle| \Psi_{J^{\pi} M_J T\, M_T} \right\rangle . \tag{5.3}$$

The binomial factor accounts for the number of combinations to pick two out of A nucleons. The integration is done over all degrees of freedom in the core Φ, and so the overlap integral $\mathcal{I}$ depends on degrees of freedom of two valence neutrons remaining outside the core. The integral has a good isospin and isospin projection 1 and -1, respectively, but it does not have a good angular momentum. It can be expanded in a complete set of hyper-harmonics with good angular momentum J^{π}_{val} from Eq. (4.1):

$$\mathcal{I}_{M_{J_{val}}1-1} = \sum_{\gamma_{val} J^{\pi}_{val}} C^{JM_J}_{J_{core} M_{J_{core}} J_{val} M_{J_{val}}} \mathcal{O}_{\gamma_{val} J^{\pi}_{val}}(\rho) \left[(\mu_1 \mu_2)^{3/4} \mathcal{Y}_{\gamma_{val} J^{\pi}_{val} 1-1} \right] , \tag{5.4}$$

where C are Clebsch-Gordan coefficients. As in Chapter 2, $\gamma_{val} = \{K, l_x, l_y, L, S, \mathrm{T}\}$. The expansion is carried out in the T Jacobi basis where the hyper-harmonics $\mathcal{Y}$ satisfy the Pauli principle by construction. The numerical factor $(\mu_1 \mu_2)^{3/4}$ is included to make the spatial part of hyper-harmonics orthonormal with respect to the weight factor

$(\mu_1\mu_2)^{-3/2}\sin^2\theta\cos^2\theta$ from the hyper-spherical volume element in Figure 2.1.[3] Note that the hyper-radial part in Eq. (5.4) is not expanded in the Laguerre basis from Eq. (2.16) because the basis functions $\mathcal{R}_{n_{lag}}$ do not have a good physical meaning. Instead, the overlap functions $\mathcal{O}$ are computed directly from:

$$\mathcal{O}_{\gamma_{val}J^{\pi}_{val}}(\rho') = \sqrt{\binom{A}{2}}\,(\mu_1\mu_2)^{3/4}\times \tag{5.5}$$
$$\left\langle \left[\Phi_{J^{\pi}_{core}T_{core}M_{T_{core}}} \otimes \mathscr{Y}_{\gamma_{val}J^{\pi}_{val}1-1}\right]_{J^{\pi}M_J T M_T} \left| \frac{\delta(\rho-\rho')}{\rho^5} \right| \Psi_{J^{\pi}M_J T M_T} \right\rangle,$$

where the integration is carried over degrees of freedom of all nucleons. Using these overlap functions, the three-body-like core + n + n component of the wavefunction Ψ can be written as:

$$\Psi^{overlap}_{J^{\pi}M_J T M_T} = \sum_{J^{\pi}_{core}\gamma_{val}J^{\pi}_{val}} (\mu_1\mu_2)^{3/4}\times \tag{5.6}$$
$$\left[\Phi_{J^{\pi}_{core}T_{core}M_{T_{core}}} \otimes \mathcal{O}_{\gamma_{val}J^{\pi}_{val}}\mathscr{Y}_{\gamma_{val}J^{\pi}_{val}1-1}\right]_{J^{\pi}M_J T M_T}$$

in the form similar to the three-body decomposition in Eq. (2.21). Moreover, the overlap wavefunction $\Psi^{overlap}$ satisfies a three-body Schrödinger equation with an additional source term due to the residual interaction between valence particles and those in the core [157]. Therefore, at least in the asymptotical regions, the three-body wavefunction from Eq. (2.21) and the overlap wavefunction $\Psi^{overlap}$ from Eq. (5.6) should behave similarly. On this merit, the three-body results and those from MiCH for ^{6}He can now be compared at the level of wavefunctions rather than integrated observables. A valence term characterized by a set γ_{val} will be refereed to as an overlap or a three-body channel. For ^{6}He, the three-body decomposition takes a simple product form:

$$\Psi^{overlap}_{0^+01-1}\left(^6\mathrm{He}\right) = (2/3)^{3/4}\Phi_{0^+00}\sum_{\gamma_{val}}\mathcal{O}_{\gamma_{val}0}\mathscr{Y}_{\gamma_{val}0^+1-1} \tag{5.7}$$

---

[3] Even though not mentioned, this factor was also included in three-body terms in Eq. (2.18).

In analogy with the three-body model and Eq. (2.11), it may be useful to work with modified overlap functions u:

$$u(\rho) = \rho^{5/2}\,\mathcal{O}(\rho) \tag{5.8}$$

Because of the orthonormality of hyper-harmonics, the norm of an overlap channel is given by:

$$S_{\gamma_{val} J^{\pi}_{val}} = \int_0^{\infty} \mathcal{O}^2_{\gamma_{val} J^{\pi}_{val}}(\rho)\rho^5\,\mathrm{d}\rho = \int_0^{\infty} u^2_{\gamma_{val} J^{\pi}_{val}}(\rho)\,\mathrm{d}\rho. \tag{5.9}$$

The last quantity is often called a spectroscopic factor. We will use this term also in connection with the three-body results for ^{6}He, where a spectroscopic factor gives the probability of a given channel in the three-body wavefunction, as we have seen in Table 2.1.

To compute overlap functions in a meaningful way, wavefunctions of both ^{4}He and ^{6}He need to be normalized. The normalization of the the core's wavefunction is known from SVM. The norm of ^{6}He wavefunction can be computed numerically, as is demonstrated in Appendix D. Here, both wavefunctions are assumed to be normalized to unity. The integration space in Eq. (5.5) is sampled by the square of the wavefunction $\Psi\left({}^6\mathrm{He}\right)$.

We extracted overlap functions for the MN-SO ^{6}He. To ensure small statistical errors, overlap functions were computed on two separate random walks, each containing four million integration points. At the end, the overlap functions from such two walks were averaged in each overlap channel to improve statistics even further.

Ordered by spectroscopic factors, the five strongest overlap channels in the MN-SO ^{6}He are listed in Table 5.4. These are the only channels that could be resolved, all other potential overlap channels have spectroscopic factors too small and as such are buried in numerical noise.[4] The table also contains spectroscopic factors for ^{6}He studied in the three-body model from Table 2.1. Surprisingly enough, not only the dominant channels are exactly the same in MN-SO and the three-body model, but also their order is preserved. In the three-body model, these five channels account for more than 98% of the wavefunction. Therefore, we expect that these channels should also grasp most

---

[4] It seems that an overlap channel can be resolved if its spectroscopic factor is larger than about 0.01, or equivalently about one hundredth of that for the strongest $K = 2$ s-waves channel.

Table 5.4: Spectroscopic factors of the five dominant overlap channels in ^{6}He. Three-body results are from Table 2.1. Numbers in parentheses are relative errors.

T Jacobi basis								
channel						S		
alias	K	l_x	l_y	L	S	3body	MN-SO	MN-SO / 3body
$K = 2$ s-waves	2	0	0	0	0	0.8089	1.1155 (0.5%)	1.38
$K = 2$ p-waves	2	1	1	1	1	0.1103	0.1859 (0.7%)	1.69
$K = 0$ s-waves	0	0	0	0	0	0.0417	0.0555 (2.1%)	1.33
$K = 6$ d-waves	6	2	2	0	0	0.0164	0.0266 (3.5%)	1.62
$K = 6$ f-waves	6	3	3	1	1	0.0078	0.0122 (3.0%)	1.56
					$\sum =$	0.9851	1.3957	

of the ^{4}He + n + n decomposition of the MN-SO ^{6}He. In the three-body model, the wavefunction is normalized to unity, and as a consequence, all spectroscopic factors are less than one. In MN-SO, however, $K = 2$ s-waves channel has a spectroscopic factor larger than one. To understand this difference, we need to dig deeper.

To see more clearly the difference between the three-body and the microscopically derived overlap wavefunctions, Figure 5.6 and Figure 5.7 show the hyper-radial dependence of the five channels from Table 5.4. We chose to show these functions as $u(\rho)$ because of their simpler asymptotic fall-off in Eq. (2.15). It is satisfying to observe that for all five channels, three-body and overlap hyper-radial functions agree on their rough properties, such as overall shape, and number of nodes. There are, however, a few obvious differences. First, absolute values at peaks are larger for overlap functions than for three-body functions. This difference is responsible for larger spectroscopic factors in Table 5.4 associated with overlap functions. Second, overlap functions tend to peak and reach nodes (other than the trivial node at $\rho = 0$ fm) slightly before three-body functions do. Also, peaks of overlap functions are steeper. Third, at larger hyper-radii, overlap functions decay a bit faster, as can also be seen from both Figure 5.6 and Figure 5.7. Overall, the overlap functions on average put more weight on smaller hyper-radii. We could then speculate that this shift of preferred hyper-radii might be indirectly reflected by smaller radii of the MN-SO ^{6}He in Table 5.3 when compared to radii from the three-body model.

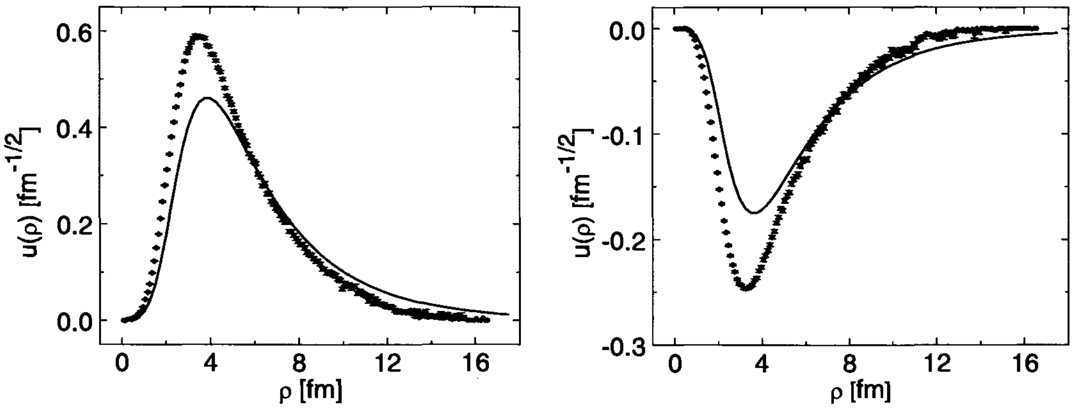

(a) $K = 2$ s-waves (b) $K = 2$ p-waves

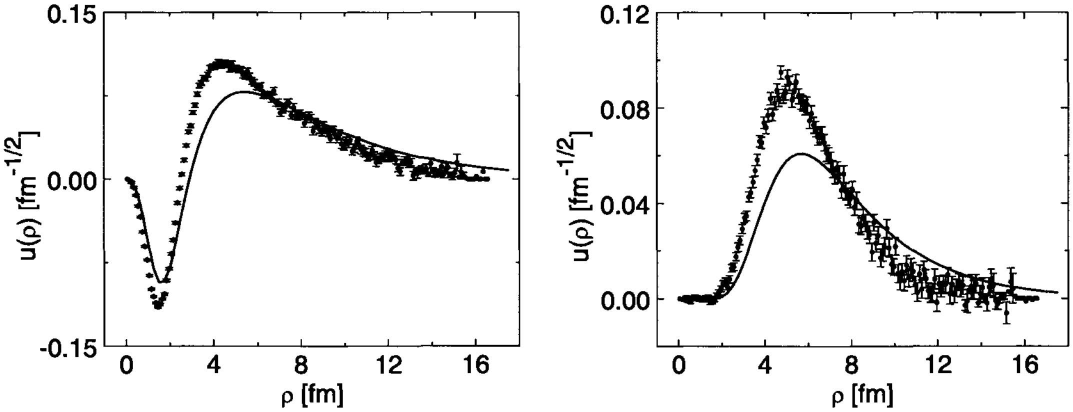

(c) $K = 0$ s-waves (d) $K = 6$ d-waves

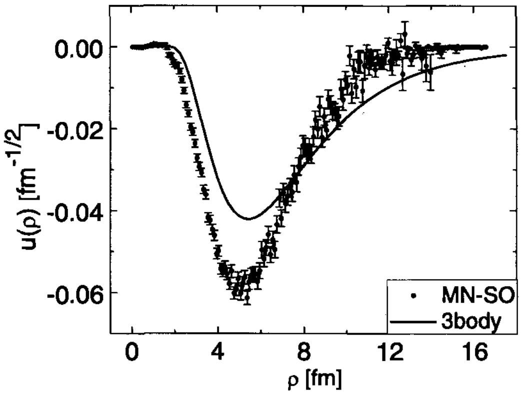

(e) $K = 6$ f-waves

Figure 5.6: Hyper-radial dependence of overlap and three-body wavefunctions for channels from Table 5.4. The three-body functions are from Figure 2.13. The legend is the same in all panels.

At hyper-radii beyond about 12 fm, MN-SO overlap functions in Figure 5.6 and Figure 5.7 become unreliable and their statistical fluctuations take over. The reason is that very large hyper-radii would place two neutrons into regions very distant from the

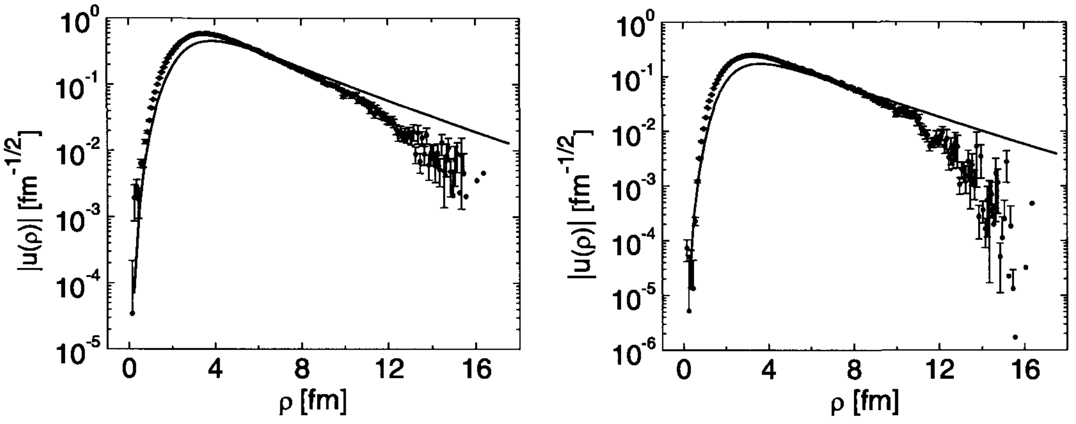

(a) $K = 2$ s-waves (b) $K = 2$ p-waves

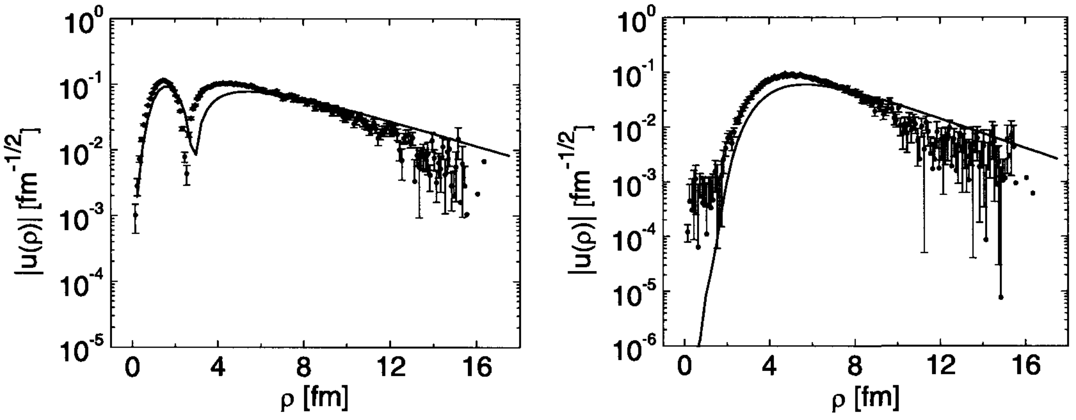

(c) $K = 0$ s-waves (d) $K = 6$ d-waves

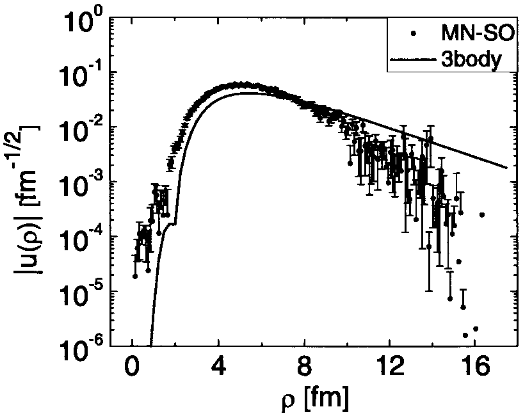

(e) $K = 6$ f-waves

Figure 5.7: Hyper-radial dependence of absolute values of overlap and three-body wavefunctions for channels from Table 5.4. The three-body functions are from Figure 2.13. The legend is the same in all panels.

core. In extreme configurations, a hyper-radius of 15 fm would correspond to a di-neutron at distance of about 13 fm from the center of the ^{4}He core, or to two neutrons on opposite sides of the core at a mutual distance of about 21 fm. And because the sampling probability is proportional to $\langle\Psi(^6\mathrm{He})|\Psi(^6\mathrm{He})\rangle_{s,t}$, such extreme spatial configurations are very unlikely to be visited by a walker during the course of a random walk. Moreover, samples in such distant regions may be highly correlated, an effect that has been seen in other Monte Carlo calculations, for example [90].

It is interesting to look at asymptotics of overlap functions a bit closer. As two neutrons are pulled out of ^{6}He, effects of the core-valence antisymmetrizer in Eq. (4.6) gradually vanish, and the full six-body wavefunction decouples into its ^{4}He + n + n asymptotical form. In asymptotic regions, the six-body wavefunction can be written as nothing else but a sum of overlap functions. Therefore, the asymptotics of overlap functions goes hand in hand with asymptotics of the many-body wavefunction in the core + n + n cluster channel. Both three-body and overlap hyper-radial functions should fall off exponentially with the decay parameter κ depending on the three-body binding energy via Eq. (2.13). For $E_{3body}\left(^6\mathrm{He}\right) = -1$ MeV, we get $\kappa \approx 0.22$ fm^{-1}. However, as discussed before, we found the value $\rho_0 = 0.45$ fm to be optimal for the valence part of the fully antisymmetrized wavefunction. Relating the two decay parameters as $\kappa = 1/(2\rho_0)$, $\rho_0 = 0.45$ fm would correspond to $\kappa = 1.11$ fm^{-1}, or $E_{3body} \approx -25$ MeV. In other words, individual valence terms in our microscopic wavefunction decay much faster than the expected asymptotic form of overlap (and three-body) functions. The asymptotical form should be most clearly realized for $K = 0$ s-waves thanks to a small, yet non-vanishing, centrifugal barrier in Eq. (2.12). In Figure 5.8, we plot again the three-body and overlap hyper-radial functions for $K = 0$ s-waves along with two asymptotical forms corresponding to decay scales $\kappa = 0.22$ fm^{-1} and $\rho_0 = 0.45$ fm. It is gratifying to see that the overlap function is almost perfect asymptotically in the computationally safe region of $\rho \lesssim 12$ fm. The right asymptotical trend is recovered regardless of the fact that all valence terms in the wavefunction are asymptotically wrong. These results have been obtained from the MN-SO wavefunction containing hyper-radial Laguerre polynomials of order five and less. Perhaps, if needed, the asymptotics could be improved further with inclusion of Laguerre polynomials of higher orders. In either case, presented results

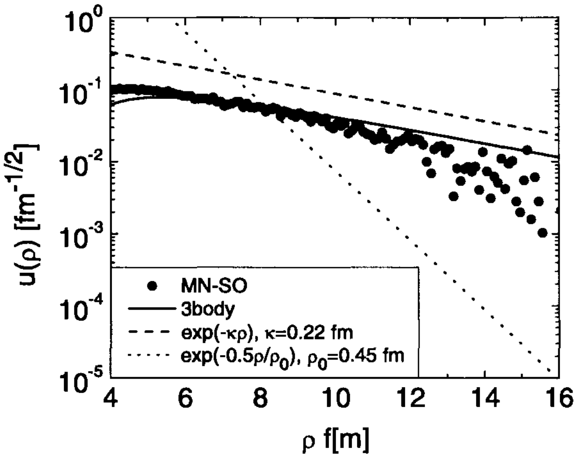

Figure 5.8: Behavior of $K = 0$ s-waves overlap and three-body functions from Figure 5.6 at large hyper-radii. Also shown are two different predictions for asymptotics, one corresponding to the three-body binding energy $E_{3body} = -1$ MeV ($\kappa = 0.22$ fm^{-1}) of ^{6}He, the other to the asymptotics of individual valence terms in the MN-SO wavefunction of ^{6}He ($\rho_0 = 0.45$ fm).

clearly demonstrate that the three-body hyper-spherical/hyper-radial basis is suitable not only for few-body, but also for microscopic calculations. The basis is flexible enough to catch simultaneously short- as well as long-distance correlations, a quality especially appreciable in the realm of Borromean halo systems. Based on these arguments, we believe that microscopic wavefunctions in MiCH have asymptotics very close to the proper one, indeed.

Using the analogy between overlap functions and three-body wavefunctions, we can also estimate relative probabilities of MN-SO overlap channels in the ^{4}He + n + n decomposition of ^{6}He. Because of the orthogonality of overlap channels, we can define such probability simply as a ratio of a spectroscopic factor and the value 1.3957, the sum of spectroscopic factors from the MN-SO model in Table 5.4. These probabilities are listed in Table 5.5 and they are very similar to the weights of corresponding channels in the three-body wavefunction of ^{6}He. Such a comparison is only approximate because the five overlap channels account for only 98.5% of the three-body wavefunction and overlap channels with spectroscopic factors smaller than about 0.01 were not extracted from the MN-SO ^{6}He. Nevertheless, mixing of overlap channels in both models is about the same.

Table 5.5: Probabilities of overlap channels from Table 5.4 in the ^{4}He + n + n decomposition of ^{6}He. Three-body probabilities are those from Table 2.1. MN-SO probabilities were computed as ratios of MN-SO spectroscopic factors from Table 5.4 and the value 1.3957 also from that table.

channel	probability [%]	
	3body	MN-SO
$K = 2$ s-waves	80.89	79.92
$K = 2$ p-waves	11.03	13.32
$K = 0$ s-waves	4.17	3.98
$K = 6$ d-waves	1.64	1.91
$K = 6$ f-waves	0.78	0.87

We now present two more comments regarding spectroscopic factors. Even though not mentioned so far, we also computed overlap functions from the MN model. Because the central nucleon-nucleon interaction does not mix valence spin-singlets and spin-triplets in the full microscopic wavefunction, overlap channels containing spin-triplets were absent in the MN model. At the same time, spectroscopic factors of the spin-singlet channels were about the same as those for the MN-SO model in Table 5.4. By not having spin-triplet overlap channels in the MN case, about 14% of spectroscopic strength resolved in the MN-SO case would be missing in MN. This potentially missing spectroscopic strength is estimated as a sum of MN-SO probabilities of spin-triplet channels in Table 5.5 and it represents one possible way to estimate the importance of non-central forces on the structure of ^{6}He.

Another comment regards the fact that the MN-SO spectroscopic factor for the dominant $K = 2$ s-waves overlap channel is larger than one in Table 5.4. This is expected [89] because in the overlap integral in Eq. (5.3), the α particle does not sit at the center of mass of ^{6}He. In other words, spectroscopic factors larger than one are there due to recoil effects. In [89], an upper limit on the spectroscopic factor of the dominant $K = 2$ s-waves channel was estimated to be about 25/16=1.5625 times the probability of this state in the shell-model. If we further assume that the probability in the shell-model can be approximated by the three-body model (as was in fact done in the cited work), then using Table 5.4 the upper limit on the spectroscopic factor of $K = 2$ s-waves channel would be 1.26, a value indeed larger than that extracted the MN-SO model. But the ratio of MN-SO and three-body spectroscopic factors in Table 5.4 varies between channels. This observation suggests that to account for microscopic information missing in the three-body model, it may not be sufficient to simply renormalize the entire three-body wavefunction by a common factor such as 25/16 suggested in [89].

Finally, overlap functions (also three-body wavefunctions) can be used to shed more light on clustering in ^{6}He. Additional insight is gained by calculating the probability of finding definite distances within the three-body decomposition of ^{6}He from Eq. (5.7):

$$P(r_{n-n}, r_{core-nn}) = r_{n-n}^2 r_{core-nn}^2 \int \left| (2/3)^{3/4} \sum_{\gamma_{val}} \mathcal{O}_{\gamma_{val}\,0^+} \mathscr{Y}_{\gamma_{val}\,0^+1-1} \right|^2 \mathrm{d}\Omega_x \, \mathrm{d}\Omega_y, \tag{5.10}$$

where r_{n-n} and $r_{core-nn}$ are the valence neutron-neutron separation and the distance between centers of masses of the core and the valence neutron pair, respectively. These distances would correspond to lengths of vectors $\vec{x}_1$ and $\vec{x}_2$ in the T Jacobi basis in Figure 2.1. The probability plot for the MN-SO ^{6}He is presented in Figure 5.9. The figure exhibits two peaks: a di-neutron-like peak positioned at about $r_{n-n} = 1.93$ fm and $r_{core-nn} = 2.63$ fm ($\rho = 3.33$ fm) with the two neutrons close together located outside ^{4}He, and a cigar-like peak at $r_{n-n} = 3.82$ fm and $r_{core-nn} = 1.03$ fm ($\rho = 2.95$ fm) with the two neutrons positioned on opposite sides of the core. Qualitatively the same clustering picture would be obtained within the three-body model and has also been reported from other models, such as SVM [133].

The occurrence of two prominent clustering peaks in Figure 5.9 is not surprising because the overlap channels are dominated in the T Jacobi basis by $K = 2$ s-waves. Using definitions from Figure 2.1, the distances r_{n-n} and $r_{core-nn}$ in ^{6}He are related to hyper-spherical coordinates as

$$r_{n-n} = \sqrt{2}\,\rho \sin\theta; \qquad r_{core-nn} = \sqrt{3/4}\,\rho \cos\theta. \tag{5.11}$$

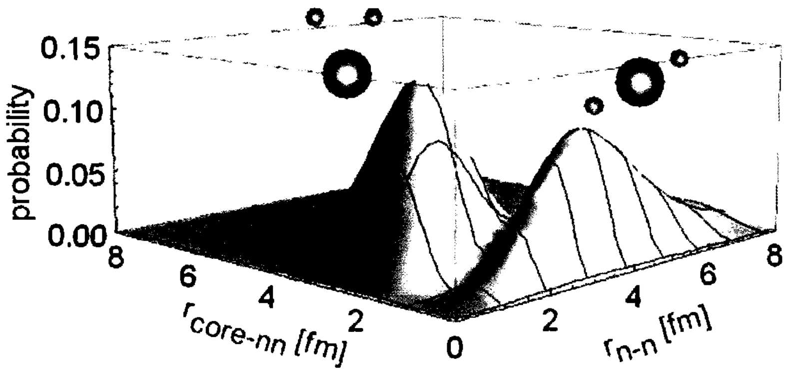

Figure 5.9: Correlation density plot for the ground state of the MN-SO ^{6}He. The dineutron and cigar-like configurations are shown schmetically.

Neglecting for a while the constant factors in Eq. (5.11), the hyper-angle serves as the polar angle in Figure 5.9, and the directional distribution of the clustering probability is given by the probability to find different hyper-angles. For $K = 2$ s-waves, the hyper-angular probability is shown in Figure 5.10. There are indeed two peaks in Figure 5.10 allowing the formation of two prominent peaks in Figure 5.9. Despite the symmetricity of the hyper-angular distribution in Figure 5.10, the clustering probability is not symmetrical due to mass factors in Eq. (5.11) and the influence of overlap channels other than $K = 2$ s-waves in the three-body decomposition of ^{6}He.

In summary, it becomes obvious that to appreciate the amount of details involved in few-body and microscopic models of ^{6}He, one should look beyond the few commonly studied features such as the three-body binding energy, nuclear radii and nucleon densities. At the level of wavefunctions, the differences between macroscopic and microscopic models are clear. To our knowledge, the overlap functions for ^{6}He have been extracted in this work for the first time from a microscopic structure model in a form that allows their direct comparison with few-body wavefunctions. By comparing our micrscopically derived overlap functions with three-body wavefunctions we concluded that a simple renormalization of three-body wavefunctions may not be sufficient to account properly for the microscopic information missing in few-body models. Besides their usefulness for a comparative study of different structure models, the overlap functions presented in this

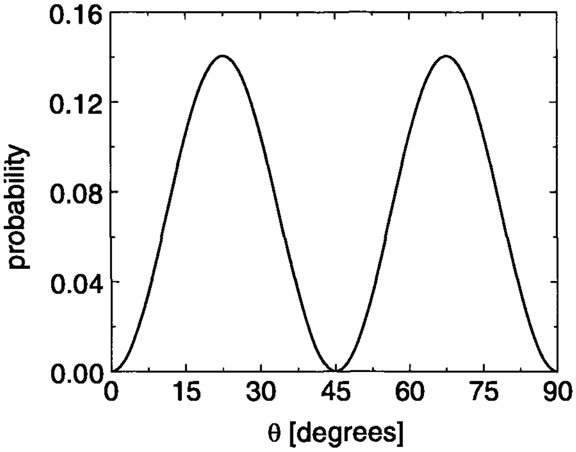

Figure 5.10: The probability to find different hyper-angles in the $K = 2$ s-waves overlap channel. For this channel, the hyper-angular probability is proportional to $P_1^{1/2,1/2}(\cos 2\theta)\sin^2\theta\cos^2\theta$ shown in the plot. The factor $\sin^2\theta\cos^2\theta$ is the hyper-angular part of the hyper-spherical volume element in Figure 2.1.

section provide a crucial input to reaction calculations involving ^{6}He, in particular, to two-neutron transfer reaction models.

5.4 Two-neutron transfer reactions

An immediate practical application of overlap functions obtained in the previous section is in reaction calculations involving ^{6}He. In particular, overlap functions enter directly in the formulation of two-nucleon transfer reactions. Several experiments have been performed to study the two-neutron transfer from ^{6}He onto hydrogen, helium, carbon, and copper targets [53,158–161]. Of those experiments, we concentrate on p(^{6}He,^{4}He)t with incident energy of ^{6}He 25 MeV/A [160], which is simpler to model due to the trivial structure of the target nucleus. This reaction was later reanalyzed in [89], where several possible drawbacks of the original analysis in [160] were indicated. It is clear from previous works that, for a given beam energy, the reaction mechanism contains both sequential and simultaneous transfers. In the former reaction mechanism, two neutrons are transferred one by one whereas in the later case they are transferred both at once as a pair. However, given that the sequential process involves the continuum and we do not yet have a fully microscopic description in that case, the comparative study here will focus only on the simultaneous transfer component, which is the only two-neutron transfer mode considered in previous works [89, 160].

Let us first analyze the transfer reaction p(^{6}He,^{4}He)t qualitatively. At the beam energy 25 MeV/A, the reaction happens well above the Coulomb barrier between proton and ^{6}He. Therefore, the neutron transfer can happen at any impact parameter. If the two neutrons are transfered in a single step as a pair, it is reasonable to expect that they are preferably picked from the di-neutron configuration in ^{6}He. Located almost entirely outside of ^{4}He, the di-neutron peak in Figure 5.9 reaches its maximum at a distance of about 2.6 fm between ^{4}He and the di-neutron. Given the radius 1.46 fm of ^{4}He, we then expect the reaction to be mostly peripheral relative to ^{4}He with small scattering angles in the reaction center-of-mass system. In terms of hyper-radii, peripherality of the reaction may be misleading, because the location of the di-neutron peak in Figure 5.9 corresponds to a fairly small hyper-radius of about 3.3 fm in Figure 5.6. Therefore, the transfer should be sensitive not only to distant tails of overlap functions in Figure 5.6, but also to their volume parts, or in other words to spectroscopic factors.

Quantitatively, the transfer reaction is analyzed within the distorted wave Born approximation (DWBA). Here, we briefly present the main ingredients of DWBA linking us to overlap functions; details can be found elsewhere [162]. Under the 1-step DWBA, the reaction amplitude for the simultaneous transfer of two neutrons in the p(^{6}He,^{4}He)t reaction can be written in prior form as (see for example Eq. (9) in [89]):

$$T^{\mathrm{DWBA}}_{\mathrm{prior}} = \left\langle \chi^{(-)}_{^4\mathrm{He-t}} \phi_{\mathrm{t}} \left| V^{\mathrm{p-(nn)}} + \delta V \right| \chi^{(+)}_{^6\mathrm{He-p}} \phi_{^6\mathrm{He}} \right\rangle , \tag{5.12}$$

where ϕ_{t} and $\phi_{^6\mathrm{He}}$ are overlaps between pairs of initial and final composite systems (t,p) and (^{4}He, ^{6}He), respectively. $\chi^{(+)}_{^6\mathrm{He-p}}$ and $\chi^{(-)}_{^4\mathrm{He-t}}$ are the distorted waves in the entrance ^{6}He-p and exit ^{4}He-t channels. The interaction causing the transition from the initial to the final state has two parts. The first part is the sum of potentials binding the two transferred neutrons to a proton: $V^{\mathrm{p-(nn)}} = V^{\mathrm{p-n_1}} + V^{\mathrm{p-n_2}}$. The other term δV, the so called remnant potential, contains potentials for a proton interacting with ^{4}He and ^{6}He: $\delta V = V^{^4\mathrm{He-p}} - U^{^6\mathrm{He-p}}$.

Traditionally, both overlaps ϕ_t and $\phi_{^6\mathrm{He}}$ would be taken as three-body wavefunctions of a triton and ^{6}He, an approach perfectly justified for the triton but arguable for ^{6}He. It is here where overlap functions from Section 5.3 obtained within MiCH enter the game: they are exactly $\phi_{^6\mathrm{He}}$. To examine the impact of the differences seen in Figure 5.6 between three-body wavefunctions and overlap functions on a physical observable, we calculate the reaction cross section for simultaneous two-neutron transfer between ^{6}He and a proton. Within DWBA and apart from additional constants, the differential cross-section is proportional to the square of the reaction amplitude from Eq. (5.12):

$$\frac{\mathrm{d}\sigma}{\mathrm{d}\Omega} \propto \left| T^{\mathrm{DWBA}}_{\mathrm{prior}} \right|^2 \tag{5.13}$$

All DWBA reaction calculations presented here are finite-range and have been performed with the code Fresco [163]. The triton three-body wavefunction ϕ_t and the binding potential $V^{^4\mathrm{He-p}}$ as well as optical potentials $U^{^6\mathrm{He-p}}$ and $U^{^4\mathrm{He-t}}$ are the same as in [89]. For consistency, the nucleon-nucleon interactions in $V^{\mathrm{p-(nn)}}$ are the same as those used to bind the triton [115]. For the optical potential between triton and ^{4}He in the exit channel, we adopted the parameter set I from Table I in [89], in which the potential was fitted to elastic scattering data, thus significantly reducing uncertainties in cross-sections. We have found the effects of the remnant potential to be large. Therefore, all presented cross-sections were obtained with the full complex remnant term included.

The cross-sections of simultaneous two-neutron transfer in the reaction p(^{6}He,^{4}He)t are finally shown in Figure 5.11. We considered two scenarios differing by treatment of the overlap $\phi_{^6\mathrm{He}}$: three-body, where the overlap was taken as the three-body wavefunction from Section 2.4, and MN-SO with the overlap replaced by microscopically founded overlap functions from the MN-SO model of ^{6}He in Section 5.3. We have found that the cross-sections are mostly sensitive to the components of $\phi_{^6\mathrm{He}}$ containing s-waves between the two neutrons, and between ^{4}He and the di-neutron. This sensitivity is expected

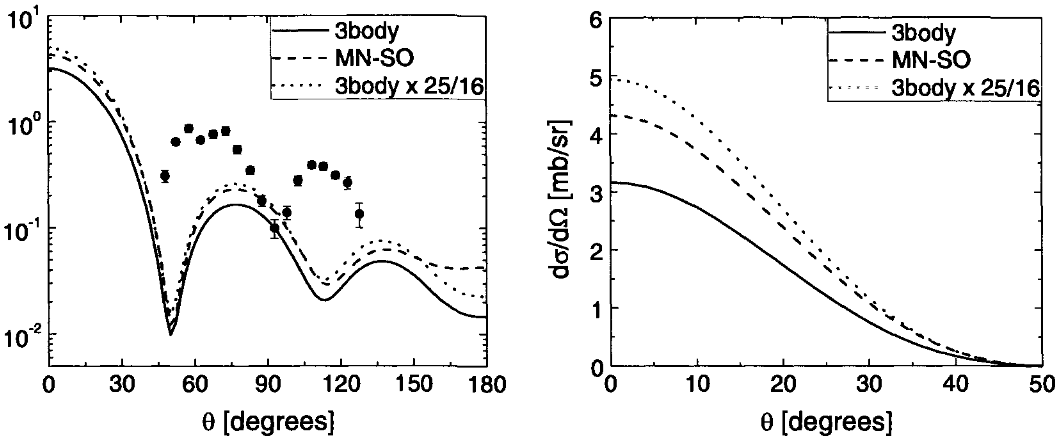

(a) Logarithmic scale. Points are experimental data from [160].

(b) Linear scale for small angles.

Figure 5.11: Cross-section of the p(^{6}He,^{4}He)t reaction at 25 MeV/A. Lines are theoretical results for the simultaneous two-neutron transfer process in the three-body, MN-SO and rescaled three-body model. See text for details.

because the reaction favors low momentum transfer. From the structure point of view, the major role of overlap channels containing s-waves is due to their dominance in the three-body ^{4}He + n + n decomposition of ^{6}He, as we have seen in Section 5.3.

At small angles, the ratio of the three-body and MN-SO cross-sections in Figure 5.11 is very close to the ratio of spectroscopic factors for $K = 2$ s-waves in Table 5.4, i.e. close to 1.38. This observation reflects our suspicion that the reaction at small angles is sensitive to almost the entire overlap functions from Figure 5.6. except perhaps at very small hyper-radii. Moreover, at small angles, the effects due to slightly different shapes of three-body and overlap functions are "integrated out", and the only thing that seems to matter is the difference in spectroscopic factors. For comparison, Figure 5.11 also contains the three-body cross-section renormalized by an additional spectroscopic factor $25/16 = 1.5625$ suggested in [89]. When one uses three-body wavefunctions in place of overlaps $\phi_{^6\text{He}}$, a simple additional renormalization of cross-sections is the only way to account for missing microscopic structure input. Observing the similar shapes of cross-sections in the three-body and MN-SO cases in Figure 5.11, one could try to argue in favor of such ad-hoc renormalization of three-body cross-sections. However, we have to realize that here we study only one reaction mechanism at a single energy; the cross-sections for other reactions and/or at different energies could be more sensitive to differences between three-body wavefunctions and microscopically derived overlap functions. Also, the three-body renormalization factor 25/16 is just an upper estimate based on a simple shell-model picture of ^{6}He. In either case, by using microscopically derived overlap functions, the cross-section is increased by about 40% compared to that obtained by using three-body wavefunctions, which by itself is significant given the quality of the experimental data in Figure 5.11.

Looking at Figure 5.11, one can see the disagreement between experimental data and theoretical calculations despite using microscopically derived overlap functions. It has been concluded in [89] that the disagreement most likely indicates the influence of other reaction channels not included in calculations, such as sequential transfer and/or ^{6}He break-up. Also, in the range of angles where the theory predicts a strong rise of the cross-section, there are no experimental data to guide the theory in the right direction.

Chapter 6

Summary and outlook

6.1 Summary

Halo nuclei are composite systems with prominent features of few-body correlations. The best examples of nuclear halo species are known to exist among light neutron-rich nuclei, in which a single or few neutrons may be partially decoupled from the rest of the system, from the core. The weak attraction to the core experienced by halo neutrons allows them to swim in distant, classically forbidden regions.

Particularly interesting are two-neutron halo nuclei, such as ^{6}He and ^{11}Li, with two correlated neutrons forming the halo. Typically, these nuclei are studied within few-body models, in which the long-distance inter-cluster motion is treated properly, but the inert-core picture used in such models is undoubtedly a simplification to the many-body problem. Nevertheless, few-body models supply the structure information for many reaction calculations involving two-neutron halo nuclei. On the other hand, microscopic models find halo species very challenging and these models may fail to capture the few-body long-distance correlations so important for halo nuclei.

At the heart of this dissertation is MiCH, a microscopic cluster model of two-neutron halo nuclei. Designing MiCH, the goal was to combine advantages of few-body and microscopic nuclear structure models to create a microscopic model capable to deal simultaneously with short- and long-range effects in two-neutron halo nuclei. To accomplish this goal, a properly antisymmetrized wavefunction in MiCH consists of a microscopic core-like piece and a three-body-like valence part expressed in terms of hyper-spherical functions. In the present work, MiCH has been applied to the ground state of the simplest two-neutron halo nucleus, ^{6}He, bound by the effective nucleon-nucleon Minnesota interaction. The results for this nucleus can be summarized as follows.

The Pauli principle is crucial for the binding and structure of ^{6}He, because it does not only eliminate forbidden states between the core and the valence neutrons and between the valence neutrons themselves, but it also delivers extra binding to the system through exchange effects. Through explicit antisymmetrization done in MiCH we have found, that the lowest hyper-spherical $K = 0$ three-body states are strongly blocked by the Pauli principle between the core and the valence neutrons. This observation is important especially in connection to three-body models, from which the hyper-spherical basis has been adopted,and which employ different methods to account approximately for the core-valence Pauli principle. The message here is that all three-body hyper-spherical states, but especially those with $K = 0$, ought to be subjected carefully to the Pauli principle if one is to describe ^{6}He realistically. It is through the core-valence exchange effects that the nucleus becomes three-body bound.

For a variationally optimized ^{6}He, the binding energy relative to the three-body threshold, rms radii, the thickness of the neutron halo, and nucleon densities were computed and found to agree with experimental values and results obtained in a variety of structure models. The halo nature of the nucleus can be seen from its extended neutron density resulting in the large difference between the matter and proton radius. It seems that commonly computed and highly integrated observables such the three-body binding energy and radii may not appreciate the amount of details built into different models of ^{6}He. For these observables, a three-body approach with its simplistic description of the ^{4}He core is as reliable as microscopic models.

To extract information about the ^{4}He + n + n component in ^{6}He, we have computed the overlap integral between ^{6}He and ^{4}He. The integral was expanded in hyper-spherical functions to make it comparable with three-body wavefunctions and applicable to reaction calculations involving ^{6}He. To our knowledge, this is the first time that overlap functions for ^{6}He have been calculated in this form from a microscopic structure model. In agreement with three-body models, the microscopically founded three-body decomposition from MiCH suggests that the same overlap channels dominate the ^{4}He + n + n cluster-division in ^{6}He. On the other hand, MiCH predicts spectroscopic factors larger by at least 30% than those from a three-body model for the dominant overlap channels in ^{6}He. This difference in spectroscopic factors reveals a deficiency of few-body models, namely the inert-core approximation. Moreover, the relative enhancement of spectroscopic factors in MiCH varies between overlap channels, and so it may not be sufficient in three-body models to simply renormalize the wavefunction to account for missing microscopic information. In agreement with other models, we predict two major clusterization patterns in ^{6}He: the di-neutron-like and the cigar-like. In the former pattern, two neutrons stay close together outside the ^{4}He core, in the later pattern, two neutrons are positioned on opposite sides of the core.

Finally, as a practical application of overlap functions obtained in MiCH, we carried out a calculation for the reaction p(^{6}He,^{4}He)t at 25 MeV/A assuming that the reaction proceeds only through the simultaneous transfer of two neutrons. The angular distribution of the reaction cross-section is similar to that obtained with three-body wavefunctions for ^{6}He, but the cross-section with microscopically derived overlap functions is larger by about 40% due to the above-mentioned difference in spectroscopic factors between MiCH and three-body models. Even with microscopically derived input for this reaction about the ^{4}He + n + n component in ^{6}He, theoretical predictions for the cross-section assuming only the simultaneous two-neutron transfer do not reproduce experimental data. Therefore, we assert that other reaction mechanisms such as sequential transfer and break-up should be included in theoretical considerations for this reaction.

6.2 Outlook

In the present work, the model MiCH has been formulated for bound states of two-neutron halo nuclei and applied to the simplest case, ^{6}He, bound by an effective soft-core nucleon-nucleon interaction. For this nucleus, the model has proved to be working and the original goal of combining advantages of few-body and microscopic models to describe simultaneously the short-distance and the long-distance few-body halo correlations in ^{6}He have been met. This success opens the door to possible future applications and improvements of the model.

Even for ^{6}He, there is still work to be done. An interesting application aimed on the halo aspects would be the β-decay of ^{6}He to ^{6}Li. There is experimental evidence that the decay takes place essentially in the halo region in ^{6}He. For such a study, a microscopic wavefunction for ^{6}Li is needed and we could attempt to produce it within MiCH despite the fact that the ground state of ^{6}Li does not have a Borromean character. ^{6}Li would be modelled as ^{4}He + n + p with a microscopic ^{4}He core.

The most exciting case to study among two-neutron halo nuclei is ^{11}Li. This nucleus has a very small two-neutron separation energy and a well developed neutron halo. As part of the present work, ^{11}Li has been studied within a deformed-core three-body model, and it has been found that the core deformation plays an important role in the structure of this nucleus. Given the physics insight built into MiCH, the model is well suited to face the challenge of the unique neutron halo in ^{11}Li. Going to mass eleven, however, we would most likely encounter (serious) computational difficulties due to the memory and CPU time required to carry out the Monte Carlo integration of matrix elements. We believe that with the increasing computational power, improved algorithms and code parallelization, this computational difficulty could be overcome which would bring ^{11}Li to our grasp.

A further improvement of the model could be achieved by the implementation of more realistic nucleon-nucleon interactions and the inclusion of excited states. For light two-neutron halo nuclei, including excited states means extension to the continuum, which is important for reaction calculations involving these nuclei due to the proximity of break-up thresholds. This brings us to the interplay between the structure and reactions.

In the present work, we have studied a two-neutron transfer reaction involving ^{6}He in the approximation of simultaneous transfer. Our results and those of other works suggest that the experimental transfer data can not be reproduced unless other reaction channels, such as sequential transfer and break-up, are included in the calculation. These other channels involve continuum states of ^{6}He as well as of ^{5}He. Our long-term goal is to describe transfer reactions involving two-neutron halo nuclei in their full complexity with a microscopically derived structure input for all nuclei involved in the reaction. This task is important because it is at the intersection between nuclear structure and reactions, where we have learnt most about two-neutron halo nuclei.

Finally, MiCH could be extended to study other light nuclei with less-straightforward cluster divisions, but still showing few-body features. Among them are ^{8}He with its neutron-skin and ^{12}C with its famous Hoyle state. For ^{8}He (= ^{4}He + n + n + n + n), the hyper-spherical formalism in MiCH adopted from few-body models would be extended to deal with the five-body inter-cluster motion, and for ^{12}C (= ^{4}He + ^{4}He + ^{4}He), the two valence neutrons in the current version of MiCH would be replaced by two microscopic ^{4}He clusters. In both nuclei, all binary subsystems are unbound which makes MiCH well suited to deal with such nuclei.

Appendix A

Implementation details

Along a random walk, local values of matrix elements in the spin-isospin space are computed many times. This is done not only at each integration point, where local values of operators such as O_{loc} in Eq. (4.22) and local weights such as w in Eq. (4.25) are evaluated, but also at each trial move proposed by the Metropolis algorithm, where a local value of importance function needs to be calculated. In either case, the first thing we need is a local representation of the wavefunction in Eq. (4.3).

A.1 Local representation of wavefunction

The concise coupled form of the wavefunction in Chapter 4 is not suitable for local manipulations. The reason is at least twofold. First, the angular momentum couplings hide projections of orbital momenta along Jacobi coordinates, which are needed to evaluate the spatial part of the wavefunction locally. Second, operators such as Hamiltonian contain pair-wise (between two spots) operators acting on spin and isospin degrees of freedom in the wavefunction, and so one must be able to identify spin-isospin "values" of each spot. A convenient basis of spin/-sospin states is provided by those sets in which each spot has a definite third components of spin and isospin [140]. Therefore, at any set of spots $\vec{r} = \{\vec{r}_1, \ldots, \vec{r}_A\}$, angular momentum couplings in the wavefunction are decoupled so that third components of orbital momenta along Jacobi coordinates and those of single-spot spins and isospins can be identified. The difference between spots and particles has been explained in Section 3.1.

In the system with A spots (particles), there are 2^A possible permutations of spin projections over spots. To represent a single spin in the computer, 0 is used for spin "down" and 1 for spin "up". Each spin basis state in the wavefunction can then be represented in a simple binary fashion. For example, for 4 particles we have:

spots	→	1	2	3	4	
binary bits	→	3	2	1	0	binary #
		0	0	0	0	0
		0	0	0	1	1
		0	0	1	0	2
			⋮	⋮		⋮
		1	1	1	1	15

This basis only keeps a record of how spin projections are distributed over spots. Under particle permutations imposed by $\mathcal{A}^{val}$ and $\mathcal{A}^{core-val}$ antisymmetrizers in Eq. (4.3), particles carrying spins jump between spots, but once the antisymmetrization of the wavefunction has been completed, the only thing one needs to know is whether there is a spin up or down at a given spot regardless of which particle brought it in.

The isospins can be handled similarly, but due to charge conservation, the number of isospin basis states can be reduced to:

$$\binom{A}{Z},$$

where Z is the number of protons. The number of isospin basis states could be reduced further by constructing states with good total isospin, but then the action of isospin-related operators would be more involved.

After spatial parts of the wavefunction have been evaluated for each particle permutation, all pieces of the antisymmetrized wavefunction belonging to a given spin-isospin basis state are gathered. Ultimately, the wavefunction is represented locally as a two dimensional array of complex numbers with elements corresponding to different spin-isospin basis states.

A.2 Operators

In the spin-isospin basis described in the previous section, the Hamiltonian containing two-nucleon interactions is a sparse matrix, since two-body interactions can only change the spins or isospins of two nucleons at a time. Any operator involving spins or isospins is written in the form in which it acts directly on spin or isospin projections. Under the action of such an operator, spin-isospin projections at some spots may be changed, and the spin-isospin basis states are transformed among themselves. Spin-dependent operators include for example interaction terms, the spin-orbit force, operators S^2 and S_z of the total spin and J^2 and J_z of the total angular momentum.

At the level of individual spots, a single spin operator $\vec{s} = \frac{1}{2}\vec{\sigma}$ is expressed in terms of raising s^+, lowering s^- and σ_z operators:

$$s_x = \frac{1}{2}\sigma_x = \frac{s^+ + s^-}{2}, \qquad s_y = \frac{1}{2}\sigma_y = \frac{s^+ - s^-}{2i}, \qquad s_z = \frac{1}{2}\sigma_z. \tag{A.1}$$

When permitted, the z-projection of a single spin is raised and lowered upon the action of s^+ and s^-, respectively. The spin projection is not changed by σ_z, but an extra factor (-1) is acquired when the spin is down. An equivalent treatment is given to a single isospin operator $\vec{t} = \frac{1}{2}\vec{\tau}$. The interaction spin-exchange operator P^σ_{ij} in Eq. (3.11) simply swaps spin projections at spots i and j. The coordinate-exchange operator P^x_{ij} in Eq. (3.11) is written as $P^x_{ij} = (-1)P^\sigma_{ij}P^\tau_{ij}$, where the isospin-exchange operator P^τ_{ij} swaps isospin projections at spots i and j. Sometimes, the central part of a two-nucleon interaction is written in a form containing $\sigma_i \cdot \sigma_j$ and $\tau_i \cdot \tau_j$ operators instead of P^σ_{ij} and P^τ_{ij}. These operators can be written as:

$$\sigma_i \cdot \sigma_j = 2P^\sigma_{ij} - 1, \qquad \tau_i \cdot \tau_j = 2P^\tau_{ij} - 1. \tag{A.2}$$

Momentum-dependent operators, such as the kinetic energy, the spin-orbit force, operators L_z and L^2 of the total orbital momentum and operators J_z, J^2 of the total angular momentum, involve first- and second-order derivatives of the wavefunction. All required derivatives are obtained simply by moving each spot by a small distance in both the positive and negative directions along each axis. If, for brevity, we consider a function $f(x, y)$ of two variables x and y, then its partial first- and second-order derivatives may approximately be obtained from:

$$
\begin{aligned}
f'_x &= \frac{f(x+\Delta, y) - f(x-\Delta, y)}{2\Delta}, && \text{(A.3)}\\
f''_{xx} &= \frac{f(x+\Delta, y) + f(x-\Delta, y) - 2f(x, y)}{\Delta^2}, && \text{(A.4)}\\
f''_{xy} &= \frac{f(x+\Delta, y+\Delta) + f(x-\Delta, y-\Delta) - 2f(x, y)}{\Delta^2} - f''_{xx} - f''_{yy}, && \text{(A.5)}
\end{aligned}
$$

where Δ represents a small shift and the subscripts on f denote differentiating variables. First- and second-order derivatives with respect to y would be obtained by making a small shift in y instead of x. The dependence of derivatives on Δ must be tested carefully to ensure their reliability. There should exist an interval of optimal values of Δ within which the approximations to derivatives are Δ-independent. In MiCH, the value $\Delta = 0.001$ fm is used.

To obtain first- and second-order derivatives of the wavefunction in MiCH, Eq. (A.3)–Eq. (A.5) are applied to each spot in each x, y, z direction which requires $2 \times 3 \times A$ additional evaluations of the wavefunction. This is the reason why, from the computational point of view, short but well decorrelated random walks may be much cheaper to work with than long but highly correlated walks. Remember that when integration points are being decorrelated, a single new evaluation of the wavefunction at $\vec{r}_{trial}$ is needed in each decorrleation step to check the Metropolis acceptance condition.

Appendix B

Further tests

For a success of any variational calculation in the framework of VMC, the reliability and accuracy of matrix element evaluation are crucial. In Section 4.2.2, the Metropolis algorithm has been checked for reliability, issues related to correlations inherent in the algorithm were pointed out and methods of their suppression were outlined. In this Appendix, additional tests are presented to convince ourselves that numerical manipulations and integrations in MiCH are carried out properly. Also, the problem of "bad points" first mentioned in Section 4.2.3 is discussed

B.1 Triton tests and the story of bad points

This section summarizes some numerical results obtained within MiCH for the simplest core + n + n bound nuclear system, the triton. In triton, the wavefunction in Eq. (4.3) does not need to be core-valence antisymmetrized, because the core contains a single proton distinguishable (by its isospin projection) from valence neutrons and there are no core-valence forbidden states. This makes the triton a perfect case to check the implementation of the valence part of the wavefunction in Eq. (4.3).

We start with a triton containing a single valence term in the T Jacobi basis characterized by $\{K, l_x, l_y, L, S, J_{val}, n_{lag}\}$ and ρ_0 from Section 2.1. By using the definition of a local value of an operator from Eq. (4.22) and after applying the kinetic energy operator from the left-hand side of Eq. (2.4) on triton's wavefunction Ψ from Eq. (4.3), the local kinetic energy can be written as:

$$
\begin{aligned}
&T_{loc}(\vec{r}) = \\
&\frac{\langle\Psi|T|\Psi\rangle_{s,t}}{\langle\Psi|\Psi\rangle_{s,t}} = \frac{\hbar^2}{2m}\frac{1}{\rho^2 L^5_{n_{lag}}} \\
&\left[\left(-\frac{15}{4}+\frac{5}{2}\frac{\rho}{\rho_0}-\frac{1}{4}\left(\frac{\rho}{\rho_0}\right)^2\right) L^5_{n_{lag}} + \left(5\frac{\rho}{\rho_0}-\left(\frac{\rho}{\rho_0}\right)^2\right) L^6_{n_{lag}-1} - \left(\frac{\rho}{\rho_0}\right)^2 L^7_{n_{lag}-2}\right] \\
&+\frac{\hbar^2}{2m}\frac{(K+3/2)(K+5/2)}{\rho^2} \qquad \text{(B.1)}
\end{aligned}
$$

with indexes on Ψ omitted. Here, all $L_l^k(\rho/\rho_0)$ are associated Laguerre polynomials having the following explicit form taken from the relationship 22.3.9 in [97]:

$$
L_l^k((x) = \sum_{m=0}^{k} (-1)^m \binom{n+k}{n-m} \frac{1}{m!} x^m, \qquad l \geq 0,\, k \geq 0. \qquad \text{(B.2)}
$$

By definition, we set $L^k_{-1} = L^k_{-2} \equiv 0$. For small hyper-radii, the local kinetic energy diverges as:

$$
K = 0, \text{any } n_{lag}: \qquad T_{loc}(\rho \to 0) \approx \left(1 + n_{lag}/3\right)/\rho, \qquad \text{(B.3)}
$$

$$
K \neq 0, \text{any } n_{lag}: \qquad T_{loc}(\rho \to 0) \approx K(K+4)/\rho^2, \qquad \text{(B.4)}
$$

where the advantage was taken of the limiting form of Eq. (B.2). Furthermore, hyper-radii in the triton are distributed according to:

$$
P(\rho) = \rho^5 \left(\mathcal{R}_{n_{lag}}\right)^2, \qquad \text{(B.5)}
$$

where $\mathcal{R}_{n_{lag}}$ is a hyper-radial basis function from Eq. (2.16) and ρ^5 is the phase-factor from the hyper-spherical volume element in Figure 2.1. By using Eq. (B.2), the hyper-radial probability at small hyper-radii is:

$$P(\rho \to 0) \approx \frac{(n_{lag}+5)!}{(n_{lag})!}\rho^5, \tag{B.6}$$

and it increases with the fifth power of n_{lag}. At small hyper-radii, however, the local kinetic energy in Eq. (B.3) and Eq. (B.4) diverges. Therefore, valence terms with higher n_{lag} may trigger "bad points", i.e. integration points with extraordinarily large local kinetic energies. When that happens, the Monte Carlo energy averaging is harder to converge.

To illustrate the effect of bad points, we consider a triton containing a single valence term in the T Jacobi basis with $l_x = l_y = L = S = 0$ and $\rho_0 = 0.50$ fm. For the hyper-spherical part of the wavefunction, two scenarios are considered: $K = 0$, $n_{lag} = 0$ and $K = 4$, $n_{lag} = 2$. The former case represents spatially the simplest possible triton, whereas the later case contains non-trivial hyper-angular and hyper-radial parts. For each of these tritons, a random walk is produced and the local kinetic energies and the distribution of hyper-radii are shown in Figure B.1.

In the figure, our suspicion about bad points is clearly confirmed. Compared to the hyper-radial distribution for the triton with $K = 0$, $n_{lag} = 0$ in Figure B.1(e), hyper-radii for the triton with $K = 4$, $n_{lag} = 2$ in Figure B.1(f) are shifted towards smaller values and their probability grows rapidly near the origin, which gives birth to very large local kinetic energies in Figure B.1(b) and Figure B.1(d) for that triton. Even though the number of bad points is small, once they occur, they severely bias the Monte Carlo estimate of the triton's kinetic energy, sometimes making the estimate completely unreliable. A similar effect has been observed in a fully antisymmetrized ^{6}He, where inclusion of valence terms with higher n_{lag} may trigger bad points, especially when there are only a few valence terms in the wavefunction. In ^{6}He, bad points may occur if any two spots and the center-of-mass of remaining spots are close to each other. Then, in some core-valence permutations, the valence part of the wavefunction is susceptible to large local kinetic energies. Therefore, valence terms with $n_{lag} \neq 0$ should be added to the model space

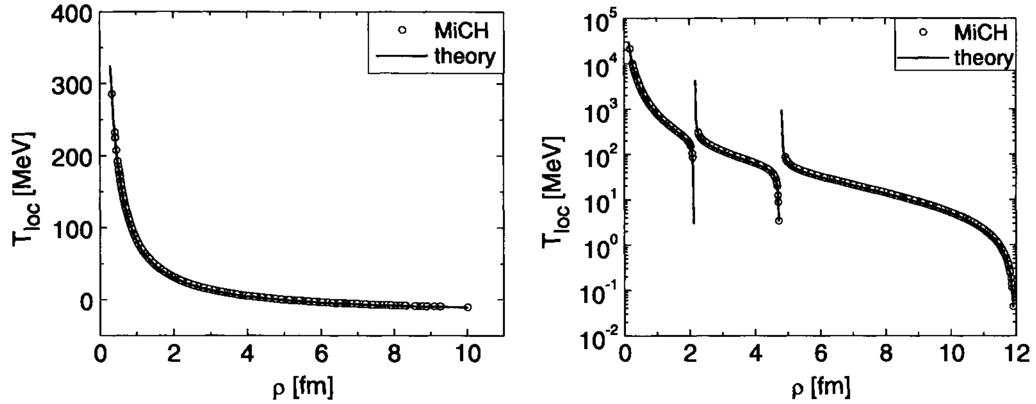

(a) Triton with $K = 0$, $n_{lag} = 0$. Dependence of local kinetic energies on the hyper-radius.

(b) Triton with $K = 4$, $n_{lag} = 2$. Dependence of local kinetic energies on the hyper-radius.

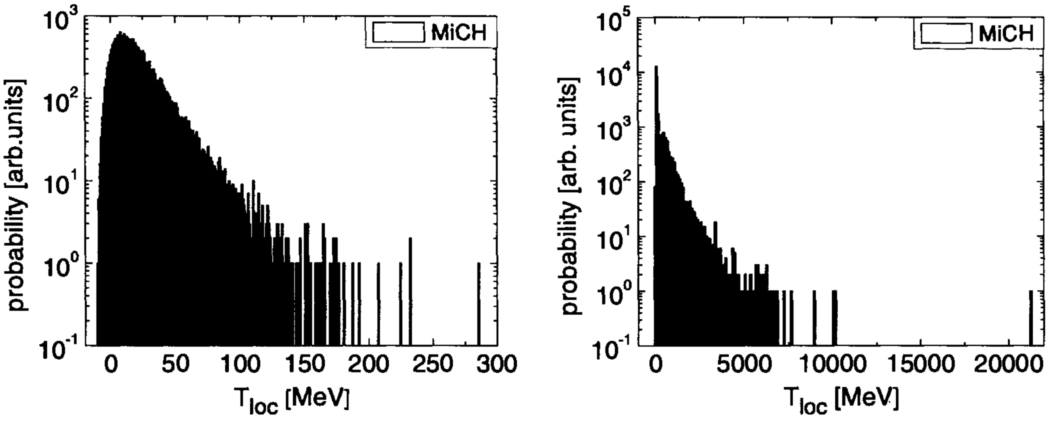

(c) Triton with $K = 0$, $n_{lag} = 0$. Distribution of local kinetic energies.

(d) Triton with $K = 4$, $n_{lag} = 2$. Distribution of local kinetic energies.

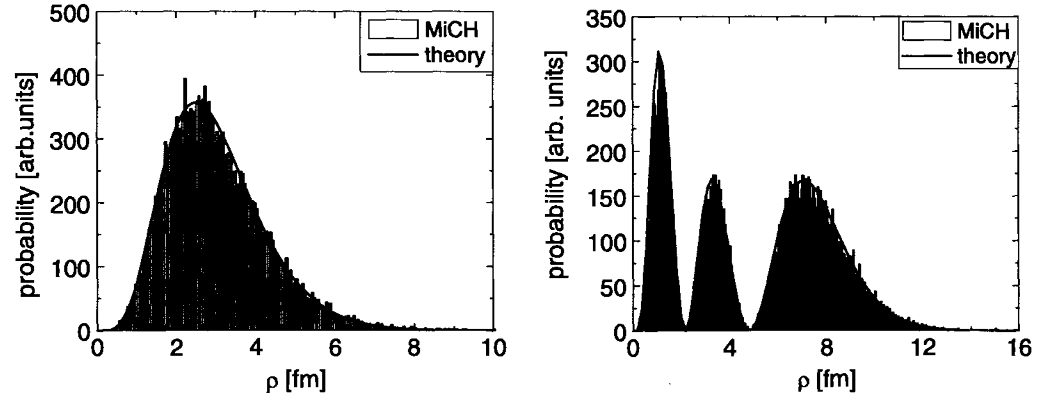

(e) Triton with $K = 0$, $n_{lag} = 0$. Distribution of hyper-radii.

(f) Triton with $K = 4$, $n_{lag} = 2$. Distribution of hyper-radii.

Figure B.1: Local kinetic energies, their distribution, and the distribution of hyper-radii for simple tritons with single $K = 0$, $n_{lag} = 0$ and $K = 4$, $n_{lag} = 2$ hyper-spherical channels.. Theoretical curves correspond to Eq. (B.1) for kinetic energy and Eq. (B.5) for the hyper-radial probability.

of ^{6}He only after a preliminary convergence in hyper-momentum has been reached for $n_{lag} = 0$.

It is gratifying to see that the theoretical predictions from Eq. (B.1) and Eq. (B.5) are perfectly reproduced by MiCH in Figure B.1. Finally, local kinetic energies can be negative, as can be seen from Figure B.1(a) for the triton with $K = 0$, $n_{lag} = 0$. When the wavefunction contains more valence terms, local kinetic energy can take negative values even for small hyper-radii due to interference effects.

To put MiCH to a further test, we now try to reproduce basic observables of an auxiliary triton produced within the three-body model described in Chapter 2. For this purpose, we use the three-body code FaCE [93] to generate the wavefunction of a triton within a limited model space containing all valence terms in the T Jacobi basis with $K \leq K_{max}$, $n_{lag} \leq 10$ and $\rho_0 = 0.50$ fm. The nucleus is bound by the Volkov I interaction with the mixing parameter set to $m = 0.0$ [135]:

$$V_{ij} = -83.34 \exp\left[-(r_{ij}/1.60)^2\right] + 144.83 \exp\left[-(r_{ij}/0.82)^2\right] \tag{B.7}$$

where $r_{ij} = |\vec{r}_i - \vec{r}_j|$ is the distance between nucleons i and j. For several values of K_{max}, the binding energy and the rms radius of a triton produced by FaCE are estimated by MiCH. The results are shown in Figure B.2. The binding energy of the triton predicted by the three-body model is perfectly reproduced numerically by MiCH in Figure B.2(a). For rms matter radii, there is a slight discrepancy ($\lesssim 1\%$) between the three-body and MiCH values in Figure B.2(b). Even in the three-body calculations, some integrals are carried out numerically with no error estimates provided. Therefore, the origin of the mentioned discrepancy remains unknown. The actual difference between three-body and our values may be beyond the accuracy of three-body calculations.

In summary, passing these triton and other tests, we have convinced ourselves that the valence part of the wavefunction is implemented properly in MiCH. It is the valence part of the wavefunction that is responsible for bad points plaguing Monte Carlo estimates of matrix elements.

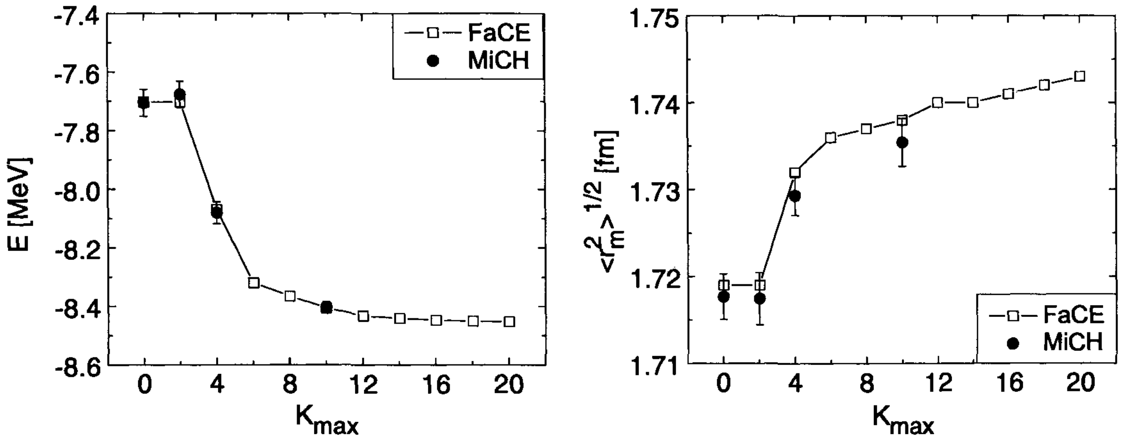

(a) Binding energy.

(b) Rms matter radius.

Figure B.2: The binding energy and the rms matter radius of a triton bound by the Volkov I nucleon-nucleon interaction ($m = 0$). Empty squares are values calculated by the three-body code FaCE. For $K_{max} = 0$, 2, 4 and 10, the observables are estimated by MiCH using wavefunctions produced by FaCE. Each value shown for MiCH is the average value from eight independent random walks each containing 100,000 integration points.

B.2 Additional tests and checks

Here, we briefly comment on some other tests of the accuracy of calculations in MiCH:

- For any wavefunction for the core produced within SVM as described in Chapter 3, the binding energy is also estimated in MiCH by simply switching off the valence part in Eq. (4.3). Our numerical estimates of the binding energy of the ^{4}He core are always in perfect agreement with values predicted by SVM.

- Occasionally, local values of the kinetic energy of the total center of mass are computed at several integration points. Typically, the values for ^{6}He are of the order of 10^{-7} MeV, i.e. at the level of numerical noise.

- At the beginning of each random walk, local values of the total orbital momentum $\vec{L} = \sum_{i=1}^{A} \vec{l}_i$ and $\vec{L}^2$, total spin $\vec{S} = \sum_{i=1}^{A} \vec{s}_i$ and $\vec{S}^2$, and total angular momentum $\vec{J} = \vec{L} + \vec{S}$ and $\vec{J}^2$ are computed at a single integration point. Among them, only local values of J_z and $\vec{J}^2$ are conserved. In ^{6}He bound by central nucleon-nucleon interactions, the core has $L = S = J = 0$ and the same is true for the valence part.

Then all operators have definite eigenvalues equal to 0. In such a case, typical local values of operators are:

operator	local value	
	real part	imaginary part
L_x	-1.781E-16	-2.079E-07
L_y	-2.664E-16	-2.282E-07
L_z	2.559E-16	-1.273E-07
L^2	1.300E-06	1.521E-11
S_x	0.000E+00	0.000E+00
S_y	0.000E+00	0.000E+00
S_z	0.000E+00	0.000E+00
S^2	5.099E-31	-4.902E-51
J_x	-1.781E-16	-2.079E-07
J_y	-2.664E-16	-2.282E-07
J_z	2.559E-16	-1.273E-07
J^2	1.300E-06	1.521E-11

Thus, all expected values are reproduced up to a numerical noise.

- Also, at the beginning of each walk, the antisymmetry of the wavefunction is checked at a single integration point. A properly antisymmetrized wavefunction Ψ changes its phase by (-1) when two particles are permuted under the action of the permutation operator P. Therefore, the sum $\Psi + P\Psi$ must vanish for any P. Again, this is confirmed numerically up to numerical noise.

Appendix C

Comparative optimization on two independent random walks

This Appendix presents the details of the improved optimization method employed for ^{6}He bound by central and non-central spin-orbit nucleon-nucleon interactions. The method has been developed to circumvent numerical instabilities encountered for such a ^{6}He due to the mixing of spin-singlet and spin-triplet valence terms in the wavefunction, as mentioned in Section 4.2.3. The idea behind the method is to attenuate the effects of statistical noise in the computation of overlap and energy matrix elements by comparing results obtained on two independent random walks. In this section, energy means the binding energy of ^{6}He.

Let us suppose that somewhere along the optimization route, we have produced a new best guess for the "stable" wavefunction containing "stable" valence terms. Two independent "reference" (random) walks are produced for this wavefunction and the reference energy of ^{6}He is estimated on each of them. Then, several (many) "trial" valence terms are temporarily added to the stable wavefunction. Such a temporary wavefunction is called a "trial" wavefunction. Normally, trial terms include all valence terms absent among the stable terms up to some maximum values of the hyper-momentum K and the order of hyper-radial valence functions n_{lag}. Actually, two identical trial wavefunctions (called trial wavefunctions) are created, each linked to one reference walk. For a given trial wavefunction, all computations will be done on the reference walk attached to it. In the following, energies are determined via the energy matrix diagonalization in correlated sampling on reference walks. "A gain" is a difference between energy and the reference energy. Trial terms are thinned out as follows:

1. Estimate the gain for each trial wavefunction. Except pathological situations, these gains represent the maximum possible gains due to all trial terms.

2. On each reference walk, determine gains for all possible wavefunctions containing "all stable + single trial" terms. A trial term is removed from a trial wavefunction if its gain is positive, or is small in absolute value relative to the maximum possible gain from step 1.

3. Compare trial terms outstanding in both trial wavefunctions and remove those terms not present in both wavefunctions. This condition is highly selective.

4. On each reference walk, compute "cumulative" gains due to a singlet, doublet, triplet, ... of remaining trial terms with largest (in absolute value) individual gains from step 2. Due to interference effects, a cumulative gain is not equal to a sum of individual gains from step 2. A trial term is removed whenever its addition makes the cumulative gain increase by more than a factor 2–3 compared to its individual gain from step 2; large contribution to the cumulative gain could be an interference effect or a numerical instability, two effects hard to disentangle.

5. Apply point 3 again on remaining trial terms.

6. At this point, there should be only few ($\lesssim 10$) trial terms left and they are the same in both trial wavefunctions. The number of remaining trial terms is controlled by restrictions in steps 2 and 4. On each reference walk, find a trial term lowering the energy the most, a pair of trial terms lowering the energy the most among all pairs of trial terms, and so on for triplets, quadruplets, etc. When taken as absolute values, the gain due to the most contributing singlet, doublet, ... of trial terms is an

increasing function. The combination of trial terms for which the gain (in absolute value) begins to saturate can be finally accepted to the stable wavefunction. The selected final combination of trial terms must be the same on both reference walks, though, which is normally true; when it is not true, all trial terms remaining after step 5 can simply be accepted because they are guaranteed to be the same on both reference walks. If the number of trial terms about to be admitted to the stable wavefunction is too high, we restrict the pool of remaining trial terms by imposing stricter conditions in steps 2 and 4.

   Note that up to this point, we are only concerned about energy eigenvalues, which are numerically stable.

7. In the previous step, a winning set of several trial terms has been found. These trial terms came as winners on two independent reference walks. Therefore, their selection should be barely affected by possible numerical instabilities in the computation of overlap and energy matrix elements and the energy matrix diagonalization. The final energy matrix diagonalization for the system containing all stable + selected trial terms provides numerically stable lowest eigenvalues and eigenvectors of linear expansion coefficients in the wavefunction. The winning set of trial terms can be safely accepted to the family of stable terms and a new stable wavefunction is thus obtained.

   However, the eigenenergies and eigenvectors in the last mentioned diagonalization will most certainly differ on the two reference walks, which implies that two new stable wavefunctions are actually produced. The final check involves cross-correlated runs, in which energy of a new stable wavefunction obtained on one reference walk is computed in correlated sampling on the other reference walk and vice versa. If everything is OK, linear coefficients in the two new stable wavefunctions can be averaged coefficient by coefficient and the final new stable wavefunction is constructed by using the averaged linear coefficients.

As described in Section 4.2.3, several optimization cycles can be executed on the same pair of reference walks. It needs to be emphasized that any failed trial valence term from one cycle will appear on the list of trial terms in any subsequent cycle. Again, it is wise to first build a wavefunction with several $n_{lag} = 0$ terms before higher-order Laguerre polynomials are considered as trial terms. As optimization process progresses, the pool of trial terms is broadened by an addition of terms with higher hyper-momentum and n_{lag}. The optimization continues until the convergence in the binding energy is reached.

In the present work, the non-linear parameter ρ_0 is the same in all valence terms. The optimization procedure described above assumes a constant value of ρ_0. Therefore, the optimal value of the non-linear parameter corresponding to the energy minimum still needs to be found. An attempt to localize the global energy minimum by simply changing the non-linear parameter in the converged wavefunction (accompanied by the energy matrix rediagonalization) is doomed to fail. Such search would point to a fake energy minimum formed at or close to the value of ρ_0, for which the wavefunction was originally constructed. This is because due to the competitive selection, many valence terms have not been admitted to the wavefunction, which makes the converged wavefunction firmly tailored to a given non-linear parameter. This is to be compared with the case of central forces, where all possible valence terms up to maximum values of K and n_{lag} are present in any converged wavefunction, as explained in Section 4.2.3. To localize the global energy minimum, we have to use a wavefunction containing all possible valence terms present and absent in the originally optimized wavefunction. Once the global energy minimum is found, the entire optimization process outlined above must be repeated for the optimum value of ρ_0.

Appendix D

Wavefunction normalization

In this Appendix, we discuss how to calculate the normalization of the ^{6}He wavefunction. In the present work, the normalization of ^{6}He is needed to compute the overlap integral between ^{4}He and ^{6}He in Section 5.3 in a meaningful way.

We rely on the Monte Carlo formalism developed in Section 4.2.1 and assume that the wavefunction of a nucleus depends on all spatial, spin and isospin degrees of freedom, i.e. $\Psi = \Psi(\vec{r}, s, t)$. By using the Monte Carlo estimator from Eq. (4.14), the norm of the wavefunction can be estimated as:

$$\langle \Psi | \Psi \rangle \approx \frac{1}{N} \sum_{n=1}^{N} w(\vec{r}^{(n)}), \tag{D.1}$$

where w is a local weight:

$$w(\vec{r}^{(n)}) = \frac{\langle \Psi | \Psi \rangle_{s,t}}{p(\vec{r}^{(n)})}. \tag{D.2}$$

The sampling function $p(\vec{r})$ satisfies Eq. (4.10) and can be chosen as a square of an auxiliary sampling wavefunction $\Psi_{sampling}(\vec{r})$ depending on spatial coordinates only:

$$p(\vec{r}) = \Psi^2_{sampling}(\vec{r}). \tag{D.3}$$

The sampling wavefunction should span the integration space of Ψ as closely as possible, and yet the norm $\langle \Psi_{sampling} | \Psi_{sampling} \rangle$ must be known analytically to be equal to one.

For compact nuclei such as ^{4}He, the norm $\langle\Psi|\Psi\rangle$ can be estimated accurately by using a simple Gaussian as the sampling wavefunction:

$$\Psi^{Gauss}_{sampling} = C \exp\left[-\frac{1}{2}\alpha \sum_{i<j=1}^{A} \left(\vec{r}_i - \vec{r}_j\right)^2\right], \tag{D.4}$$

where C is a normalization coefficient and α is adjusted to reproduce the rms matter radius of the nucleus.

For ^{6}He, however, the sampling wavefunction from Eq. (D.4) is not flexible enough to mimic the extended neutron density and a more sophisticated sampling function is needed. For ^{6}He, we have tested several sampling wavefunctions. The most accurate results for Eq. (D.1) have been obtained with the symmetrized product of a Gaussian for the ^{4}He core (particles $p_1, \ldots, p_4$) and a hyper-radial Gaussian for the valence part (particles p_5 and p_6):

$$\Psi^{Gauss+Gauss,sym}_{sampling} = \mathcal{S}^{core-val} \Psi^{Gauss+Gauss}_{sampling}, \tag{D.5}$$

where:

$$\Psi^{Gauss+Gauss}_{sampling} = C \exp\left[-\frac{1}{2}\alpha \sum_{i<j=1}^{4} \left(\vec{r}_{p_i} - \vec{r}_{p_j}\right)^2\right] \exp\left[-\frac{1}{2}\frac{\rho^2}{\rho_0^2}\right], \tag{D.6}$$

and $\mathcal{S}^{core-val} = \sum_1^{A(A-1)/2} P$ is the core-valence symmetrizer running over all particle permutations between the core and the valence part. The hyper-radius ρ is computed assuming two valence particles attached to the core as in Figure 2.1. Parameters α and ρ_0 are adjusted to produce the most reliable estimate in Eq. (D.1). The normalization coefficient C in Eq. (D.6) can be computed analytically.

Using the sampling function $\Psi^{Gauss+Gauss,sym}_{sampling}$, the wavefunction of ^{6}He can easily be normalized to unity with an accuracy of 0.3% or better. This accuracy is sufficient for the computation of the overlap integral between ^{4}He and ^{6}He in Section 5.3.

Bibliography

[1] R. E. Grisenti et al., Phys. Rev. Lett. **85**, 2284 (2000).

[2] Y. Li, Q. Gou, and T. Shi, Phys. Rev. A **74**, 032502 (2006).

[3] J. Mitroy, Phys. Rev. Lett. **94**, 033402 (2005).

[4] A. Cobis, A. S. Jensen, and D. V. Fedorov, J. Phys. G: Nucl. Part. Phys. **23**, 401 (1997).

[5] A. S. Jensen et al., Rev. Mod. Phys. **76**, 215 (2004).

[6] K. Riisager, D. V. Fedorov, and A. S. Jensen, Europhys. Lett. **49**, 547 (2000).

[7] A. S. Jensen and M. V. Zhukov, Nucl. Phys. A **693**, 411 (2001).

[8] D. V. Fedorov, A. S. Jensen, and K. Riisager, Phys. Lett. B **312**, 1 (1993).

[9] A. S. Jensen and K. Riisager, Phys. Lett. B **480**, 39 (2000).

[10] F. M. Nunes, I. J. Thompson, and R. C. Johnson, Nucl. Phys. A **596**, 171 (1996).

[11] D. Bazin et al., Phys. Rev. C **57**, 2156 (1998).

[12] Z. H. Liu et al., Phys. Rev. C **64**, 034312 (2001).

[13] M. V. Zhukov et al., Phys. Rep. **231**, 151 (1993).

[14] C. Bachelet et al., Phys. Rev. Lett. **100**, 182501 (2008).

[15] I. J. Thompson and M. V. Zhukov, Phys. Rev. C **53**, 708 (1996).

[16] W. Horiuchi and Y. Suzuki, Phys. Rev. C **74**, 034311 (2006).

[17] P. G. Hansen, A. S. Jensen, and B. Jonson, Annu. Rev. Nucl. Part. Sci. **45**, 591 (1995).

[18] I. Tanihata et al., Phys. Lett. B **289**, 261 (1992).

[19] R. E. Warner et al., Phys. Rev. C **52**, R1166 (1995).

[20] R. Kanungo et al., Phys. Lett. B **571**, 21 (2003).

[21] V. Rotival and T. Duguet, arXiv:nucl-th/0702050v3 (2007).

[22] V. Rotival, K. Bennaceur, and T. Duguet, arXiv:0711.1275v1 [nucl-th] (2007).

[23] V. M. Efimov, Phys. Lett. B **33**, 563 (1970).

[24] V. M. Efimov, Comments Nucl. Part. Phys. **19**, 271 (1990).

[25] D. R. Tilley et al., Nucl. Phys. A **708**, 3 (2002).

[26] T. Björnstad et al., Nucl. Phys. A **359**, 1 (1981).

[27] T. Bjerge, Nature **138**, 400 (1936).

[28] A. M. Poskanzer et al., Phys. Rev. Lett. **17**, 1271 (1966).

[29] I. Tanihata et al., Phys. Rev. Lett. **55**, 2676 (1985).

[30] I. Tanihata et al., Phys. Lett. B **160**, 380 (1985).

[31] P. G. Hansen and B. Jonson, Europhys. Lett. **4**, 409 (1987).

[32] T. Kobayashi et al., Phys. Rev. Lett. **60**, 2599 (1988).

[33] T. Kobayashi et al., Phys. Lett. B **232**, 51 (1989).

[34] R. Anne et al., Phys. Lett. B **250**, 19 (1990).

[35] B. Blank et al., Z. Phys. A **340**, 41 (1991).

[36] I. Tanihata et al., Phys. Lett. B **287**, 307 (1992).

[37] C.-B. Moon et al., Phys. Lett. B **297**, 39 (1992).

[38] Y. Ohbayasi and Y. Suzuki, Phys. Lett. B **346**, 223 (1995).

[39] M. V. Zhukov et al., Phys. Rev. C **52**, 2461 (1995).

[40] I. Mukha et al., Phys. Lett. B **367**, 65 (1996).

[41] M. J. G. Borge et al., Nucl. Phys. A **613**, 199 (1997).

[42] R. Raabe et al., Phys. Rev. Lett. **101**, 212501 (2008).

[43] I. Tanihata, J. Phys. G: Nucl. Part. Phys. **22**, 157 (1996).

[44] I. J. Thompson, Nucl. Phys. A **701**, 7 (2002).

[45] N. Keeley et al., Prog. Part. Nucl. Phys. **59**, 579 (2007).

[46] M. Smith et al., arXiv:0807.1260v2 [nucl-ex] (2008).

[47] L.-B. Wang et al., Phys. Rev. Lett. **93**, 142501 (2004).

[48] R. Sánchez et al., Phys. Rev. Lett. **96**, 033002 (2006).

[49] R. Neugart et al., Phys. Rev. Lett. **101**, 132502 (2008).

[50] I. Brida, F. M. Nunes, and B. A. Brown, Nucl. Phys. A **775**, 23 (2006).

[51] E. Sauvan et al., Phys. Rev. Lett. **87**, 042501 (2001).

[52] I. Tanihata et al., Phys. Rev. Lett. **100**, 192502 (2008).

[53] A. Chatterjee et al., Phys. Rev. Lett. **101**, 032701 (2008).

[54] J. S. Al-Khalili and J. A. Tostevin, Phys. Rev. Lett. **76**, 3903 (1996).

[55] I. J. Thompson and Y. Suzuki, Nucl. Phys. A **693**, 424 (2001).

[56] J. S. Al-Khalili and F. M. Nunes, J. Phys. G: Nucl. Part. Phys. **29**, R89 (2003).

[57] J. M. Bang and I. J. Thompson, Phys. Lett. B **279**, 201 (1992).

[58] E. Garrido, D. V. Fedorov, and A. S. Jensen, Nucl. Phys. A **700**, 117 (2002).

[59] M. V. Zhukov et al., Phys. Lett. B **265**, 19 (1991).

[60] L. Johannsen, A. S. Jensen, and P. G. Hansen, Phys. Lett. B **244**, 357 (1990).

[61] G. F. Bertsch and H. Esbensen, Ann. Phys. **209**, 327 (1991).

[62] Y. Tosaka and Y. Suzuki, Nucl. Phys. A **512**, 46 (1990).

[63] K. Ikeda, Nucl. Phys. A **538**, 355c (1992).

[64] N. Vinh Mau and J. C. Pacheco, Nucl. Phys. A **607**, 163 (1996).

[65] F. M. Nunes, *Core excitation in few-body systems: Application to light exotic nuclei*, PhD thesis, University of Surrey, England, 1995.

[66] S. C. Pieper and R. B. Wiringa, Annu. Rev. Nucl. Part. Sci. **51**, 53 (2001).

[67] S. C. Pieper, Nucl. Phys. A **751**, 516 (2005).

[68] B. R. Barrett et al., Nucl. Phys. A **746**, 579 (2004).

[69] P. Navrátil et al., Phys. Rev. Lett. **87**, 172502 (2001).

[70] P. Navrátil and B. R. Barrett, Phys. Rev. C **57**, 3119 (1998).

[71] H. Feldmeier and J. Schnack, Rev. Mod. Phys. **72**, 655 (2000).

[72] T. Neff, H. Feldmeier, and R. Roth, Nucl. Phys. A **752**, 321 (2005).

[73] N. Itagaki, A. Kobayakawa, and S. Aoyama, Phys. Rev. C **68**, 054302 (2003).

[74] K. Varga and Y. Suzuki, Phys. Rev. C **52**, 2885 (1995).

[75] K. Arai et al., Prog. Theor. Phys. Suppl. **142**, 97 (2001).

[76] K. Arai, Y. Suzuki, and R. G. Lovas, Phys. Rev. C **59**, 1432 (1999).

[77] K. Varga, Y. Suzuki, and R. G. Lovas, Phys. Rev. C **66**, 041302 (2002).

[78] J. Wurzer and H. M. Hofmann, Phys. Rev. C **55**, 688 (1997).

[79] S. Korennov and P. Descouvemont, Nucl. Phys. A **740**, 249 (2004).

[80] J. R. Armstrong, *A cluster model of ^{6}He and ^{6}Li*, PhD thesis, Michigan State University, USA, 2007.

[81] G. F. Bertsch, B. A. Brown, and H. Sagawa, Phys. Rev. C **39**, 1154 (1989).

[82] B. A. Brown, Prog. Part. Nucl. Phys. **47**, 517 (2001).

[83] N. Michel et al., Phys. Rev. Lett. **89**, 042502 (2002).

[84] T. T. S. Kuo, F. Krmpotić, and Y. Tzeng, Phys. Rev. Lett. **78**, 2708 (1997).

[85] J. M. Bang, Phys. Rep. **264**, 27 (1996).

[86] K. Riisager, Rev. Mod. Phys. **66**, 1105 (1994).

[87] F. M. Nunes, C. R. Physique **4**, 489 (2003).

[88] I. J. Thompson et al., Phys. Rev. C **61**, 024318 (2000).

[89] N. K. Timofeyuk, Phys. Rev. C **63**, 054609 (2001).

[90] K. M. Nollett, Phys. Rev. C **63**, 054002 (2001).

[91] P. Navrátil, Phys. Rev. C **70**, 054324 (2004).

[92] F. M. Nunes et al., Nucl. Phys. A **609**, 43 (1996).

[93] I. J. Thompson, F. M. Nunes, and B. V. Danilin, Comp. Phys. Comm. **161**, 87 (2004).

[94] B. V. Danilin et al., Nucl. Phys. A **632**, 383 (1998).

[95] L. M. Delves, Nucl. Phys. **20**, 275 (1960).

[96] G. Erens, J. L. Visschers, and R. van Wageningen, Ann. Phys. **67**, 461 (1971).

[97] M. Abramowitz and I. A. Stegun, *Handbook of mathematical functions*, Dover Publications, 1972.

[98] M. Theeten, D. Baye, and P. Descouvemont, Phys. Rev. C **74**, 044304 (2006).

[99] D. R. Tilley et al., Nucl. Phys. A **745**, 155 (2004).

[100] J. Raynal and J. Revai, Il Nuovo Cimento **68**, 612 (1970).

[101] B. M. Young et al., Phys. Rev. Lett. **71**, 4124 (1993).

[102] C. Bachelet et al., Eur. Phys. J. A **25**, s1.31 (2005).

[103] D. V. Fedorov, E. Garrido, and A. S. Jensen, Phys. Rev. C **51**, 3052 (1995).

[104] H. Esbensen, G. F. Bertsch, and K. Hencken, Phys. Rev. C **56**, 3054 (1997).

[105] S. N. Ershov et al., Phys. Rev. C **70**, 054608 (2004).

[106] W. Koepf et al., Z. Phys. A **340**, 119 (1991).

[107] J. Meng and P. Ring, Phys. Rev. Lett. **77**, 3963 (1996).

[108] S. Karataglidis et al., Phys. Rev. Lett. **79**, 1447 (1997).

[109] D. Gogny, P. Pires, and R. D. Tourreil, Phys. Lett. B **32**, 591 (1970).

[110] B. A. Brown, private communication, 2004.

[111] D. Borremans et al., Phys. Rev. C **72**, 044309 (2005).

[112] F. Ajzenberg-Selove, Nucl. Phys. A **506**, 1 (1990).

[113] http://www.fresco.org.uk/programs/efaddy/.

[114] H. B. Jeppesen et al., Nucl. Phys. A **748**, 374 (2005).

[115] I. J. Thompson, private communication, 2008.

[116] S. Funada, H. Kameyama, and Y. Sakuragi, Nucl. Phys. A **575**, 93 (1994).

[117] S. C. Pieper et al., Phys. Rev. C **64**, 014001 (2001).

[118] D. R. Tilley, H. R. Weller, and G. M. Hale, Nucl. Phys. A **541**, 1 (1992).

[119] H. Kamada et al., Phys. Rev. C **64**, 044001 (2001).

[120] B. S. Pudliner et al., Phys. Rev. C **56**, 1720 (1997).

[121] V. I. Kukulin and V. M. Krasnopol'sky, J. Phys. G: Nucl. Part. Phys. **3**, 795 (1977).

[122] Y. Suzuki and K. Varga, *Stochastic variational approach to quantum-mechanical few-body problems*, Springer-Verlag Berlin-Heidelberg, 1998.

[123] K. Varga, Nucl. Phys. A **684**, 209 (2001).

[124] K. Varga, private communication, 2006.

[125] K. Varga, Y. Ohbayasi, and Y. Suzuki, Phys. Lett. B **396**, 1 (1997).

[126] S. F. Boys, Proc. R. Soc. London Ser. A **258**, 402 (1960).

[127] K. Singer, Proc. R. Soc. London Ser. A **258**, 412 (1960).

[128] S. A. Alexander, H. J. Monkhorst, and K. Szalewicz, J. Chem. Phys. **85**, 5821 (1986).

[129] D. B. Kinghorn and R. D. Poshusta, Phys. Rev. A **47**, 3671 (1993).

[130] Y. Suzuki et al., Nucl. Phys. A **706**, 123 (2002).

[131] H. Kameyama, M. Kamimura, and Y. Fukushima, Phys. Rev. C **40**, 974 (1989).

[132] K. Varga, Y. Suzuki, and R. G. Lovas, Nucl. Phys. A **571**, 447 (1994).

[133] K. Varga, Y. Suzuki, and Y. Ohbayasi, Phys. Rev. C **50**, 189 (1994).

[134] A. Csótó, Phys. Rev. C **48**, 165 (1993).

[135] A. B. Volkov, Nucl. Phys. **41**, 33 (1965).

[136] D. R. Thompson, M. Lemere, and Y. C. Tang, Nucl. Phys. A **286**, 53 (1997).

[137] I. Reichstein and Y. C. Tang, Nucl. Phys. A **158**, 529 (1970).

[138] W. M. C. Foulkes et al., Rev. Mod. Phys. **73**, 33 (2001).

[139] M. H. Kalos and P. A. Whitlock, *Monte Carlo methods, Volume I: Basics*, John Wiley & Sons, 1986.

[140] J. A. Carlson and R. B. Wiringa, Variational Monte Carlo techniques in nuclear physics, in *Computational nuclear physics I: Nuclear structure*, edited by K. Langanke, J. A. Maruhn, and S. E. Koonin, Springer-Verlag, 1991.

[141] N. Metropolis et al., J. Chem. Phys. **21**, 1087 (1953).

[142] H. Flyvbjerg and H. G. Petersen, J. Chem. Phys. **91**, 461 (1989).

[143] C. J. Umrigar, K. G. Wilson, and J. W. Wilkins, Phys. Rev. Lett. **60**, 1719 (1988).

[144] P. R. C. Kent, R. J. Needs, and G. Rajagopal, Phys. Rev. B **59**, 12344 (1999).

[145] M. Snajdr and S. M. Rothstein, J. Chem. Phys. **112**, 4935 (2000).

[146] M. P. Nightingale and V. Melik-Alaverdian, Phys. Rev. Lett. **87**, 043401 (2001).

[147] W. H. Press et al., *Numerical Recipes in FORTRAN 77: The Art of Scientific Computing*, Cambridge University Press, 1992.

[148] E. Anderson et al., *LAPACK Users' Guide*, Society for Industrial and Applied Mathematics, 1999.

[149] X. Lin, H. Zhang, and A. M. Rappe, J. Chem. Phys. **112**, 2650 (2000).

[150] C. J. Umrigar et al., Phys. Rev. Lett. **98**, 110201 (2007).

[151] I. Sick, Phys. Rev. C **77**, 041302 (2008).

[152] I. Tanihata et al., Phys. Lett. B **206**, 592 (1988).

[153] I. Brida and F. M. Nunes, Int. Jour. Mod. Phys. E **17**, 2374 (2008).

[154] I. Sick, Phys. Lett. B **576**, 62 (2003).

[155] S. Kopecky et al., Phys. Rev. Lett. **74**, 2427 (1995).

[156] S. Kopecky et al., Phys. Rev. C **56**, 2229 (1997).

[157] J. M. Bang et al., Phys. Rep. **125**, 253 (1985).

[158] G. M. Ter-Akopian et al., Phys. Lett. B **426**, 251 (1998).

[159] A. N. Ostrowski et al., J. Phys. G: Nucl. Part. Phys. **24**, 1553 (1998).

[160] Y. T. Oganessian, V. I. Zagrebaev, and J. S. Vaagen, Phys. Rev. C **60**, 044605 (1999).

[161] R. Raabe et al., Phys. Lett. B **458**, 1 (1999).

[162] G. R. Satchler, *Direct nuclear reactions*, Oxford: Clarendon Press, 1983.

[163] I. J. Thompson, Comput. Phys. Rep. **7**, 167 (1988).